

Study, design and realization of a communication system for untethered underwater vehicles

Auteur : François, Simon

Promoteur(s) : Redouté, Jean-Michel

Faculté : Faculté des Sciences appliquées

Diplôme : Master : ingénieur civil électricien, à finalité spécialisée en "electronic systems and devices"

Année académique : 2023-2024

URI/URL : <http://hdl.handle.net/2268.2/20999>

Avertissement à l'attention des usagers :

Tous les documents placés en accès ouvert sur le site le site MatheO sont protégés par le droit d'auteur. Conformément aux principes énoncés par la "Budapest Open Access Initiative"(BOAI, 2002), l'utilisateur du site peut lire, télécharger, copier, transmettre, imprimer, chercher ou faire un lien vers le texte intégral de ces documents, les disséquer pour les indexer, s'en servir de données pour un logiciel, ou s'en servir à toute autre fin légale (ou prévue par la réglementation relative au droit d'auteur). Toute utilisation du document à des fins commerciales est strictement interdite.

Par ailleurs, l'utilisateur s'engage à respecter les droits moraux de l'auteur, principalement le droit à l'intégrité de l'oeuvre et le droit de paternité et ce dans toute utilisation que l'utilisateur entreprend. Ainsi, à titre d'exemple, lorsqu'il reproduira un document par extrait ou dans son intégralité, l'utilisateur citera de manière complète les sources telles que mentionnées ci-dessus. Toute utilisation non explicitement autorisée ci-avant (telle que par exemple, la modification du document ou son résumé) nécessite l'autorisation préalable et expresse des auteurs ou de leurs ayants droit.

University of Liège
Faculty of Applied Sciences



Study, design and realization of a communication system for untethered underwater vehicles

Author:

SIMON FRANÇOIS

Supervisor:

PROF. J.M. REDOUTÉ

Reading committee:

PROF. T. GILET

PROF. P. VANDERBEMDEN

Academic Year 2023-2024

Master's thesis submitted in partial fulfillment of the requirements for the
Master degree in

Electrical Engineering

Professional focus : Electronic systems and devices

ABSTRACT

This master thesis aims to design and realize a high-speed communication system for untethered underwater devices fulfilling three criteria : 1) Providing a short range, up to 50 m, untethered transmission system from the ROV or AUV to the receiver; 2) Having a data rate in the Mbps range suitable for the transmission of multimedia contents; 3) Having a limited cost in order to be more accessible than existing devices with a total BOM price under 1,000.00 EUR. After an evaluation of the technical approaches of the transmission system and the underwater environment, an optical communication system was specified. Then the design and various components of the final system were evaluated, selected, crafted and tested. The objectives were met, though additional testing to validate the maximum range of the system is required.

ACKNOWLEDGEMENTS

I would like first to express my heartfelt gratitude to Professor Jean Michel Redouté. Beyond my thesis, meeting the Professor Redouté has been one of the highlights of my academic studies. His talent is matched only by his admirable human qualities, which have left a lasting impression on me. Also the professor Philippe Vanderbemden that gave me support and guidance allong all my studies specially regarding my particular situation. I would also warmly thanks François Piron for all his precious advices along the realisation of this master thesis and the professor Tristan Gillet and its team for their help and the possibility to conduct my experiments in their laboratory.

Finally, as I bring this thesis to a close, I wish to honor the memory of Hervé Pierre who sadly left us this year. Hervé was the first person to whom I showed the draft of this thesis. From wherever you are now, thank you, Hervé, for your kindness and for everything you did for the students...

Introduction	1
1 Underwater optical communication system	8
1.1 Optical transmission in underwater environment	9
1.2 Review of Underwater Optical Communication System (UWOCS)	17
1.2.1 General overview	17
1.2.2 Source and channel encoder	18
1.2.3 Modulation	18
1.2.4 Optical source and driver	21
1.2.5 Optical sensor and optics	22
1.2.6 Signal Processing	24
1.2.7 Demodulation Source and channel decoder	25
1.3 Proposed UWOCS design and specifications	26
2 Prototype design and realization	31
2.1 Receiver module	31
2.1.1 Silicon Photomultiplier sensors (SiPM)	31
2.1.2 Amplification stage	42
2.1.3 Emitter board simulation	50
2.1.4 Printed Circuit Board (PCB) design	59
2.1.5 PCB Board realization	69
2.1.6 Receiver power supply design and realization	72
2.1.7 Alternative UWOCS receiver design	74
2.2 Emitter Design	76
2.2.1 LED review	76
2.2.2 Led and driver selection	81
2.2.3 Emitter PCB design and realization	84
2.2.4 Receiver power supply design and realization	88

3	System evaluation and discussion	90
3.1	Test bench design and realization	90
3.1.1	Test bench design	90
3.1.2	Test bench realization	91
3.1.3	UWOCS evaluation	93
3.2	Discussion	99
4	Conclusion and perspectives	101
A	Different useful Tables	113
A.1	Underwater environment.	113
A.2	Bill of materials	114
B	Useful figures	116
B.1	Simulation	116
B.2	Schematics	116

LIST OF FIGURES

1	Picture of two underwater vehicles. Taken from [7] p.3	1
2	Picture of a ROV tether and its feeder. Taken from [9]	2
3	Picture of a Tonpilz acoustic transducer with its piezo stack. Taken from [12] p.10	3
4	Paul Langevin's patent drawing of an acoustic quartz transducer. Taken from [12] p.5	3
5	Absorbtion of sound by seawater function of the sound frequency. Taken from [15], cited in [16]	4
6	Absorption of visible light by seawater as a function of the EM wavelength. Taken from [18]	4
7	Picture of the Popoto acoustic emitter. Taken from [22]	5
8	Picture of the Teledyne acoustic emitter UTS-9500. Taken from [20]	5
9	Conceptual view of the high speed system in its underwater environment. Background picture adapted from [23]	6
1.1	Light absorption and scattering trough a small piece of water. Image adapted from [18, Chapter 7]	9
1.2	Absorption coefficient $a(\lambda)$ as a function of visible EM spectrum for pure sea water. Taken from [18] p.152	11
1.3	Scattering coefficient $b(\lambda)$ as a function of the visible EM spectrum for pure sea water. Taken from [18] p.152	11
1.4	Typical absorption coefficient of CDOM as a function of the visible EM spectrum. Taken from [18] p.153	12
1.5	Typical absorption coefficient of detritus as a function of the visible EM spectrum. Taken from [18] p.153	13
1.6	Typical absorption coefficient of phytoplankton as a function of the visible EM spectrum. Taken from [18] p.153	14
1.7	Typical scattering coefficient of Detritus function of the EM visible Spectrum. Taken from [18] p.156	15
1.9	Emitted signal	15
1.10	Distance = 50 m	15

1.11	Signal distortion due to ISI. Taken from [32] p.1626. No ordinate units are provided	15
1.8	Typical scattering coefficient of Phytoplankton function of the EM visible Spectrum. Taken from [18] p.156	16
1.12	Block diagram of usuals components or sections composing UWOCs system. Optional blocks are circled with dotted line. Adapted from [14] and [18]	17
1.13	Block diagram of usual modulation techniques in UWOCs system. Taken from [38] p.158	18
1.14	Modulation scheme of OOK with T_b the bitstream period and T_s the symbol period. Adapted from [40] p.2 and [18]	19
1.15	Modulation scheme of 4-PPM with T_p the pulse period, T_b the bitstream period and T_s the symbol period. Adapted from [40] p.2 and [18]	20
1.16	Modulation scheme of 4-PWM with T_p the pulse period, T_b the bitstream period and T_s the symbol period. Adapted from [40] p.2 and [18]	21
1.17	Modulation scheme of 4-DPIM with T_p the pulse period, T_b the bitstream period and T_s the symbol period. Adapted from [40] p.2 and [18]	21
1.18	Picture of a PIN photodiode S1223 from Hamamatsu taken from [44]	23
1.19	Picture of an APD S5344 from Hamamatsu taken from [46]	24
1.20	Picture of an APD control circuit from Hamamatsu with the the high voltage unit on the left of the picture. Taken from [47]	24
1.21	Schematic of a ultra high speed Op-amp OPA818 used as TIA with its feedback resistor and capacitance. Taken from [51] p.1	25
1.22	General block diagram of the designed UWOCs	26
1.23	8-DPIM scheme selected for the designed UWOCs with T_p the fixed pulse rate and T_i the symbol duration.	28
1.24	Emitter design specification.	29
2.1	Picture of SiPM microcells from ON Semiconductor. Taken from [48] p.1 . .	32
2.2	Schematics of a SiPM with the SPAD diodes and their quenching resistances in series. Taken from [48] p.1	32
2.3	Spad photodiode operating cycle in Geiger mode. Taken from [56] p.1	33
2.4	Different voltage pulses superimposed related to the current flowing trough a SiPM sensor when illuminated by different level of pulsed light. Taken from [56] p.3	33
2.5	Pulse shape voltage of a SiPM sensor in series with a 16 ohm resistor. Taken from [48], p. 3.	34
2.6	The SiPM output current function of the received light power. Taken from [56] p.9	35
2.7	The SiPM sensor in serie with a resistance R_s . Adapted from [52] p.8	37
2.8	Picture of the SiPM MicroFJ 60035 taken from [61] p.10	37
2.9	Picture of the evaluation board for the SiPM MicroFJ 60035 taken from [61] p.6	37
2.10	Incoming light power $P_{SiPM}[\frac{W}{m^2}]$ on the active surface of the SiPM sensor as a function of distance, d , for different beam angles.	38
2.11	Output current $I_{SiPM}(d)[W]$ from the SiPM sensor as a function of the distance, d , for different beam angles with a luminous power $P_l = 1 W$	40

2.12	Output current I_{SiPM} [W] from the SiPM sensor as a function of the incoming power, P_{in} .	41
2.13	The SiPM sensor in serie with a resistor R_s . Adapted from [52] p.8	43
2.14	The OPA818 from Texas Instruments and its WSON package. Taken from [68]	44
2.15	The OPA818 used in inverting configuration with R_G and R_F . Taken from [51] p.15	45
2.16	Output current $I_{SiPM}(d)$ [A] from the SiPM sensor as a function of the distance, d , for different beam angles with a luminous power $P_l = 3$ W.	46
2.17	Schematic of the implemented amplification stage using OPA818 from Texas Instruments.	47
2.18	Schematic of the implemented high pass filter using resistor and capacitor.	47
2.19	Schematic of the implemented comparator stage using TLV3601 comparator.	50
2.20	Schematic of the modeled SiPM MicroFJ-60035 used for Pspice simulation.	51
2.21	Schematic of the first amplification stage with its associated High Pass filter stage.	52
2.22	Schematic of the second amplification stage with its associated High Pass filter stage.	52
2.23	Schematic of the last amplification stage with a $50\ \Omega$ output resistance.	53
2.24	Schematic of the comparator with the different voltage divider and the simulated .	53
2.25	Transient simulation of the receiver board showing both output voltage of the last amplification stage and comparator and the SiPM output current. This simulation uses the shortest pulse interval and the SiPM minimum output current.	54
2.26	Transient simulation of the receiver board showing the output voltage of the first amplification stage and the SiPM output current. This simulation uses the shortest pulse interval and the SiPM minimum output current.	55
2.27	Transient simulation of the receiver board showing the output voltage of the first high pass filter and the SiPM output current. This simulation uses the shortest pulse interval and the SiPM minimum output current.	55
2.28	Transient simulation of the receiver board showing both output voltage of the last amplification stage and comparator and the SiPM output current. This simulation uses the shortest pulse interval and the SiPM maximum output current	56
2.29	Transient simulation of the receiver board showing the output voltage of the SiPM sensor and the SiPM output current. This simulation uses the shortest pulse interval and the SiPM maximum output current	57
2.30	Transient simulation of the receiver board showing the current trough the feedback and output pin of the first Op-amp and the output power of the first Op-Amp and comparator. This when the SiPM maximum output current occurs.	57
2.31	Transient simulation of the receiver board illustrating both output voltage of the last amplification stage and comparator and the SiPM output current. This simulation uses the longest pulse interval and the SiPM minimum output current.	58

2.32	AC simulation of the receiver board showing the gain between the last amplification stage output and the SiPM output voltage, using the lowest SiPM output current.	59
2.33	Picture of the selected SMA connector from Samtec. Taken from [86]	60
2.34	Schematic of the 5019 test pad from Keystone. Taken from [87]	60
2.35	Schematic of the output and selection ports of the UWOCs receiver board .	61
2.36	Schematic of the output and selection ports of the UWOCs receiver board .	61
2.37	Picture of the BGA pads of the MicroFJ-60035. Dimension in [mm].Taken from [61]	62
2.38	Schematic of the BGA pads of the MicroFJ-60035. Taken from [61]	62
2.39	Picture of a 100 nF capacitor using 0603 package	62
2.40	Schematic of the SiPM sensors connections and its decoupling capacitors . .	62
2.41	Schematic of the first amplification stage using OPA818	63
2.42	Schematic of the decoupling stage of the first Op-Amp and the first high-pass filter	63
2.43	Schematic of the TLV3601 comparator with the different voltage divider and its decoupling capacitors	64
2.44	Schematic of the comparator stage power supply	64
2.45	Stackup of the designed PCB. Taken from [92]	65
2.46	Picture of a 50nm hard coated optical filter from Edmund optics. Taken from [95]	66
2.47	Schematic of a 50nm hard coated optical filter from Edmund optics. Taken from [95]	66
2.48	Picture of the SiPM footprint on the designed PCB.	66
2.49	Picture of the gain resistor and capacitor of one of the OPA818 on the designed PCB.	66
2.50	Picture of the final PCB layout without the mass and power planes	67
2.51	3D image of the final UWOCs receiver PCB.	68
2.52	3D image of the bottom of the final UWOCs receiver PCB.	68
2.53	Picture of the cut-out plane trough the different PCB layer at the inverting input and output of the OPA818	68
2.54	Unsoldered manufactured PCB of the UWOCs receiver.	69
2.55	UWOCs receiver PCB fixed under its stencil before applying the solder paste	70
2.56	Some footprint of the receiver PCB viewed on microscope after applying the solder paste	70
2.57	Picture of the solder paste 4902P tube from MG Chemicals. Taken from [98]	70
2.58	Temperature reflow profile of the 4902P solder paste from MG Chemichals. Taken from [98]	70
2.59	The SiPM sensor when placed on the receiver PCB	71
2.60	Placed components and awaiting footprint with the solder paste	71
2.61	Picture of the implemented alternative reflow system.	71
2.62	Thermal image when the PCB is reflowed	71
2.63	Picture of the completed UWOCs receiver PCB	72
2.64	Schematic of the $\pm 5V$ DC/DC Meanwell converter	72
2.65	Schematic of the boost converter with its auxiliaries components	73

2.66	Picture of the final receiver supply PCB layout.	73
2.67	Picture of the final realized PCB with its components.	73
2.68	Picture of the LT1222 from Analog Devices. Taken from [104]	74
2.69	Picture of the evaluation board for the SiPM MicroFJ 60035 taken from [61] p.6	74
2.70	Picture of the alternative UWOCS receiver PCB layout	75
2.71	Graph of the I-V curve of a diode. Adapted from [107].	76
2.72	The emission spectrum of three Led XLamp XHP35.2 from Cree. Graph taken from [110].	78
2.73	Schematic of a Planar LED structure taken from [38] p.46	78
2.74	Lambertian light intensity distribution of a Planar LED structure taken from [38]	78
2.75	Schematic of a Dome led structure taken from [38] p.47	79
2.76	Eye sensitivity function and Luminous efficacy functions of the Wavelength λ . Taken from [38] p.50	80
2.77	Electromagnetic spectral power distribution of different Leds from Lumileds. Taken from [112] p.7	80
2.78	Picture of the LED GD CSSRM3.14 from OSRAM. Taken from [113] p.1	82
2.79	Spectral bandwidth of the LED GD CSSRM3.14 from OSRAM. Taken from [113] p.8	82
2.80	Schematic of a usual high speed LED driver circuit. Adapted from [114] p.2	82
2.81	Proposed high speed LED driver circuit. Taken from [113] p.8	82
2.82	Picture of the wide beam optical reflector used in the emitter board. Taken from [117]	84
2.83	Picture of the narrow beam optical reflector used in the emitter board. Taken from [118]	84
2.84	Schematic of the first LED circuit of the UWOCS emitter board	85
2.85	Schematic of the input ports of the UWOCS emitter board	85
2.86	Design of the UWOCS emitter board	86
2.87	Picture of the manufactured UWOCS Emitter board	86
2.88	UWOCS Emitter board with solder paste applied on it	86
2.89	Final assembled UWOCS emitter board with their optical concentrators	87
2.90	Schematic of the RSDW60F-05 DC/DC Meanwell converter	88
2.91	Picture of the final emitter supply PCB layout	89
2.92	Picture of the emitter supply board with its components placed on it	89
2.93	Picture of the emitter supply board with its components placed on it (bottom)	89
3.1	Schematic of the implemented test bench in order to evaluate the UWOCS.	91
3.2	Pipe support of the test bench under construction	91
3.3	Test bench pipe's support glued	91
3.4	Emitter and receiver isolated box under construction	92
3.5	Test bench's internal glass	92
3.6	Test bench deployed with the pipe extension along it.	92
3.7	Receiver fixed on the test bench	92
3.8	Test bench pipe	92
3.9	Emitter superimposed by the two polarisers uncrossed	93

3.10	Emitter superimposed by the two polarisers crossed	93
3.11	Comparator signal with the emitter and receiver at a distance of 4.5m and with symbol 1 transmitted	94
3.12	Eye diagram of the comparator signal with the emitter and receiver at a distance of 4.5m and with symbol 1 transmitted	94
3.13	Comparator signal with the emitter and receiver at a distance of 4.5m and with symbol 8 transmitted	95
3.14	Eye diagram of the comparator signal with the emitter and receiver at a distance of 4.5m and with symbol 8 transmitted	95
3.15	FFT of the comparator signal with the emitter and receiver at a distance of 4.5m and with symbol 1 transmitted	95
3.16	FFT of the comparator signal with the emitter and receiver at a distance of 4.5m and with symbol 3 transmitted	96
3.17	FFT of the comparator signal with the emitter and receiver at a distance of 4.5m and with symbol 8 transmitted	96
3.18	Comparator signal with the emitter and receiver at a distance of 14.5m and with symbol 1 transmitted	97
3.19	Eye diagram of the comparator signal with the emitter and receiver at a distance of 14.5m and with symbol 1 transmitted	97
3.20	FFT of the comparator signal with the emitter and receiver at a distance of 14.5m and with symbol 1 transmitted	97
3.21	Amplification stage signal with the emitter and receiver at a distance of 50m and with symbol 1 transmitted	98
3.22	Eye diagram of the amplification stage signal with the emitter and receiver at a distance of 50m and with symbol 1 transmitted	98
3.23	FFT of the amplification stage signal with the emitter and receiver at a distance of 14.5m and with symbol 1 transmitted	98
A.1	Bill of material (BOM) of the UWOCS receiver board	114
A.2	Bill of material (BOM) of the UWOCS receiver supply board	115
A.3	Bill of material (BOM) of the UWOCS emitter board	115
A.4	Bill of material (BOM) of the UWOCS emitter supply board	115
B.1	AC simulation of the receiver board showing the gain between the last amplification stage output and the SiPM output voltage. This taking the highest SiPM output current	116
B.2	Schematics of the receiver board. Page 1 of 5.	117
B.3	Schematics of the receiver board. Page 2 of 5.	118
B.4	Schematics of the receiver board. Page 3 of 5.	119
B.5	Schematics of the receiver board. Page 4 of 5.	120
B.6	Schematics of the receiver board. Page 5 of 5.	121

LIST OF TABLES

1.1	Suited Operating Wavelength range (nm) for different water types. Adapted from [13]	13
1.2	Absorption and scattering coefficients for different water types at a wavelength of $\lambda \approx 450$ nm. Adapted from [30] cited in [31].	14
1.3	Comparison of Laser and LED technologies for UWOCs.	22
1.4	Symbol, Bits, Pulse Duration, and Total Time Interval for various codes. . .	27
1.5	Synthesis of the UWOCs Design Specifications	30
2.1	Maximum and minimum current output of the SiPM sensor function of the emitter-receiver distance and beam angle.	39
2.2	Input-output relationship for the comparator circuit. Adapted from [74] . . .	49
2.3	Common LED materials and their optical radiation wavelengths. Table taken and adapted from:[38], p.45	77
2.4	LED Requirements for the proposed system.	81
3.1	Total cost of the implemented UWOCs system.	100
A.1	Absorption coefficient $a(\lambda)$ for various wavelength in the visible EM spectrum. Adapted from [17] p.98	113
A.2	Irradiance [$\frac{W}{m^2}$] at the receiver side as a function of the distance, d , for different beam angles.	114

INTRODUCTION, CONTEXT AND OBJECTIVES

The 20th century witnessed humanity's major achievements in world and space exploration. However, while humankind landed on the moon over 400,000 km away from the Earth, only a small fraction of the ocean has been explored [1]. This is despite the fact that oceanic exploration offers numerous opportunities across various fields, including pollution monitoring, the oil industry, and scientific data collection [2][3][4].

Most of oceanic exploration could be conducted using remotely operated vehicles (ROVs) or autonomous underwater vehicles (AUVs) [5][2]. An ROV is an underwater vehicle controlled remotely by an operator at the surface, while an AUV carries out autonomous missions without continuous contact with the surface [6]. These underwater vehicles typically include a video camera, lighting equipment(s), and various sensors, as shown in figure 1.



Figure 1: Picture of two underwater vehicles. Taken from [7] p.3

To operate these vehicles, a tether¹ is deployed, connecting them to the surface [7]. While this solution is the most commonly used today, it remains impractical [8]. On one hand, the tether is cumbersome, as it restricts the ROV's movement, and is expensive to maintain.

¹i.e., an electric or fiber-optic cable

On the other hand, operating an AUV without a connection to the surface also presents its limitations in its operability and data collection. This issue, first highlighted by Stojanovic in 1996, has led to a resurgence of interest in untethered solutions for underwater vehicles in civilian and commercial sectors, which were previously confined to the military domain [3].



Figure 2: Picture of a ROV tether and its feeder. Taken from [9]

However, whereas classical aerial and terrestrial telecommunication systems use Electromagnetic Waves (EM) in the radio frequency domain to provide wireless communications between systems, the underwater environment restrains considerably the range and capabilities of this method. Therefore, an alternative manner to communicate with underwater vehicles is to rely on acoustic or optical transmission devices [2][10][3][11].

In contrast to classical aerial and terrestrial telecommunication systems, it is not possible to achieve reliable communications by using electromagnetic waves (EMW) in the radio frequency domain in the underwater environment. Therefore, an alternative method to communicate with underwater vehicles is to rely on acoustic or optical transmission devices [2][10][3][11].

Acoustic systems were the first alternative employed to provide underwater communication without physical connexion [12]. They rely on piezoelectric transducers in the ultrasound domain. Initially developed by Paul Langevin in the early 1900s (as shown in figure 3 and figure 4), it remains the most commonly used technique for underwater communication today. It is primarily due to the fact that acoustic systems are robust and offer the longest range with the lowest signal attenuation over distance, even in degraded water environments like harbors and coastal waters where massive particles are present [13][12].



Figure 3: Picture of a Tonpilz acoustic transducer with its piezo stack. Taken from [12] p.10

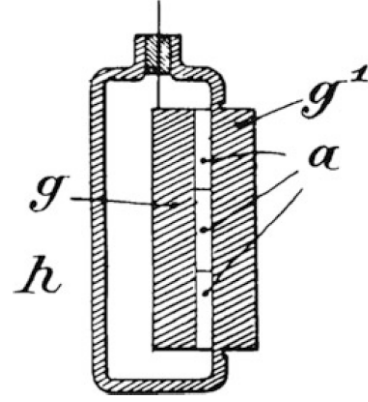


Figure 4: Paul Langevin's patent drawing of an acoustic quartz transducer. Taken from [12] p.5

Acoustic systems present nevertheless several disadvantages. Firstly, the propagation speed of acoustic waves is five orders of magnitude lower than that of radio waves, with a transmission speed of around 1500 m/s in saltwater [10]. This causes long propagation delays as the distance increases, and Doppler shifts when the transmitter or receiver is moving [12][10][13]. Secondly, acoustic systems suffer from high multipath propagation, resulting in transmission delays and strong inter-symbol interference (ISI), sometimes affecting hundreds of symbols [13]. ISI occurs when a transmitted pulse overlaps with adjacent pulses at the receiver, leading to signal distortion and reduced transmission efficiency [14]. Finally, acoustic signals in water are strongly attenuated as frequency increases, as shown in figure 5, which limits the usable bandwidth to the kilohertz range [12][10]. Overall, these limitations restrict the data transmission rate to the kilobits per second (Kbps) range [12][13].

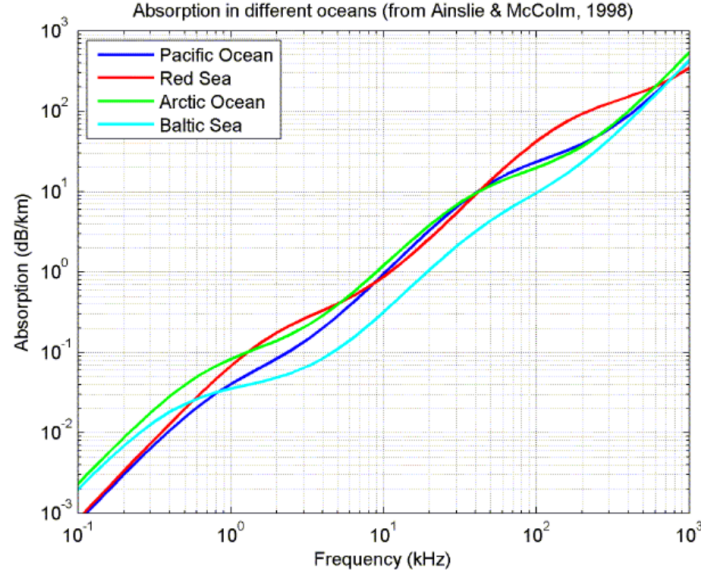


Figure 5: Absorption of sound by seawater function of the sound frequency. Taken from [15], cited in [16]

A second alternative are optical communication systems. They rely on visible light, typically lasers or LEDs, to communicate between systems. Unlike EM waves in the radio frequency domain, visible light is less attenuated in water, especially in the blue-green spectrum as shown in figure 6, which explains why underwater environment appears more blue than red [17].

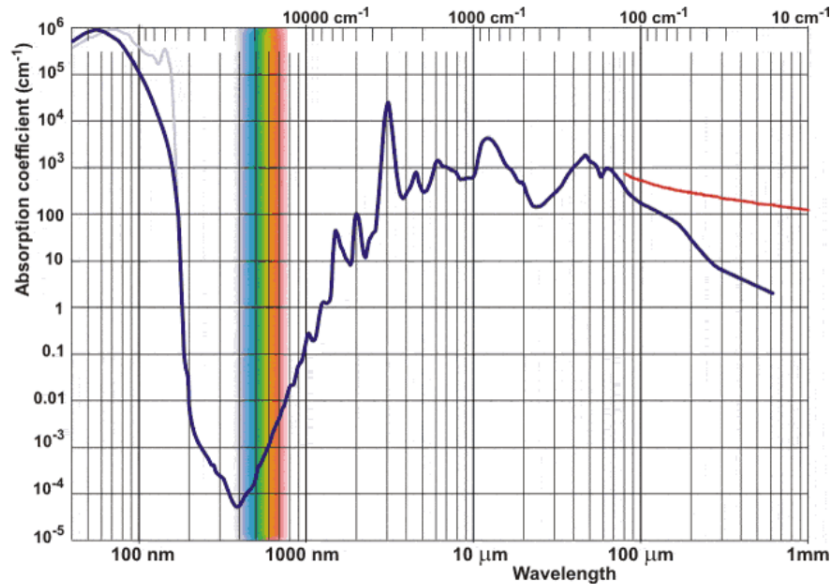


Figure 6: Absorption of visible light by seawater as a function of the EM wavelength. Taken from [18]

The primary advantage of using light as a transmission medium is its high data transmission speed. In fact, its modulation frequencies range in the megahertz (MHz) and data rates can reach megabits per second (Mbps) [13]. However, this technology also faces significant stability issues in unstable environments, such as shallow or turbid water. This results in a short transmission range [11][2]. In harbors or coastal areas where particles are present, light is absorbed or scattered, rapidly reducing signal intensity and thus the communication range [13]. Additionally, precise pointing and alignment are crucial for optical communication. Although the use of high-power LEDs instead of lasers has larger beam width and eases alignment challenges, light can produce unsatisfactory results in this aspect as well.

In practice, a quick market overview shows that most commercially available systems rely on acoustic transmission technology. This is the case, for example, for the Popoto system from Delresearch LLC, shown in figure 7, which starts at over 7,000 USD. Similarly, Teledyne operates with the UTS-9500 system, shown in figure 8[19][20]. While these systems are robust and suitable for telemetry or guidance purposes, their low data transmission rates, typically situated in the Kbps range, makes them unsuitable for transmitting multimedia content. Optical transmission systems are less common, but companies such as Hydromea offer solutions with higher data rates suitable for multimedia transmission, albeit with environmental restrictions and limited range [21].



Figure 7: Picture of the Popoto acoustic emitter. Taken from [22]



Figure 8: Picture of the Teledyne acoustic emitter UTS-9500. Taken from [20]

Despite the availability of these products, the overall commercial offerings appears limited and expensive. More critically, no existing solution provides both a highly reliable transmission system for critical operations and a data rate sufficient for multimedia content transmission. Developing such a comprehensive solution at an affordable cost could offer new perspectives for underwater exploration. A straightforward solution, known as a hybrid system, would combine a low-speed, highly reliable transmission system with a high-speed, less reliable system for multimedia content transmission [13].

Based on these observations, this master thesis aims to initiate the development of a complete communication system for underwater vehicles. Designing such a system represents a significant amount of work, and given the time constraints, this research focuses on the high-speed part of the communication system. It studies the feasibility of implementing a high-speed underwater communication system, as seen in Figure 9, showing a conceptual view of the final system in its underwater environment.

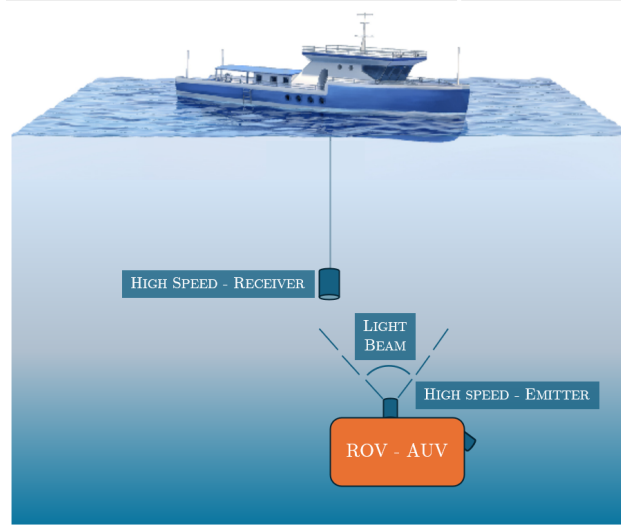


Figure 9: Conceptual view of the high speed system in its underwater environment. Background picture adapted from [23]

According to this objective, this master thesis should demonstrate the feasibility of implementing an underwater communication system presenting the following characteristics :

1. Providing a short range, up to 50 m, untethered transmission system from the ROV or AUV to the receiver ;
2. Having a data rate in the Mbps range suitable for the transmission of multimedia contents ;
3. Having a limited cost in order to be more accessible than existing devices with a total BOM price under 1,000.00 EUR.

This objective raises several questions to be answered though this research:

1. Is acoustic or optical technology suitable to achieve these requirements?
2. Is it possible to provide a solution with a bill of material (BOM) under 1,000.00 EUR?
3. Regarding the chosen technology, what are its operating limitations?
4. What are the advantages and drawbacks of the developed technology?

In order to achieve these objectives and answer the questions, different approaches are considered. The use of acoustic system while the bandwidth is increased up to the MHz range to allow sufficient transmission speed for multimedia content is evaluated. Secondly, optical transmission system can be exploited to provide higher transmission speed with restrained operability in certain underwater environment.

Acoustic system was primarily chosen as - as explained before, it appeared to offer the best compromise between operability and data rate while providing a wider range of operation. Based on this acknowledgement, investigations have been performed with a novel acoustic transmission system proposed by Martins et al. [24][25] that relies on polymer piezoelectric elements (PVDF) instead of traditional lead zirconate titanate piezo elements (PZT). It is supposed to allows to work at higher frequencies and reach the requested data rate. However further investigation proved that the system proposed by Martin et al. did not achieved the expected results. Therefore, the second approach based on optical transmission has been considered.

Following this choice of using light as a transmission medium, the present research has been developed as follow. The first chapter explore the critical importance of understanding underwater light transmission when designing underwater optical communication systems (UWOCS). It covers the fundamental characteristics of UWOCS and concludes with a description of the proposed system. The next chapters focus on the realization of the different parts of the designed communication systems including the emitter and the receiver. Afterwards, the complete system is tested and evaluated. Finally the last chapters discuss the results obtained in regards to the initial objectives and questions, and finally propose some improvement and a conclusion of the present thesis.

CHAPTER 1

UNDERWATER OPTICAL COMMUNICATION SYSTEM

The first chapter of this master thesis explores initially the critical importance of understanding underwater light transmission when designing Underwater Optical Communication Systems (UWOCS). Afterwards, it covers the fundamental characteristics of UWOCS before concluding with the proposed UWOCS design and its specifications.

1.1 Optical transmission in underwater environment

When designing an Underwater Wireless Optical Communication System (UWOCS), a fundamental challenge is ensuring reliable transmission in underwater environment. As explained in the introduction, the electromagnetic spectrum in the visible light domain experiences significantly lower attenuation underwater. However, this advantage is offset by numerous factors related to the underwater environment that can significantly impact the system's performance. Therefore, a thorough understanding of light transmission through water is crucial when developing an UWOCS [26][18].

The first two phenomena essential to understand are absorption and scattering, as they most significantly impact UWOCS performance. When a light beam is emitted to send information to a receiver, some photons do not reach the receiver [27]. The primary cause of this is absorption, where photon energy is converted into another form, such as heat. The second phenomenon, scattering, occurs when photons change direction. Together, these factors contribute to overall light attenuation, as described in figure 1.1 and represented by the law of conservation of energy¹ in equation (1.1) [13].

$$P_e(\lambda) = P_a(\lambda) + P_s(\lambda) + P_t(\lambda) \quad (1.1)$$

The Equation (1.1) shows that when a light beam passes through a small section of the transmission medium Δx , a fraction of the initial power $P_e(\lambda)$ is transmitted as $P_t(\lambda)$, while other fractions are absorbed and scattered, as represented by $P_a(\lambda)$ and $P_s(\lambda)$, respectively [13].

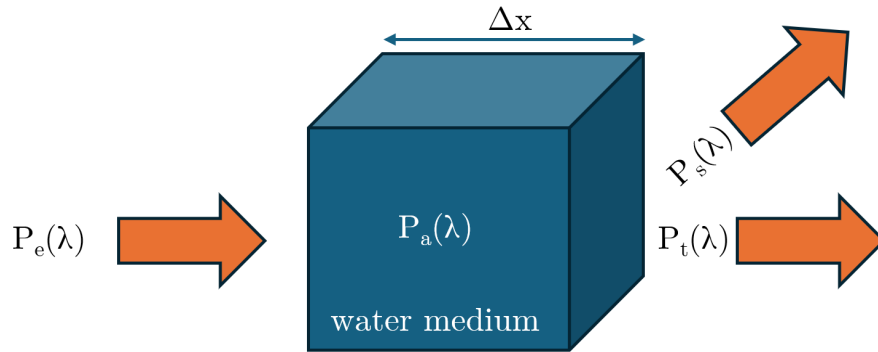


Figure 1.1: Light absorption and scattering through a small piece of water. Image adapted from [18, Chapter 7]

The absorbed and scattered ratios can be defined respectively as [13]:

$$A(\lambda) = \frac{P_a(\lambda)}{P_e(\lambda)} \quad (1.2)$$

and

¹Expressed here as energy per unit of time

$$B(\lambda) = \frac{P_s(\lambda)}{P_e(\lambda)} \quad (1.3)$$

These equations can be reformulated to obtain the attenuation per unit distance, Δx . Assuming Δx becomes infinitely small, the absorption and scattering attenuation coefficients $a(\lambda)$ and $b(\lambda)$ can be obtained as follows [27]:

$$a(\lambda) = \lim_{\Delta x \rightarrow 0} \frac{\Delta A(\lambda)}{\Delta x} = \frac{dA(\lambda)}{dx} \quad (1.4)$$

$$b(\lambda) = \lim_{\Delta x \rightarrow 0} \frac{\Delta B(\lambda)}{\Delta x} = \frac{dB(\lambda)}{dx} \quad (1.5)$$

These two coefficients are combined together to give a global attenuation coefficient $c(\lambda)$:

$$c(\lambda) = a(\lambda) + b(\lambda) \quad (1.6)$$

Finally, the power transmitted, $P_t(\lambda, x)$, coming from an emitter with an initial power $P_e(\lambda)$ over a given distance d , is calculated using the global attenuation coefficient $c(\lambda)$ in the Beer-Lambert law equation[18]:

$$P_t(\lambda, d) = P_e(\lambda)e^{-c(\lambda)d} \quad (1.7)$$

When designing UWOCs, the lower the global attenuation coefficient $c(\lambda)$, the better the transmission. This is directly influenced by the type of water environment and its composition. Although various classifications of water environments exist, five types are commonly considered in UWOCs: pure water, pure sea water, clear ocean water, coastal ocean water, and turbid harbor water [13][28][29][17].

The first types studied, pure water and pure oceanic water, remain mostly theoretical. They illustrate how light propagates through water without other interactions besides water molecules and, in the case of pure sea water, dissolved salts.

In these environments, and within the visible spectrum, only the absorption coefficient $a(\lambda)$ is significant, as the scattering coefficient is negligible, with a magnitude much lower than the absorption coefficient, as shown in figure 1.2 and figure 1.3 [13][17]. As described by Mobley (1994) [17], the behavior of the absorption coefficient as a function of light wavelength can be summarized as follows. In the ultraviolet section of the electromagnetic (EM) spectrum, photons possess enough energy to excite electrons to higher energy levels, resulting in significant absorption. As the wavelength increases and enters the blue region of the EM spectrum, photon energy decreases, and absorption reaches a minimum. In the green region, absorption increases again, as photons excite the fundamental vibrational and rotational modes of water molecules. The differences between pure water and pure sea water become apparent at longer wavelengths, beyond visible EM spectrum.

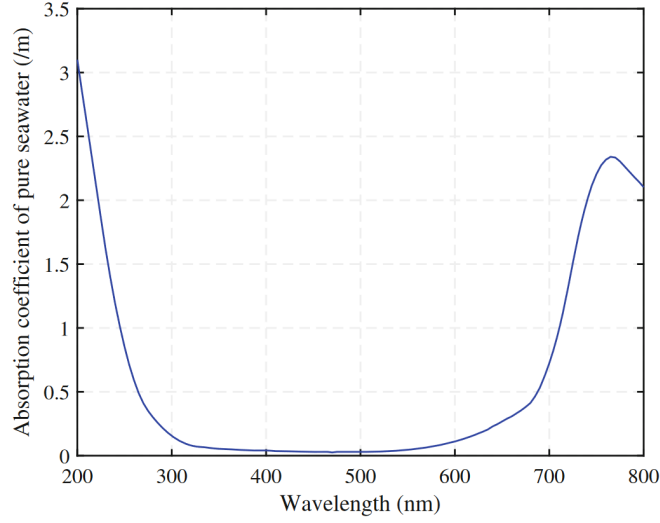


Figure 1.2: Absorption coefficient $a(\lambda)$ as a function of visible EM spectrum for pure sea water. Taken from[18] p.152

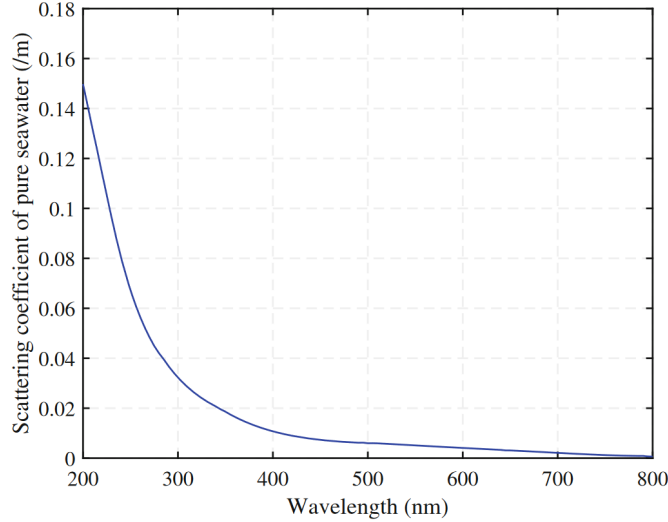


Figure 1.3: Scattering coefficient $b(\lambda)$ as a function of the visible EM spectrum for pure sea water. Taken from[18] p.152

The table A.1 in Appendix A shows the variation of the absorption coefficient for pure sea water. In these two types of water, the blue region of the EM spectrum appears to be the most appropriate for UWOCs, with the lowest attenuation occurring around 450 nm for pure sea water [13].

However, these situations are more theoretical than practical and the three remaining water types — clear ocean water, coastal ocean water, and turbid harbor water — are a better reflection of real-world conditions. In these environments, both absorption and scattering effects occur, primarily due to the presence of additional elements in the water. The elements

affecting UWOCs transmission performance are mainly composed of phytoplankton, detritus, and colored dissolved organic matter (CDOM) such as viruses, bacteria, dead plant tissues, as well as other small particles.

Regarding absorption, these elements absorb shorter wavelengths more effectively, as seen in figure 1.4, figure 1.5, and figure 1.6 [18]. Additionally, phytoplankton absorbs light more successfully in the red domain. Each element thus contributes to absorption, and the total absorption coefficient can be computed linearly as follows [18]:

$$a(\lambda) = a_{psw}(\lambda) + a_{CDOM}(\lambda) + a_{det}(\lambda) + a_{phy}(\lambda) \quad (1.8)$$

With $a_{psw}(\lambda)$, $a_{CDOM}(\lambda)$, $a_{det}(\lambda)$ and $a_{phy}(\lambda)$ the absorption coefficient of respectively CDOM, Detritus and Phytoplankton in pure sea water.

This implies that as the concentration of these elements increases, the effects become more pronounced, shifting the lowest absorption window from blue to the green region of the EM visible spectrum [13].

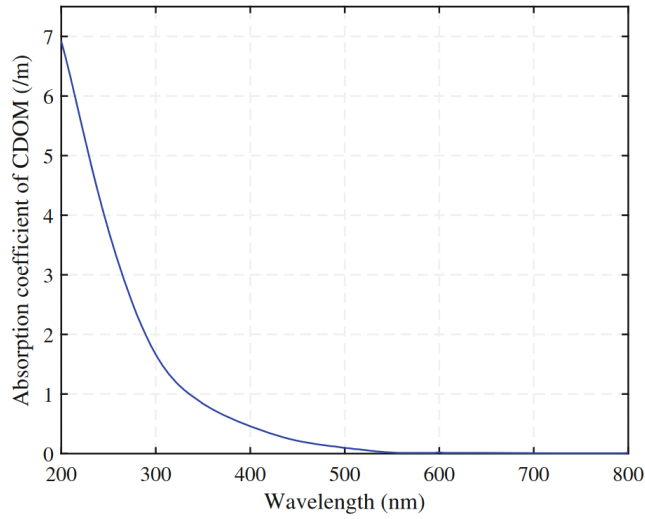


Figure 1.4: Typical absorption coefficient of CDOM as a function of the visible EM spectrum. Taken from [18] p.153

Similarly, the global scattering coefficient can be obtained by the linear addition of the different scattering coefficients of the previously mentioned elements:

$$b(\lambda) = b_{psw}(\lambda) + b_{CDOM}(\lambda) + b_{det}(\lambda) + b_{phy}(\lambda) \quad (1.9)$$

However, when the concentration of matter is sufficiently high, the scattering coefficients of CDOM and pure sea water can be omitted compared to those of detritus and phytoplankton, resulting in [18]:

$$b(\lambda) = b_{det}(\lambda) + b_{phy}(\lambda) \quad (1.10)$$

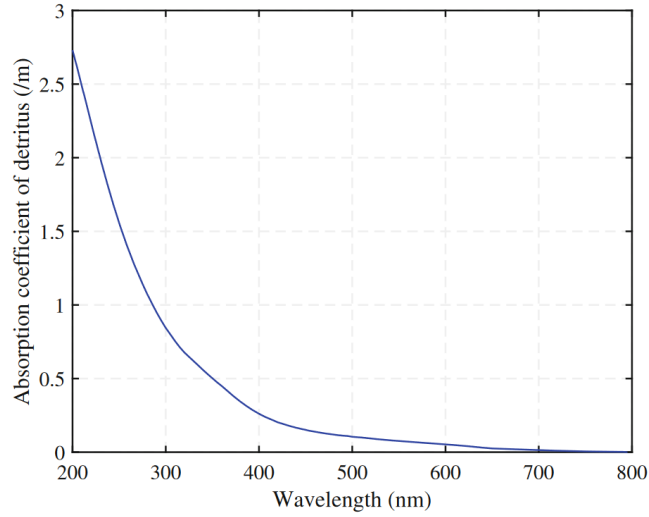


Figure 1.5: Typical absorption coefficient of detritus as a function of the visible EM spectrum. Taken from [18] p.153

Regarding wavelength, as with absorption, the scattering coefficient is greater at shorter wavelengths, such as in the blue region, as shown in figure 1.7 and figure 1.8 [18].

Finally, some temporary phenomenon, such as turbulence effect or large particles like sand, objects or animals can dramatically increase the scattering effect for the two first elements or totally cut the light beam and impact communication for a short period of time [13].

In conclusion, it is evident that as the concentrations of CDOM, phytoplankton, and detritus increase, so do the absorption and scattering coefficients. In terms of wavelength, these elements shift the lowest absorption window from blue to yellow as matter concentration increases. Regarding UWOCs, table 1.1 as adapted from [13], can be used to show the most suitable optical wavelength windows for different water environments. The absorption coefficient is most significant in environments such as pure sea water and clear ocean water, whereas it becomes secondary to scattering in coastal ocean water and turbid harbor water where matter concentration increases. These last two environments might therefore seriously affect the transmission reliability of UWOCs and are consequently less suited for optical communication purposes [13]. The table 1.2 illustrates different absorption coefficients for a wavelength of 450 nm.

Water Type	Suited Operating Wavelength range (nm)
Pure sea/clear ocean	450-500 nm (blue-green)
Coastal ocean	520-570 nm (yellow-green)
Turbid harbor	520-570 nm (yellow-green)

Table 1.1: Suited Operating Wavelength range (nm) for different water types. Adapted from [13]

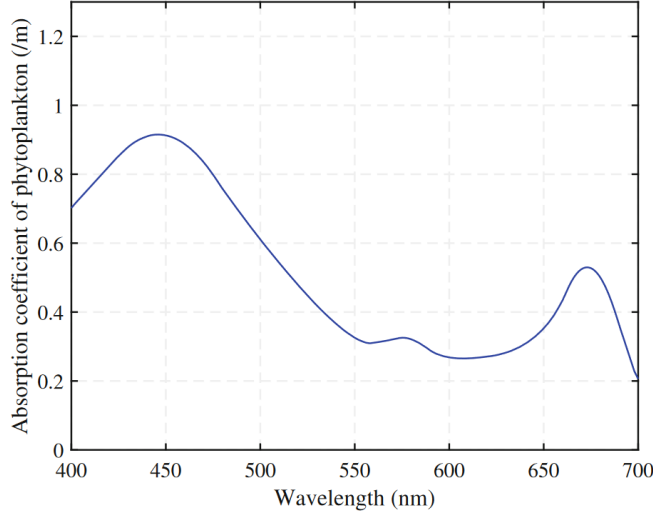


Figure 1.6: Typical absorption coefficient of phytoplankton as a function of the visible EM spectrum. Taken from [18] p.153

Water Type	$a \text{ (m}^{-1}\text{)}$	$b \text{ (m}^{-1}\text{)}$	$c \text{ (m}^{-1}\text{)}$
Clear ocean	0.114	0.0374	0.1514
Coastal ocean	0.179	0.220	0.339
Turbid harbor	0.366	1.829	2.195

Table 1.2: Absorption and scattering coefficients for different water types at a wavelength of $\lambda \approx 450 \text{ nm}$. Adapted from [30] cited in [31].

The next significant phenomenon impacting UWOCS is a direct result of the scattering effect known as Inter-Symbol Interference (ISI). ISI is the distortion of the signal at the receiver side due to the superposition of different symbol windows, caused by a delay due to the scattering of the light beam between the emitter and receiver [18][32]. Fortunately, given the speed of light, the ISI effect is not pronounced to a significant extend at short distances. However, at high data rates or longer distances, the previous symbols might easily overlap with the subsequent ones [33]. This is because increasing the distance extends the delay due to multiple scatterings, while increasing the data rate reduces the symbol time window, making it easier for symbols to overlap. Such observation can be illustrated with figure 1.11 from a study that demonstrated that ISI strongly affects UWOCS communication at a distance of 50 meters for a data rate of 1 Gbps [32]. Finally, as ISI is strongly dependent on scattering, it ensues that higher concentrations of matter will result in stronger ISI effects [13].

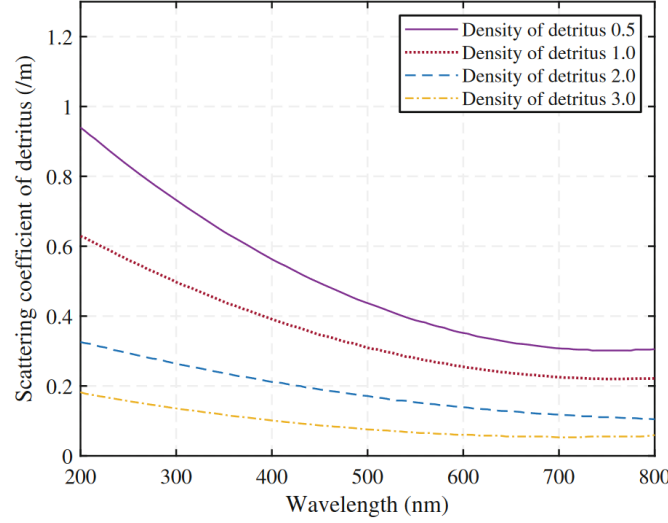


Figure 1.7: Typical scattering coefficient of Detritus function of the EM visible Spectrum. Taken from [18] p.156

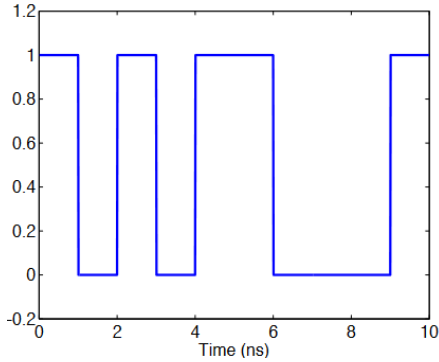


Figure 1.9: Emitted signal

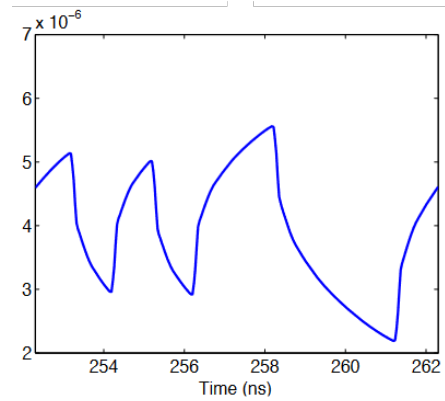


Figure 1.10: Distance = 50 m

Figure 1.11: Signal distortion due to ISI. Taken from [32] p.1626. No ordinate units are provided

In summary, the negative consequences of ISI in UWOCs can be mitigated by reducing the data rate as communication distance increases and by preferring operations in clear ocean water rather than in coastal or turbid harbor waters.

The two remaining effects impacting UWOCs communications are alignment problems and background noise [13][18]. Alignment problems occur when the emitted light beam is poorly oriented and does not reach the receiver. This issue mainly affects the UWOCs systems that relies on lasers as their emitters. Although lasers are more efficient over long distances due to their narrow beam angle, they require a perfect alignment. The second technology used in UWOCs is LEDs, which, although less efficient over longer distances due to their wider beam angle, also tends to be less affected by alignment problems [13].

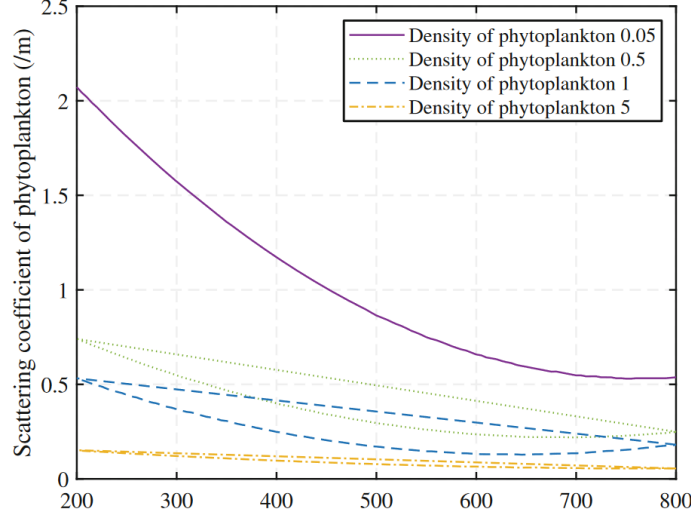


Figure 1.8: Typical scattering coefficient of Phytoplankton function of the EM visible Spectrum. Taken from [18] p.156

Background noise problems occur when the received signal is combined with ambient noise at the receiver side [13]. In the case of UWOCs, ambient noise is primarily caused by sunlight as it provides a constant DC light power to the receiver [13][17]. When designing a UWOCs system, it is therefore important to consider the amount of noise light power reaching the receiver. This is done using solar irradiance, I_{sun} , i.e., the sunlight power per square meter [$\frac{W}{m^2}$]. According to Mobley (1994), the average solar irradiance at sea level under clear skies when the sun is at its zenith is $I_{sunl} \approx 500 Wm^{-2}$, for a wavelength band between 400 nm and 700 nm. This leads to a solar irradiance per unit of wavelength calculated as follows:

$$I_{sun_w} = \frac{I_{sun}}{BW} = \frac{500 \frac{W}{m^2}}{300nm} \approx 1.74 \frac{W}{m^2nm} \quad (1.11)$$

Evidently, the deeper the UWOCs receiver operates and the more it is oriented towards the seabed, the less solar irradiance could interfere, as previously explained through light absorption and scattering.

To conclude this section, the consideration of underwater environment in the design of Underwater Wireless Optical Communication Systems (UWOCs) appears to be critical, and different factors have to be taken into for. Firstly, the optimal wavelength, with the lowest attenuation around 450nm for clear ocean water - the most favorable condition for UWOCs - shifts right as the concentration of particles in the water increases. Then, limited range and data rates help prevent ISI problems, whereas LED technology helps prevent alignment issues. Finally, special attention must be given to ambient noise, primarily resulting from sunlight, during the design of UWOCs.

1.2 Review of Underwater Optical Communication System (UWOCS)

This section provides a brief overview of the fundamental characteristics and components of Underwater Wireless Optical Communication Systems (UWOCS). The aim is to highlight their typical features and critical considerations. Combined with the previous section, this review will help define the framework of the designed system and clarify the choices made in its development.

1.2.1 General overview

Like all communication systems, a UWOCS primarily consists of a transmitter, a receiver, and a transmission medium, which in this case is water [13]. The block diagram in figure 1.12 shows the various components or sections that typically compose a UWOCS system [14][18][13]:

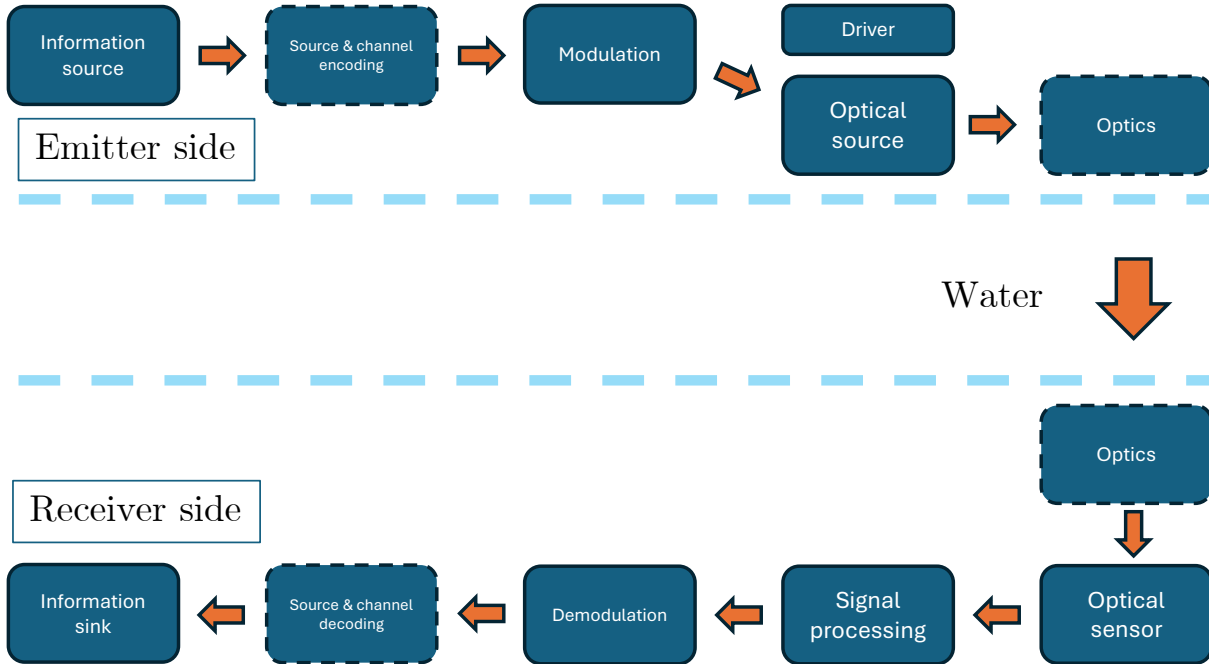


Figure 1.12: Block diagram of usuals components or sections composing UWOCS system. Optional blocks are circled with dotted line. Adapted from [14] and [18]

Some of these blocks are essential, as in all communication systems, while others, such as the optical source, are specific to UWOCS. Additionally, some blocks are optional, depending on the requirements or desired level of reliability [13][14]. To better understand how the information flows from the input of the transmitter to the output of the receiver, each block and section is described below, following the information stream.

1.2.2 Source and channel encoder

When the digital information arrives at the transmitter's input, the bits are typically stored in a buffer, referred as the information source in figure 1.12. They are thus ready to be processed by the transmitter [34]. However, to improve the communication system's efficiency or adapt the signal to the transmission system, two initial optional operations can be performed: source and channel encoding [35][14][13][18].

The first operation, called source encoding, reduces redundancy in the bitstream using compression algorithms [14]. The compressed bitstream is then optimized for the transmission channel. Unlike source coding, channel encoding adds redundancy to increase robustness against transmission errors [18]. Common codes include Hamming code, Reed-Solomon, Forward Error Correction (FEC), and Turbo codes [35][36]. This step can also include additional bits for synchronization purposes.

1.2.3 Modulation

Once the bitstream is conditioned, it must be adapted for transmission over the optical channel [37][18][36]. Each transmission technology requires its own modulation technique, and in optical communication, several modulation schemes can be used, as illustrated in figure 1.13.

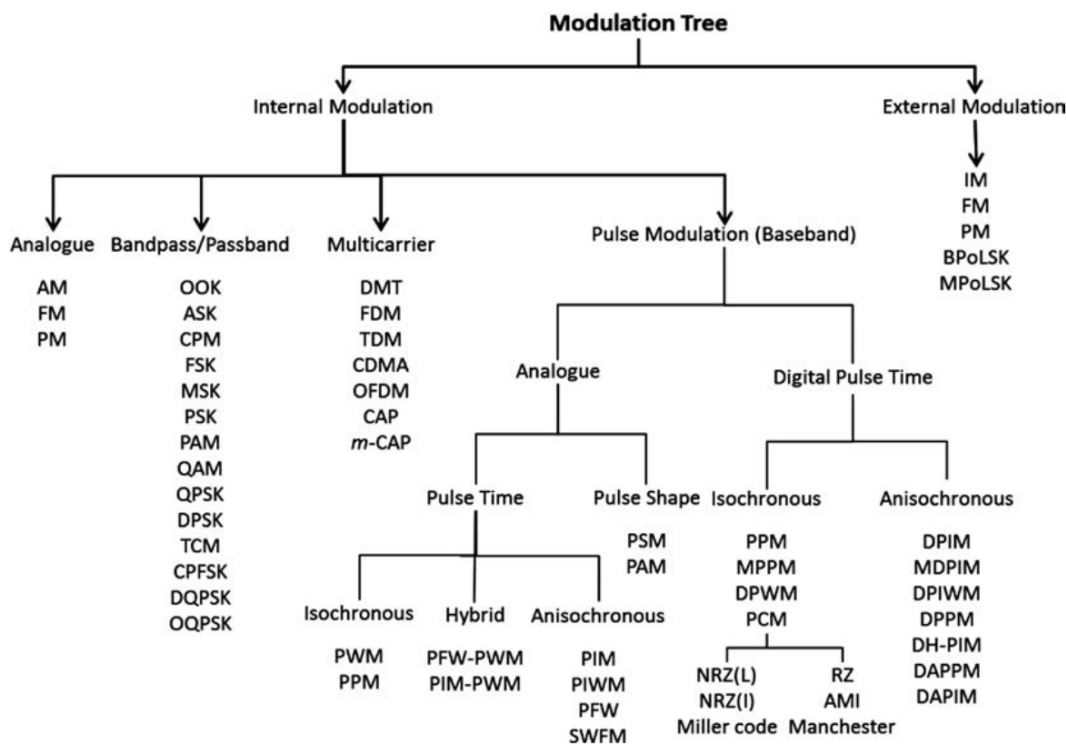


Figure 1.13: Block diagram of usual modulation techniques in UWOC system. Taken from [38] p.158

However, the most commonly used modulation technique in UWOCs is intensity modulation with direct detection (IM/DD), which includes [18][28][13]:

- OOK : On-off keying
- PPM : Pulse position modulation
- PWM : Pulse width modulation
- DPIM : Digital pulse interval modulation

IM/DD is preferred for its simplicity and because the signal is directly recovered by the detector on the receiver side.

Among these, On-Off Keying (OOK) is the simplest and most widely used IM/DD technique [38][18]. OOK is a binary modulation scheme where the light source is on when the transmitted bit is one (1) and off when the bit is zero (0). Thus, binary information is conveyed by the presence or absence of light pulses, as shown in figure 1.14.

While simple, OOK remains less efficient and reliable than other IM/DD techniques, resulting in a higher bit error rate (BER) for the same transmitted power [18]. Another problem regarding OOK is baseline wandering [39]. In the case of OOK the decision about the value of the received data is generally depending if the signal power (or any other electrical value) is above a dynamic threshold called baseline. Generally on the long run the bitstream is equally composed of one (1) and zeros (0) and the emitted power is $P_{OOK} = \frac{P}{2}$ [18] but at some moment the bitstream can be only composed of a sequence of one (1) or zeros (0). This resulting in the baseline being changed and the receiver unable anymore to decode well the transmitted bits. A solution to this is using coding that avoid this situation such as Manchester encoding.

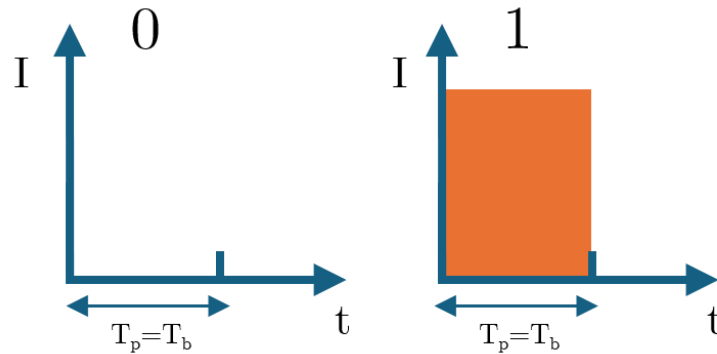


Figure 1.14: Modulation scheme of OOK with T_b the bitstream period and T_s the symbol period. Adapted from [40] p.2 and [18]

To enhance system efficiency, other modulation schemes from the Pulse Time Modulation (PTM) family are introduced [38]. This family includes Pulse Position Modulation (PPM), Pulse Width Modulation (PWM), and Differential Pulse Interval Modulation (DPIM). Unlike

OOK, these techniques modulate information based on the time position or duration of a constant amplitude pulse sequence. This approach also allows multiple bits to be transmitted in one period (single pulse), sending a symbol composed of several bits [41].

PPM is a modulation scheme in which a series of bits is modulated onto a single light pulse of period T_p within a transmission window of period T_s [41][18]. The transmission window is divided into 2^M intervals, where M is the size of the bit sequence, and the pulse's position determines the transmitted bits. For example, the modulation scheme of 4-PPM, shown in figure 1.15, transmits 2 bits simultaneously, resulting in 4 possible emitted symbols, hence the name 4-PPM.

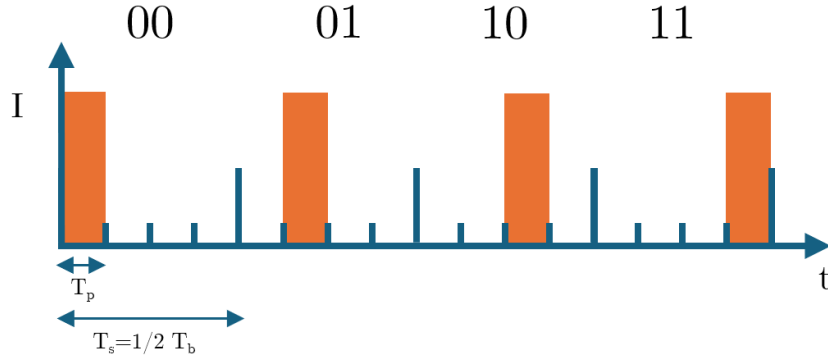


Figure 1.15: Modulation scheme of 4-PPM with T_p the pulse period, T_b the bitstream period and T_s the symbol period. Adapted from [40] p.2 and [18]

PPM uses less power than OOK if more than two symbols are used, with $P_{M-PPM} = \frac{P}{2^M}$, and requires less bandwidth [18]. However, PPM requires perfect timing synchronization at the receiver, and any error can increase the system's bit error rate (BER) [41].

PWM is also widely used in UWOCs to simplify synchronization [18][41]. Like PPM, a series of bits is modulated onto a single light pulse within a fixed transmission window. The difference is that the pulse always starts at the beginning of each transmission window, and the pulse duration determines which symbol is sent. The transmission window is divided into 2^M intervals, with M being the size of the bit sequence, and the pulse duration is a multiple of one interval. The Figure 1.16 shows the modulation scheme of 4-PWM, which transmits 2 bits simultaneously, resulting in 4 possible emitted symbols, hence the name 4-PWM. Since the PWM pulse always starts at the beginning of a transmission window, synchronization is easier, but at the cost of lower power efficiency compared to PPM, as the average pulse duration is longer [18].

The final PTM scheme explored is DPIM. This scheme combines the advantages of the previous modulation techniques while achieving better power efficiency and easier synchronization at the receiver [41][18]. In DPIM, the transmission window is not fixed, and the information is modulated through the time difference between each emitted symbol. The number of time slots between each pulse corresponds to $2^M + 1$, with M being the number of bits sent in one symbol, typically with an additional guard slot to avoid consecutive pulses.

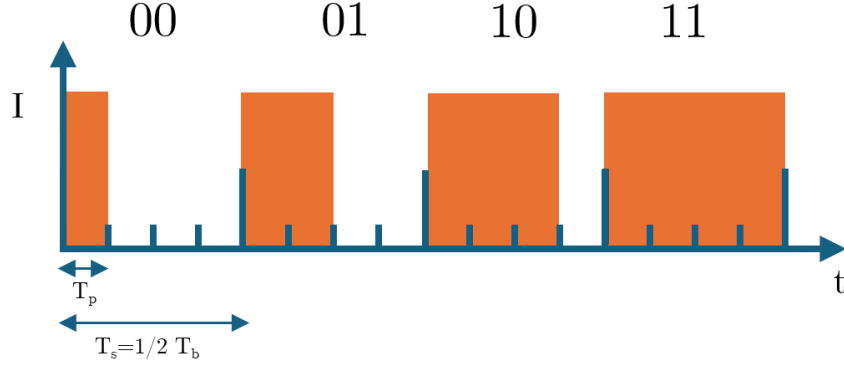


Figure 1.16: Modulation scheme of 4-PWM with T_p the pulse period, T_b the bitstream period and T_s the symbol period. Adapted from [40] p.2 and [18]

Each pulse has its own duration T_p , and each time slot T_s . The maximum symbol transmission duration is then $T_p + (2^M + 1)T_s$ and the minimum is $T_p + T_s$, assuming the presence of a guard slot. The Figure 1.17 shows the modulation scheme of 4-DPIM, which transmits a sequence of 2 bits, resulting in 4 possible symbols.

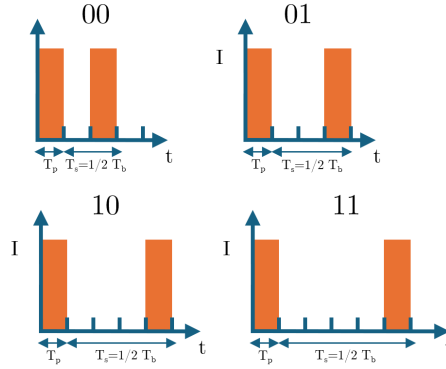


Figure 1.17: Modulation scheme of 4-DPIM with T_p the pulse period, T_b the bitstream period and T_s the symbol period. Adapted from [40] p.2 and [18]

To conclude this section, several popular modulation schemes in UWOCs have been reviewed, along with their advantages and disadvantages. However, it is relevant to point out that this review is not exhaustive; other modulation schemes can be used in UWOCs, such as Phase Shift Keying (PSK), Frequency Shift Keying (FSK), and Orthogonal Frequency Division Multiplexing (OFDM) [18]. While these modulation techniques generally offer higher spectral efficiency and transmission rates, they require much more complex and costly systems and synchronization methods, making them unsuitable for the aims of this master thesis [13].

1.2.4 Optical source and driver

Following the modulation step, the signal is now adapted for optical transmission and needs to travel from the transmitter to the receiver through the underwater channel. To perform this step, the electrical signal is converted into an optical signal using either laser or LED

technology [13]. Each technology has its own advantages and disadvantages and should be selected based on the goals of the UWOCs project.

On the one hand, lasers provide generally a higher output intensity emitted to the receiver. This is due to ultra narrow beam with a tight spectral band [41]. They have also ultra fast switching speed and offer additional modulation technique due to the coherent nature of the emitted light. Therefore, lasers are certainly the best choice for ultra long distance and ultra high speed application [13]. However, laser source suffer from multiple drawbacks such a high cost and shorter lifetime in comparison with LED technology. Additionally, lasers' need of having a perfect alignment between the transmitter and the receiver due to their narrow beam is an impediment [41]. A solution to avoid perfect alignment is to use electronic or mechanical beam steering system but this implies high implementation costs and is complex to achieve [13].

On the other hand, LED systems are more simple to implement thanks to their lower cost and wider light beam angle, which can be managed by optics after the LED source, reducing the alignment problem encountered with laser [41][13]. The downsides are a lower power emitted in the receiver direction, a larger spectral bandwidth and lower switching speed resulting of a shorter range and lower transmission speed in comparison with laser technology as showed on table table 1.3.

Elements	Laser	LED
Transmission speed	Ultra high speed (Gbps)	Low transmission speed (Mbps)
Cost	High	Low
Complexity	High	Low
Light nature	Coherent	Incoherent
Lifetime	Shorter	Longer
Alignment requirement	High	Low

Table 1.3: Comparison of Laser and LED technologies for UWOCs.

Finally, both laser and LED source require a specific driver circuitry in order to switch the modulation signal into a suitable power signal[13].

1.2.5 Optical sensor and optics

Following its emission, the light beam go trough the underwater channel, is attenuated as described in the previous section and only a small part of the initial power reach the receiver side. In order to detect this small amount of power and convert it into an electrical measure, some light sensors are used. Many existing light sensors are suitable for UWOCs but as the irradiance, I_r ($\frac{W}{m^2}$), the luminous power per square meter, is weak it request sensors with high photosensitivity. This implies a good ratio between the output signal and the optical power[42][38].

In UWOCs, the two most popular sensors used are PIN photodiode (PIN) and avalanche photodiode (APD) [38][13]. PIN photodiode is a classical PN junction semiconductor material with a low n-doped intrinsic region. The PIN photodiodes are generally used in reverse bias mode and like APD output a current proportionally to incident light power reaching the sensors. The main advantage of PIN photodiode in comparison with APD are their lower cost and easiness of implementation, mainly due to their lower bias voltage. The figure 1.18 depicts an example of a PIN photodiode S1223 from Hamamatsu available at a price of 23.76€ on RS-online [43].

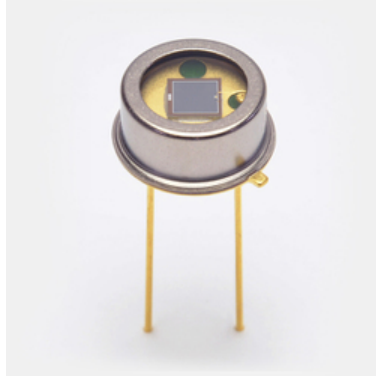


Figure 1.18: Picture of a PIN photodiode S1223 from Hamamatsu taken from [44]

APDs have an additional internal gain due to the avalanche effect, making them more suitable when the received power is very low [13][18]. Like PIN photodiodes, APDs are used in reverse bias mode but require higher reverse bias voltage, necessitating more complex circuitry. APDs may also require additional protection regarding this high voltage bias [13][38]. The Figure 1.19 shows an APD from Hamamatsu, priced at 450 USD on Edmund Optics [45], and its control circuitry is illustrated in figure 1.20. While the price of the APD is higher, it provides an internal gain of $G = 20$ compared to the S1223 photodiode [44][46]. In summary, PIN photodiodes are more suitable for short-distance, low-cost systems, while APDs, though more complex and expensive, are used for longer-distance transmission systems [13].

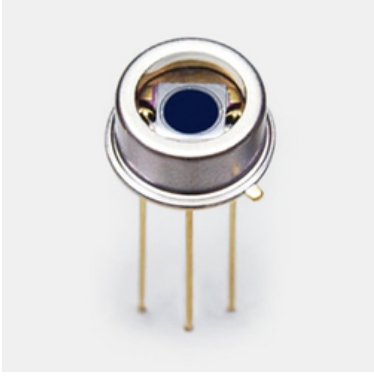


Figure 1.19: Picture of an APD S5344 from Hamamatsu taken from [46]



Figure 1.20: Picture of an APD control circuit from Hamamatsu with the the high voltage unit on the left of the picture. Taken from [47]

In addition to PIN photodiodes and APDs, other sensors can be used in UWOCs, such as photomultiplier tubes (PMTs) [41]. While these sensors offer exceptional sensitivity and low noise levels, they are highly expensive, fragile, and easily damaged when exposed to high light levels.

A recent alternative to PMTs, increasingly considered in UWOCs, is the silicon photomultiplier (SiPM) [23]. A SiPM consists of a dense array of single-photon avalanche diodes (SPADs), which essentially function as photon counters operating in Geiger mode [48]. SiPMs offer performance comparable to PMTs without the aforementioned drawbacks, making them more suitable for future UWOCs implementations [48].

Finally, it is notable that all the presented systems can be combined with a concentrating lens. This would increase the received light power and a bandpass filter in the EM spectrum as to receive only the wavelength emitted by the light source, thus avoiding sunlight and other optical noise present at other wavelengths [13].

1.2.6 Signal Processing

After the light is converted to an electrical signal by the sensors, the resulting current is typically very weak and needs to be amplified [38]. The first amplification stage usually involves a Transimpedance Amplifier (TIA) to convert the current into a voltage signal [49][50][38]. The TIA is essentially an Operational Amplifier (Op-Amp) with a feedback resistor, R_{FB} , connected between its inverting input and output. The incoming signal is also connected to the inverting input, so the current flows through the feedback resistor, creating a potential difference between the inverting input and the output of the Op-Amp. A reference voltage is connected to the non-inverting input of the Op-Amp, ensuring that the inverting input has the same reference voltage, thus setting the output signal, V_{out} , as:

$$V_{out} = V_{ref} - I_{sensor} R_{FB} \quad (1.12)$$

where I_{sensor} is the current flowing out of the optical sensor, and R_{FB} is the resistance of the feedback resistor, which, as shown in equation (1.12), is also the I/V (Current to Voltage) gain of the Op-Amp [49][38]. Although the TIA concept is straightforward in theory, its practical implementation requires careful attention. The TIA is sensitive to any capacitance at its inputs, and the photodiode capacitance may cause instability. A feedback capacitance may be added to ensure the Op-Amp's stability. Additionally, the TIA PCB layout should be designed carefully to avoid additional parasitic capacitance [51]. A schematic of an Op-Amp used as a TIA is shown in figure 1.21.

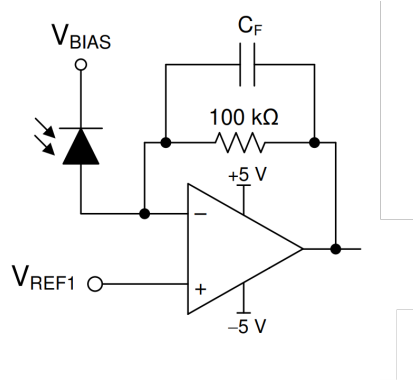


Figure 1.21: Schematic of a ultra high speed Op-amp OPA818 used as TIA with its feedback resistor and capacitance. Taken from [51] p.1

After this first stage of amplification, the signal is now a voltage, but nevertheless it may still remain small. Therefore, additional Op-Amps may be added to further amplify the signal to a usable level [52].

1.2.7 Demodulation Source and channel decoder

Once the signal is processed, it may need to be demodulated, depending on the modulation scheme chosen earlier. Then, source and channel can be decoded to retrieve the original bitstream, and be ready to use in an information sink [53][18].

1.3 Proposed UWOCs design and specifications

Given the information provided in the previous two sections, the design of the UWOCs will presently be specified. This will be done in line with the objective of this thesis into account, which consist in demonstrating the feasibility of creating an operational underwater communication system with the following criteria:

1. Providing a short range, up to 50 m, untethered transmission system from the ROV or AUV to the receiver.
2. Having a data rate in the Mbps range suitable for the transmission of multimedia contents.
3. Having a limited cost in order to be more accessible than existing devices with a total BOM price under 1,000.00 EUR.

To meet these objectives, both an optical emitter and receiver have to be designed. Regarding the emitter, the system will produce a modulated voltage signal at its input, considering the chosen modulation scheme. A power stage will then process this signal to ensure that it appropriately drives the light emitter. Finally, optical lenses will be added to manage the light beam.

As for the receiver, the system will capture the light signal through its sensor. This signal will then be properly amplified and shaped to provide an appropriate output signal ready for demodulation. The various blocks of the designed UWOCs are depicted in figure 1.22, and the different design choices are explained below. In order to simplify the reading, please note that all assumptions provided below, unless otherwise cited, are discussed in section 1.1 and section 1.2.

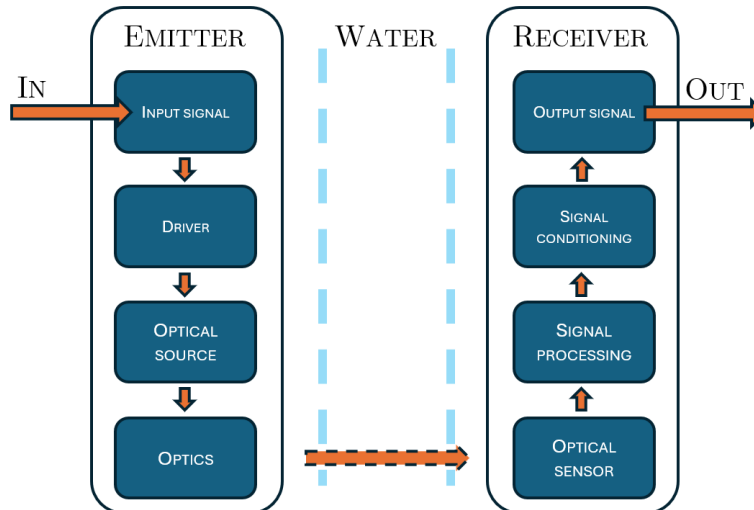


Figure 1.22: General block diagram of the designed UWOCs

Since the modulation scheme influences the entire design, it is evidently the first aspect to be selected. Considering the various modulation techniques discussed in section 1.2 and the

cost and complexity constraints defined in the objectives of this thesis, Intensity Modulated Direct Detection (IM/DD) is chosen.

While On-Off Keying (OOK) is the simplest modulation scheme suitable for UWOCs, several of its characteristics make it incompatible with the system this thesis aims to implement. Firstly, OOK does not constrain pulse duration when multiple "1"s or "0"s are transmitted, leading to baseline wandering. Additionally, if the pulse duration extends, the optical source might experience currents that are safe for short pulses but could damage the transmitter over longer periods². Furthermore, using a high-pass filter at the receiver to mitigate DC noise from environmental sources like sunlight could result in signal distortion. Lastly, OOK is limited to transmitting binary information, whereas other IM/DD schemes can transmit multiple bits per symbol, increasing power efficiency—a crucial factor given the limited autonomy of ROVs and AUVs [54]. For all these reasons, Differential Pulse Interval Modulation (DPIM), derived from Pulse Time Modulation (PTM) schemes, is preferred due to its numerous advantages, such as an easy synchronization, a fixed pulse length, and a better power efficiency.

As the modulation scheme is selected, the next step is to determine the pulse duration (T_p), the time intervals between the pulses ($T_i(S)$) with "S" representing the emitted symbol, and the symbol definitions. With a 1 Mbps bitrate objective as a lower bound and considering frequency limitations such as Inter-Symbol Interference (ISI) and LED bandwidth³, the pulse duration is set at $T_p = 500$ ns. To prevent longer pulse lengths, a guard slot is added, and all empty slots have the same duration as the pulse. An 8-DPIM scheme is chosen, transmitting 3 bits of information per emitted symbol to achieve the targeted bitrate. The different symbols, their corresponding bits, and the time intervals are shown in table 1.4, with the modulation scheme illustrated in figure 1.23.

Symbols (S)	Emitted bits	Pulse duration (T_p) [us]	Total interval (T_i) [us]
A	000	0.5	1.0
B	001	0.5	1.5
C	010	0.5	2.0
D	011	0.5	2.5
E	100	0.5	3.0
F	101	0.5	3.5
G	110	0.5	4.0
H	111	0.5	4.5

Table 1.4: Symbol, Bits, Pulse Duration, and Total Time Interval for various codes.

This configuration results in an average bitrate calculated as follow :

$$Bitrate = \frac{S_{nb}N}{\sum T_i(S)} = 1.09Mbps \quad (1.13)$$

²For consistency, this is explained in the receiver and transmitter section of this master thesis

³For consistency, the choice of emitter source is explained below

With $S_{nb} = 8$, the number of symbols and $N = 3$, the number of bits emitted per symbol emitted. As seen in equation (1.13) the average bitrate meet the specified criterion. Finally, if needed some additional slot might be added for synchronization purposes or when no signal is transmitted.

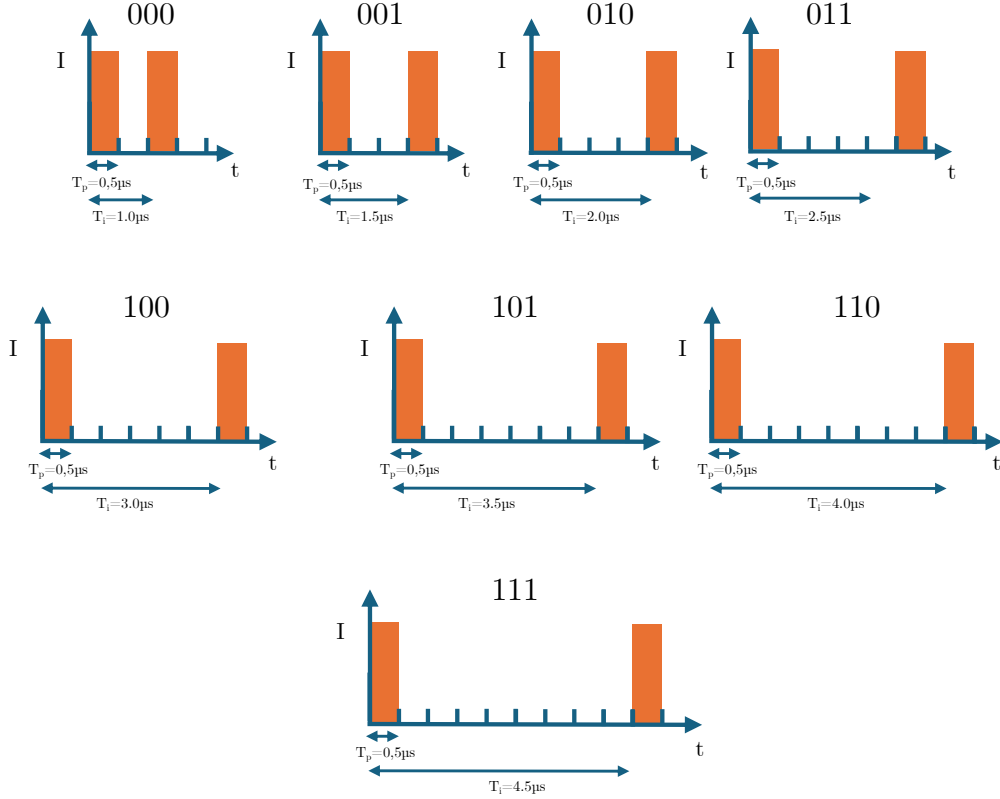


Figure 1.23: 8-DPIM scheme selected for the designed UWOCs with T_p the fixed pulse rate and T_i the symbol duration.

Following the selection of the modulation scheme, the next step is to specify the emitter light source. As previously discussed, the two available technologies for UWOCs are lasers and LEDs. Although lasers are more powerful, their higher cost, increased complexity, and alignment difficulties make them unsuitable for the objectives of this thesis. Consequently, high-powered LEDs are preferred. LEDs offer a broader beam, that simplifies alignment. Despite their lower operational frequency, they remain sufficiently fast for the defined modulation scheme. As detailed in section 1.1, light-powered underwater communication systems operate better in clear ocean water. Consequently, the LED wavelength will be selected within the range $\lambda_{LED} \in [450 \text{ nm}; 500 \text{ nm}]$, and considering the typical power used in UWOCs, a minimum luminous power of $P_{light} \geq 1 \text{ W}$ is preferred. A suitable driver will be designed to power the LEDs, taking the 8-DPIM square signal as input and outputting the appropriate power signal to the LEDs. Regarding the light beam configuration, a combination of a narrow LED beam with $\Phi_b \approx 15^\circ$ and a wider beam with $\Phi_b \approx 90^\circ$ will be utilized. This configuration provides a sufficiently large functional area when the receiver is close to the emitter using the wider beam, and enough power when the receiver is farther away by using

the narrow beam. The complete emitter block diagram is shown in figure 1.24.

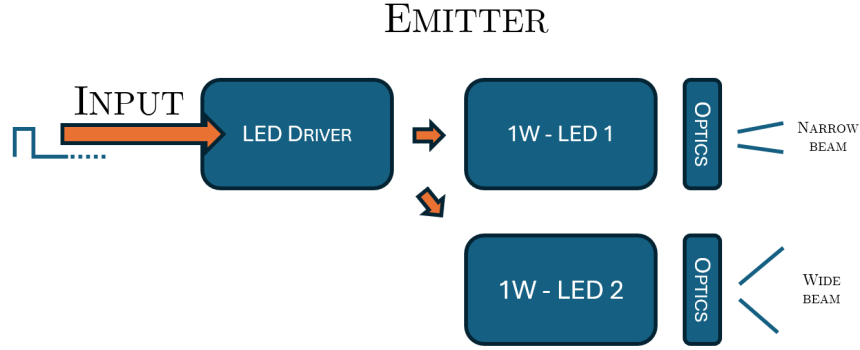


Figure 1.24: Emitter design specification.

On the receiver side, the developed UWOCS will use a Silicon Photomultiplier (SiPM) as the light sensor. As discussed previously, UWOCS typically employ PIN or avalanche photodiodes as light sensors, and at the time of writing this master thesis, research on SiPM sensors in UWOCS appears limited. Therefore, investigating the SiPM's high internal gain and ability to detect ultra-low light sources could provide valuable insights. Following light detection, the signal will be amplified using operational amplifiers (Op-Amps). Typically, light sensors generate a current signal that is amplified at their first stage with a Transimpedance Amplifier (TIA), as previously explained. However, as will be further detailed in the receiver design chapter, the use of a TIA may not be suitable when employing an SiPM sensor. Consequently, the designed UWOCS will use classical Op-Amp amplification stages with a resistor in series with the SiPM sensor. Lastly, a comparator will be used for the final stage, providing a digital output that clearly distinguishes between high and low levels based on the presence or absence of a pulse[55].

To conclude the UWOCS design specification, a table summarizing the complete specifications is provided in table 1.5.

Specification	Details
Communication Range	Up to 50 meters
Data Rate	1.09 Mbps
Total BOM Cost	Under \$1,000.00 USD
Modulation Scheme	IM/DD 8-DPIM
Emitter Type	High-powered LEDs
LED Wavelength	450 nm - 500 nm
Luminous Power	≥ 1 Watt
Beam Configuration	Narrow beam ($\approx 15^\circ$) and wider beam ($\approx 90^\circ$)
Light Sensor	Silicon Photomultiplier (SiPM)
Amplification	Operational Amplifier stages
Final Output Stage	Comparator providing digital output
Operational Environment	Clear ocean water

Table 1.5: Synthesis of the UWOCs Design Specifications

CHAPTER 2

PROTOTYPE DESIGN AND REALIZATION

This chapter details the design and conception of the underwater optical communication system. It begins with the design and the construction of the receiver, before following with the elaboration of the transmitter. The chapter concludes with the design and completion of the power supply auxiliary circuits.

2.1 Receiver module

This first section focuses on the receiver. It starts with a theoretical overview of the Silicon Photomultiplier (SiPM) and the rationale behind its selection. Once the choice of the sensor is settled, the design and specification of the amplification stages are discussed, followed by the development of the comparator stage. Finally, the design and fabrication of the Printed Circuit Board (PCB) for the complete system are covered.

2.1.1 Silicon Photomultiplier sensors (SiPM)

The light sensor used in the receiver module is a Silicon Photomultiplier (SiPM). The SiPM consists of an array, as shown in figure 2.1, composed of a large number of Single Photon Avalanche Diodes (SPADs) placed in series with quenching resistors, as illustrated in figure 2.2 [48]. Each SPAD, along with its quenching resistor, is referred to as a microcell. SiPMs performance is comparable to that of photomultiplier tubes, as described in the UWOCs review section, but without such drawbacks as an high cost, fragility, a larger size, and the requirement for very high bias voltages [56].

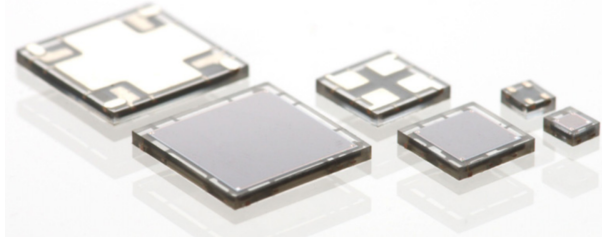


Figure 2.1: Picture of SiPM microcells from ON Semiconductor. Taken from [48] p.1

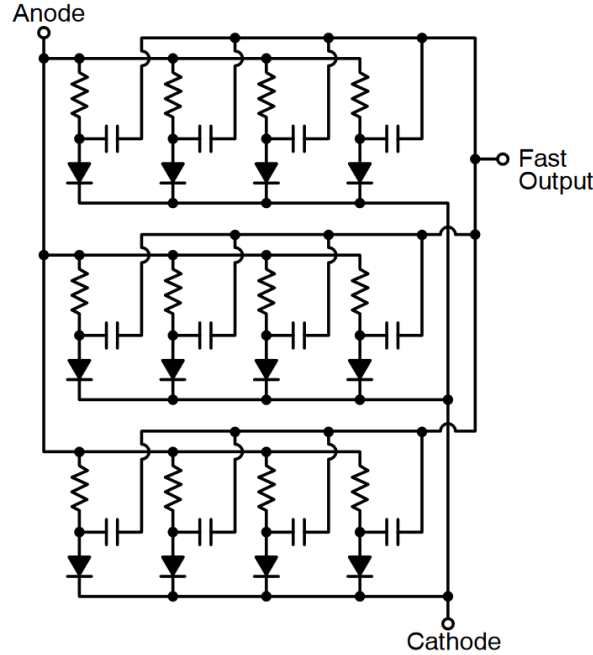


Figure 2.2: Schematics of a SiPM with the SPAD diodes and their quenching resistances in series. Taken from [48] p.1

A SiPM sensor works as follow : when a photon hits one of the SPAD, it might then be absorbed and afterwards the photon transfers its energy to an electron that moves from its valence band into the conduction band and creates an electron-hole pair (charge carriers)[56]. Since the SPAD is reverse biased, an electric field exists within the depletion region, accelerating the charge carriers toward the anode (for holes) and the cathode (for electrons). It results in a current flow through the SPAD photodiode.

If the SPAD is reverse biased over the breakdown voltage, the electric field present in the depletion region is high and the charge carriers are sufficiently accelerated to create another electron-hole pair [56]. This process is called "impact ionization" and means that a single absorbed photon can trigger a self-sustained ionization, leading to an amplified current flow through the SPAD photodiode. Once the current starts flowing, it doesn't stop on its own; thus, a quenching resistor is placed in series with the SPAD photodiode to bring the SPAD's voltage below its breakdown voltage (V_{br}), halting the avalanche process. The photodiode

voltage can then return to its bias level, ready to detect another incoming photon. This process is called a Geiger discharge, and as such the SPAD operates in Geiger mode, with the operating cycle depicted in figure 2.3.

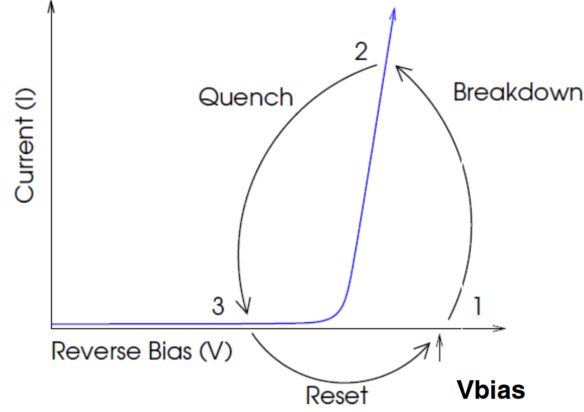


Figure 2.3: Spad photodiode operating cycle in Geiger mode. Taken from [56] p.1

It is important to highlight that a SPAD photodiode operating in Geiger mode functions as a binary device with "off" and "on" (or "fired") states [56]. The "on" state is characterized by a current flowing through the photodiode when it is hit by an incoming photon, while the "off" state occurs when no current flows. This implies that even if multiple photons hit the photodiode, the current magnitude does not provide any additional information at the single SPAD photodiode level.

However, since the SiPM consists of a dense array of SPAD photodiodes placed in parallel, the magnitude of the current flowing through the SiPM sensor depends on how many individual SPAD photodiodes have fired [56]. Consequently, the entire SiPM sensor provides information about the magnitude of the incoming photon flux. When photons hit the SiPM sensor, a current pulse is generated, proportional to the number of photons, as shown in figure 2.4.

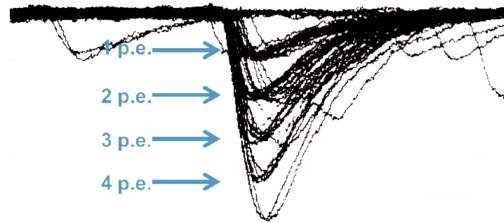


Figure 2.4: Different voltage pulses superimposed related to the current flowing through a SiPM sensor when illuminated by different level of pulsed light. Taken from [56] p.3

As seen in figure 2.4, the pulse has a specific shape and duration due to the avalanche process, which determines a rise time, and a longer fall time, also known as recovery or

decay time. It allows the SPAD photodiode to return to its initial state before detecting another incoming photon [56]. The recovery time is determined by the microcell recharge time constant, given by:

$$\tau_R = C_d (R_q + R_s \cdot N) \quad (2.1)$$

Where C_d is the individual capacitance of each microcell, R_q is the quenching resistance, N is the number of microcells in the SiPM array, and R_s includes all possible resistances in series with the SiPM sensor [56]. The Figure 2.5 shows the pulse shape voltage of an SiPM sensor in series with a 16-ohm resistor, with a recovery time on the order of tens of nanoseconds.

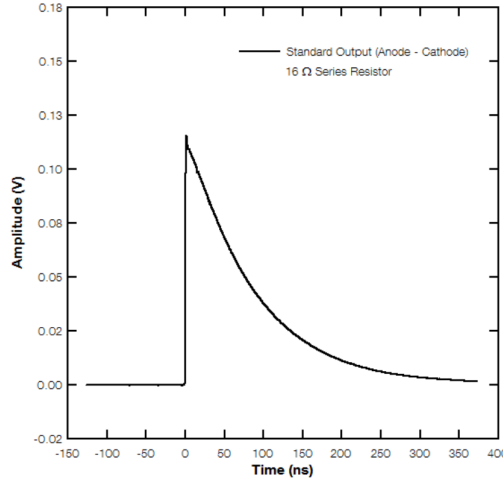


Figure 2.5: Pulse shape voltage of a SiPM sensor in series with a 16 ohm resistor. Taken from [48], p. 3.

In the context of the implemented UWOCs system, the general recovery time of the SiPM sensor is significantly shorter than the pulse period of the DPIM modulation, with $T_p \gg \tau_R$. The SiPM outputs a continuous current depending on the incoming light received by the sensor, according to the following relation [57][56]:

$$I_{\text{out}} = G e M \frac{1 - e^{-\text{PDE}(\lambda, V) \frac{P_{\text{SiPM}}}{E_p(\lambda)} \frac{t_p}{M}}}{t_p} \quad (2.2)$$

Where :

- I_{out} : the output current
- G : the gain of the SiPM sensor, $G \approx 10^6$
- e : the electron charge
- M : the number of microcells present in the SiPM sensor

- $PDE(\lambda, V)$: the photon detection efficiency, which is roughly the probability that an incoming photon will initiate an avalanche process. The PDE depends on λ and V , the bias voltage.
- P_{SiPM} : the light power arriving on the active surface of the sensor
- $E_p(\lambda) = \frac{hc}{\lambda}$: the photon energy
- $t_p = 2.2\tau_R$: the pulse pair resolution, which is roughly the time needed for the microcell to recover from 90% to 10%

The Equation (2.2) shows that the output current depends on many factors and remains mostly linear if the incoming light power stays within a low range [58]. If the light power increases beyond a certain level, all the microcells fire, and fewer incoming photons trigger an avalanche process when hitting the sensor. This situation is illustrated in figure 2.6. Another critical point is that the output current and the linear range of the SiPM sensor also depend on the microcell recovery time τ_R . According to equation (2.1), an increase in any resistances in series with the SiPM sensor will increase the microcell recovery time and, consequently, decrease the linear range of the sensor.

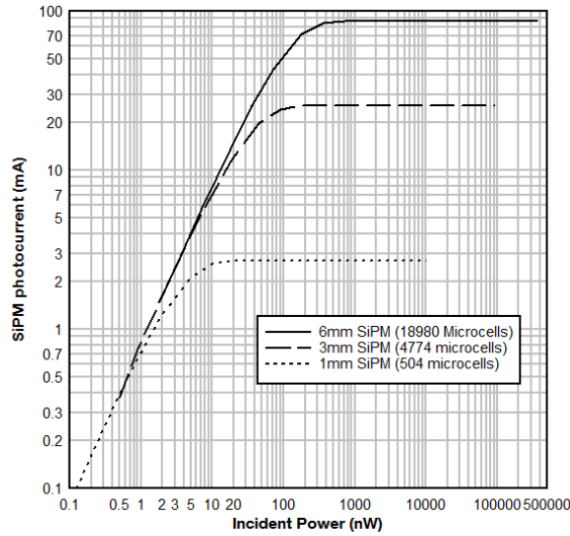


Figure 2.6: The SiPM output current function of the received light power. Taken from [56] p.9

Finally, it is necessary to take into account that, like most sensors, the SiPM has various noise sources. The primary noise sources are dark count rate and optical crosstalk [56]. Dark count rate occurs when a microcell of the SiPM sensor fires due to the thermal generation of an electron, making it the most significant source of noise in SiPM sensors. Crosstalk happens when adjacent microcells fire due to the firing of a neighboring microcell, even though they should not. Since both noise sources are proportional to the bias voltage, lowering the bias voltage can mitigate these effects, but it will also reduce the sensor's photon detection efficiency (PDE).

Sensor selection

Following this brief theoretical review of Silicon Photomultiplier (SiPM) technology, it is then needed to select an appropriate sensor. After surveying the market, it emerges that SiPM sensors are less popular than traditional photodiodes. The first criterion for selection is the certainty that the chosen SiPM sensor is readily available and in stock on various marketplaces such as Farnell, Mouser, or Digikey. Additionally, another criterion is the ability of the manufacturer to provide comprehensive documentation for their SiPM sensors, and that they could ideally offer evaluation boards. This is particularly relevant as most SiPMs use Ball Grid Array (BGA) connectors or similar products, which require advanced equipment and manufactured PCBs for proper utilization [59]. From a technical perspective, the selected SiPM sensor must then have a sufficiently low operating voltage, ideally below 30V, to comply with the IEC 60364-7-702 standard [60], given that the system will operate in an underwater environment. Furthermore, the sensor should be capable of handling a wide range of incoming light power amplitudes.

For this last reason, before selecting the sensor, it is essential to estimate the range of irradiance, i.e., the light power per square meter $I_r[\frac{W}{m^2}]$, at the receiver side as a function of d , the distance with the emitter. This taking into accounts the requirements and postulates from section 1.3 with an operational range between 1 m and 50 m in a clear ocean water, a light power at the output of the emitter of minimum 1 W and an emitter light beam angle Φ_b comprised between 15° and 90° .

First, the luminous power at the receiver side, $P_r[W]$, as a function of its distance, $d[m]$, from the emitter is calculated using the Beer-Lambert Law ¹:

$$P_r(\lambda, d) = P_e e^{c(\lambda) d} \quad (2.3)$$

Here, the attenuation coefficient for clear ocean water is $c = 0.151$, in the wavelength range suitable for UWOCs transmission, as defined in the previous section.

Then the circular area at the receiver side $A_r(\Phi_b, d)$ function of the beam angle and distance is calculated as :

$$A_r(\Phi_b, d) = \pi (d \tan(\Phi_b/2))^2 \quad (2.4)$$

Finally, using the equations above, the irradiance at the receiver side, $I_r(\lambda, d, \Phi_b)[\frac{W}{m^2}]$, is calculated:

$$I_r(\lambda, d, \Phi_b) = \frac{P_r(\lambda, d)}{A_r(\Phi_b)} \quad (2.5)$$

As seen on figure 2.7 the irradiance, $I_r(\lambda, d, \Phi_b)$ varies with nine and seven decades of magnitude within the requested range and with respectively a beam angle of $\Phi_b = 90^\circ$ and $\Phi_b = 15^\circ$ which is very large².

¹Defined in section 1.1.

²Appendix A, table A.2 show the detailed numerical values for different distances

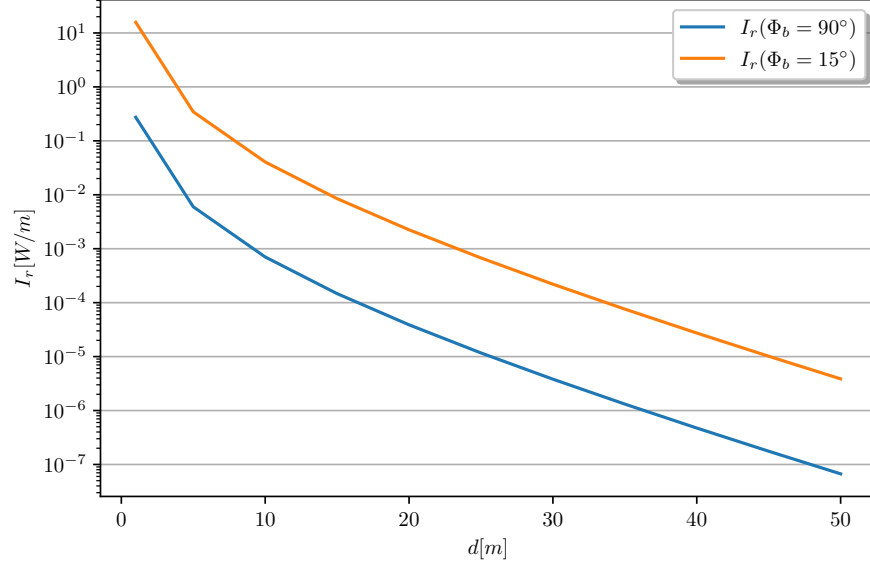


Figure 2.7: The SiPM sensor in serie with a resistance R_s . Adapted from [52] p.8

Based on these results and the different requirements outlined previously, the SiPM sensors from ON Semiconductor appear to be the most suitable for the implemented system, more specifically the SiPM J-series 600035. This model features the largest array of microcells among existing ON Semiconductor, as well as a high Photon Detection Efficiency (PDE) serving excellent low-light detection, and robust tolerance to high luminous power without saturating [57][61]. Moreover, evaluation boards are available for this sensor, which is advantageous given that it uses a BGA pads configuration, making evaluation challenging without a specifically designed PCB [59]. The full sensor is shown in figure 2.8, along with its BGA pad, and the evaluation board is depicted in figure 2.9.

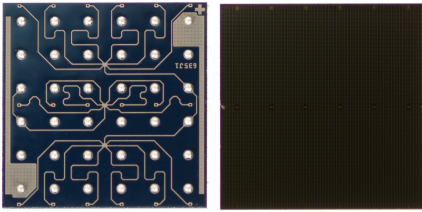


Figure 2.8: Picture of the SiPM MicroFJ 60035 taken from [61] p.10

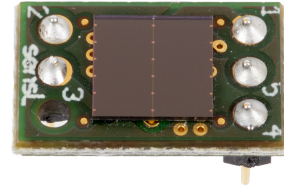


Figure 2.9: Picture of the evaluation board for the SiPM MicroFJ 60035 taken from [61] p.6

Sensor evaluation

As the SiPM sensor is selected, and in order to implement correctly the next amplification stage, the output current, I_{SiPM} , from the SiPM sensor as a function of incoming light and thus function of the distance between the emitter and receiver, needs to be calculated. This

calculation will use the relation provided in equation (2.2), with parameters specified in the MicroFJ SiPM datasheet [61] at the desired optical frequency of $\lambda = 450 \text{ nm}$.

To begin, the incoming light power on the SiPM sensor, $P_{SiPM}(\lambda, d, \Phi_b)$, is computed using the previously calculated irradiance:

$$P_{SiPM}(\lambda, d, \Phi_b) = I_r(\lambda, d, \Phi_b) A_{SiPM} \quad (2.6)$$

Where $A_{SiPM} = 3.684 \times 10^{-5} : \text{m}^2$, the sensor surface area, as provided by the SiPM datasheet [61]. The light power received by the sensor, as a function of the receiver-emitter distance, is detailed in figure 2.10.

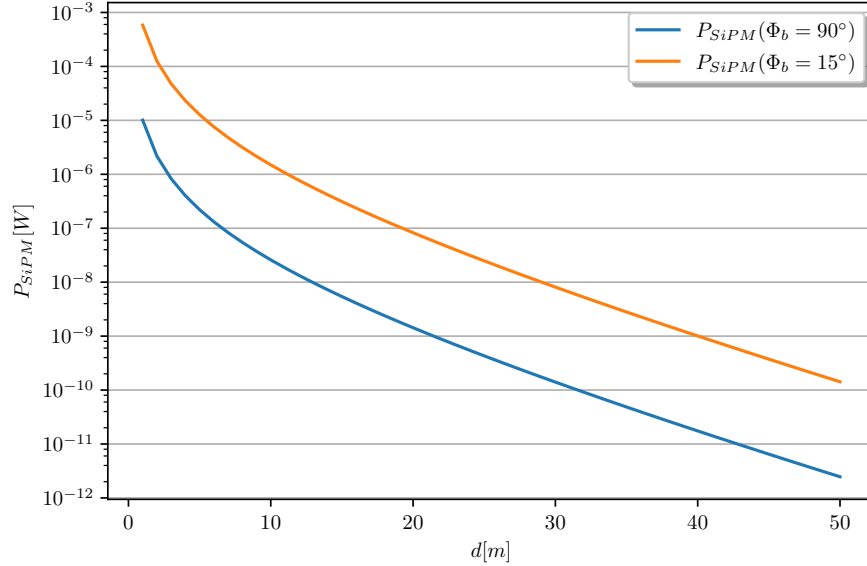


Figure 2.10: Incoming light power $P_{SiPM}[\frac{\text{W}}{\text{m}^2}]$ on the active surface of the SiPM sensor as a function of distance, d , for different beam angles.

However, before calculating the SiPM current, practical considerations must be addressed regarding the maximum continuous output current, $I_{max} = 15 \text{ mA}$, allowed by the sensor. If the sensor is exposed to high-power LED light when the receiver is close to the emitter, the current might exceed this limit and damage the sensor. To mitigate this risk, the average current is first calculated under worst-case scenario conditions, where the sensor receives the full emitter light power, $P_{emitter} = 1 \text{ W} = P_{SiPM}$, using equation (2.2). This results in a maximum flowing current of $I_{SiPM-max} = 43.3 \text{ mA}$. Then, the average current is calculated, considering the 8-DPIM modulation scheme, under a worst-case scenario of continuous pulses interspersed with guard slots:

$$\hat{I}_{SiPM-max} = \frac{I_{SiPM-max}}{2} = 21.65 \text{ mA} \quad (2.7)$$

This calculation shows that the average current flowing through the SiPM could be too high, potentially damaging the sensor. To resolve this issue, a resistor is added at the output

of the SiPM sensor. It modifies the sensor's time constant, as described in equation (2.1). The equation (2.2) stipulates that this resistor can reduce the maximum current of the sensor. The resistor value should be large enough to limit the current but small enough to avoid introducing a significant low-pass filter effect when combined with the SiPM capacitance [62]. Taking this into account, a resistor's value of $R_s = 5 \Omega$ is selected. It leads to a new time constant of $\tau_{R_s} = 6.37 \text{ ns}$ and a reduced maximum current of $I_{SiPM-max} = 29.3 \text{ mA}$, and results in an average current of:

$$\hat{I}_{SiPM-max} = \frac{I_{SiPM-max}}{2} = 14.65 \text{ mA} \quad (2.8)$$

This configuration also maintains a sufficiently high cutoff frequency relative to the modulated pulse duration [62]:

$$f_c = \frac{1}{2\pi R_s C_{SiPM}} = 7.69 \text{ MHz} \quad (2.9)$$

With the new time constant and a safe maximum average current, the output current, $I_{SiPM}(d, \Phi_b)$, of the sensor can now be calculated across the operational range of the UWOCs, and for the two different light beam angles.

The results are described in figure 2.11, with the extreme output current values summarized in table 2.1. The figure 2.11 also illustrates how the SiPM saturates when the incoming light becomes excessive, consistent with the exponential nature of equation (2.2).

SiPM current	$\Phi_b = 90^\circ$	$\Phi_b = 15^\circ$
$I_{SiPM}(d = 1 \text{ m}) [\text{A}]$	$2.92 \cdot 10^{-02}$	$2.92 \cdot 10^{-02}$
$I_{SiPM}(d = 50 \text{ m}) [\text{A}]$	$3.23 \cdot 10^{-07}$	$1.86 \cdot 10^{-05}$

Table 2.1: Maximum and minimum current output of the SiPM sensor function of the emitter-receiver distance and beam angle.

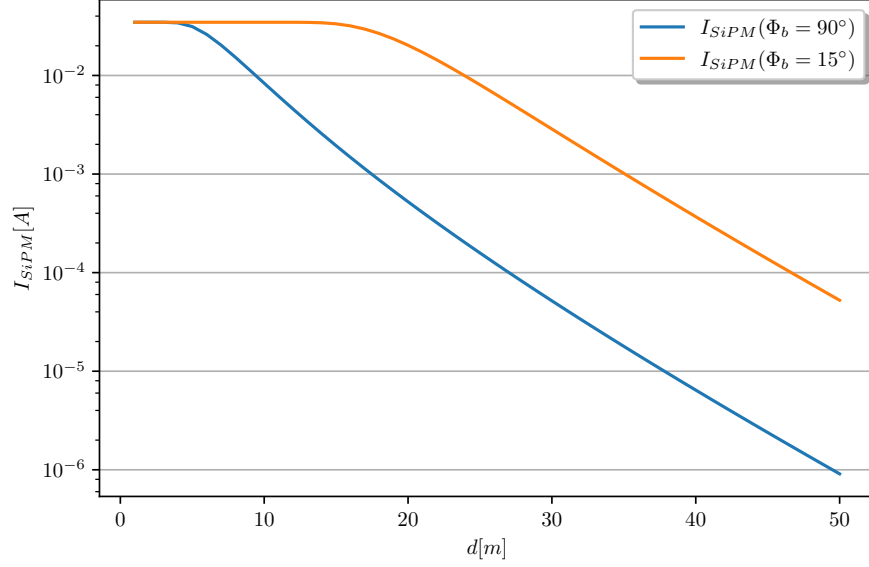


Figure 2.11: Output current $I_{SiPM}(d)$ [A] from the SiPM sensor as a function of the distance, d , for different beam angles with a luminous power $P_l = 1$ W.

Although the sensor's saturation caused by emitted light is not an issue, ambient DC noise due to sunlight must be considered. If the solar power is too high, the photons from the useful light signal will no longer trigger the SiPM microcells effectively, and the sensor's responsivity $R[\frac{A}{W}]$, i.e., the variation in current with respect to incoming light power, will dramatically decrease [56][58].

To evaluate the impact of sunlight, the output current of the SiPM sensor, I_{SiPM} , is calculated as a function of different incoming power levels using equation (2.2), establishing a maximum safe sunlight power under which the sensor will correctly detect the useful light signal without saturating. The results are shown in figure 2.12.

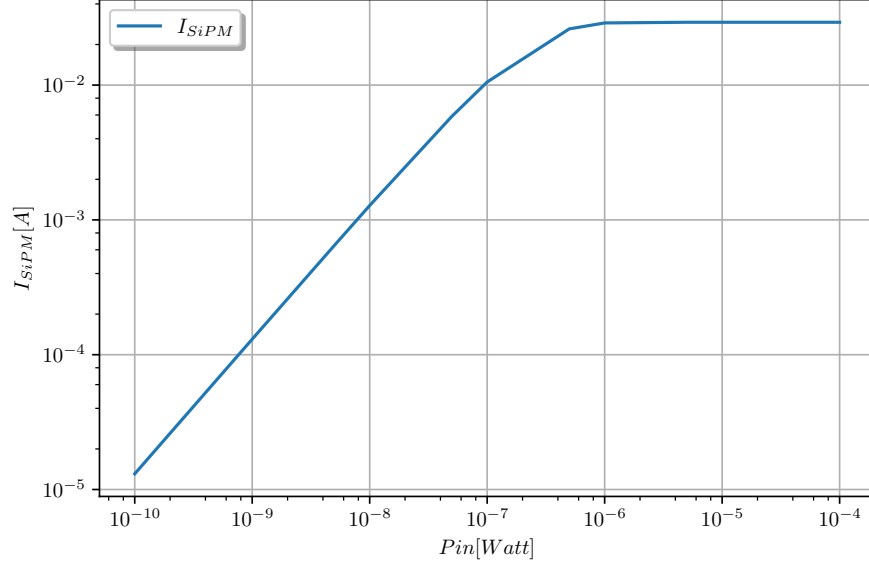


Figure 2.12: Output current I_{SiPM} [A] from the SiPM sensor as a function of the incoming power, P_{in} .

To maintain the sensor in a mostly linear operating range, the solar power arriving on the active surface of the SiPM sensor should remain below approximately $P_{sun}^{max} \lesssim 100$ nW. Based on this upper limit, the solar power, P_{sun} , reaching the sensor is estimated. Using the solar irradiance at the surface³, $I_{sun} \approx 500$ W/m², and applying it to equation (2.6), results in a total power of approximately $P_{sun} \approx 18$ mW reaching the sensor's active surface. This significantly exceeds the linear range limit. Additionally, it is important to note that the irradiance value used only accounts for the visible spectrum, potentially underestimating the problem.

A first solution to mitigate this issue is to limit the electromagnetic spectrum to the LED wavelengths using an optical bandpass filter [13]. This bandpass filter has a spectral range of $\lambda = 50$ nm centered around the peak wavelength $P_{LED}^{max}(\lambda_{max})$ of the LED spectrum. It is designed to cover the typical spectral width of LED emitters, including a safety margin for temperature-induced spectral shifts [38].

Operating the new spectral band λ_{bp} and the solar irradiance per unit of wavelength, $I_{sun-\lambda} \approx 1.74 [\frac{W}{m^2 nm}]$ ⁴, the total solar irradiance within the bandpass range is:

$$I_{sun} = \lambda_{bp} I_{sun-\lambda} = 87 \frac{W}{m^2} \quad (2.10)$$

Based on the solar irradiance comprised in the filter range, the sun power reaching the sensor is now reduced to $P_{sun} \approx 3.2$ mW. If the reduction is significant, it nevertheless largely exceeds the linear range of the sensor. Some other solutions exist, including firstly the use two

³Provided in section 1.1

⁴Provided in section 1.1

polarizers crossed by 90° or secondly the limitation of the UWOCs operational capabilities from a minimal depth as the solar irradiance decrease while the distance from the surface increase⁵[63].

As the UWOCs is designed to operate in clear ocean water, typically far from the coast, and considering that the average ocean depth is approximately 3,682m, the second solution is chosen, setting a minimal operational depth for the UWOCs to function correctly [1]. The minimal functional depth is calculated using Beer-Lambert's Law as defined in equation (2.3), with the solar power at the surface within the filter band, $P_{\text{sun}}^{\text{surf}} \approx 3.2 \text{ mW}$, as the initial power. The minimum depth is calculated to be approximately $d_{\text{min}} \approx 70 \text{ m}$, reducing the solar power to:

$$P_{\text{sun}}^{70} \approx 82 \text{ nW} < P_{\text{sun}}^{\text{max}} = 100 \text{ nW} \quad (2.11)$$

This depth ensures that the ambient light noise remains within acceptable levels, allowing the SiPM sensor to function effectively without saturation.

2.1.2 Amplification stage

With the SiPM signal range established at $I_{\text{SiPM}} \in [19 \mu\text{A}; 29 \text{ mA}]$, the amplification stage can now be developed. As explained in section 1.2, optical sensors typically use an Operational Amplifier (Op-Amp) in a Transimpedance Amplifier (TIA) configuration to convert the sensor's current signal into a readable voltage signal. However, in this context, it is also possible to use a voltage-to-voltage Op-Amp configuration, taking the voltage signal between the output of the SiPM sensor and the series resistor⁶ as shown in figure 2.13. This configuration provides a gain G_{Rs} , defined as follows [38][52]:

$$G_{Rs} = I_{\text{SiPM}} R_s \quad (2.12)$$

With I_{SiPM} the sensor current and R_s the value of the series resistor.

⁵explained in section 1.1

⁶Used to limit the current, as previously explained

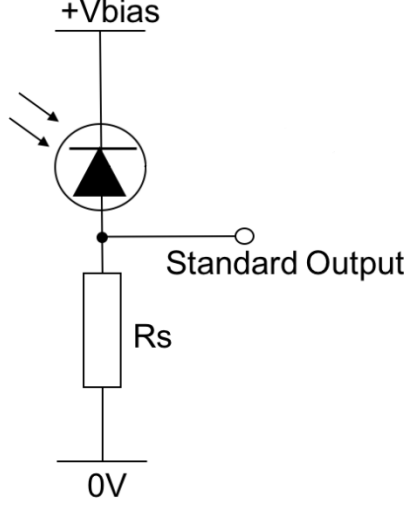


Figure 2.13: The SiPM sensor in serie with a resistor R_s . Adapted from [52] p.8

The voltage-to-voltage configuration is preferred for the developed system for several reasons. Firstly, while the gain offered by a TIA would be slightly higher than the one given by the series resistor - the significant capacitance of the SiPM sensor, $C_{SiPM} = 4140\text{pF}$, would severely limit the TIA's closed-loop bandwidth, f_{3dB} , as calculated below [49][61]:

$$f_{3dB} = \sqrt{\frac{GBP}{2\pi R_F C_{in}}} \quad (2.13)$$

With GBP , the gain bandwidth product of the TIA, R_F , the feedback resistor of the TIA and C_{in} , all parasitic capacitance at the input of the TIA, including the SiPM capacitance C_{SiPM} .

At the time of writing this thesis, Transimpedance Amplifiers (TIAs) available on the market typically have a Gain Bandwidth Product (GBP) in the GHz range. An example is provided through the calculation of the closed-loop bandwidth, f_{3dB} , for the OPA818, a TIA from Texas Instruments with a GBP of 2.7 GHz[64][51]. According to the Op-amp datasheet, the other parasitic capacitances are negligible compared to that of the SiPM, allowing to approximate the input capacitance with $C_{in} \approx C_{SiPM} = 4140\text{pF}$. Given this input parasitic capacitance and the desired bandwidth, a feedback resistor value of $R_s = 20\Omega$ appears to be appropriate, giving a gain of $G = 20$ and a TIA bandwidth of $f_{3dB-TIA} = 7.2\text{MHz}$. If the gain is close to that of the series resistor, this configuration might introduces additional noise directly from the TIA [65].

The second reason for preferring the voltage-to-voltage configuration is the current limitation at the TIA ports. While photodiodes typically generate very small current signals, the SiPM used in the designed UWOCs may produce an average current of $\hat{I}_{SiPM-max} \approx 15\text{mA}$ [65]. This current would flow through the feedback pin of the TIA, potentially exceeding the maximum allowable current, as would be the case with the OPA818.

Amplification stage design

Given the choice to use a voltage-to-voltage configuration, the Op-Amp is selected. The objective is to amplify a wide range of voltage signals, $V_{in} \in [95 \mu\text{V}; 145 \text{mV}]$, calculated using equation (2.12). The selected Op-Amp should count among other things the following characteristics [55][66][67]:

- High GBP: to provide sufficient gain without requiring too many amplification stages;
- Low voltage and current noise: to maintain a good signal-to-noise ratio, especially when the input signal is low;
- Low bias current: to minimize voltage offset.

On that basis, the OPA818 from Texas Instruments is chosen and described in figure 2.14. As previously mentioned, with a GBP of 2.7 GHz, it is placed in the highest GBP Op-Amps, while also offering low input voltage and current noise, with $e_n = 2.2 \frac{\text{nV}}{\sqrt{\text{Hz}}}$ and $i_n = 145 \frac{\text{fA}}{\sqrt{\text{Hz}}}$, respectively, and a bias current of $i_B = \pm 4 \text{pA}$.

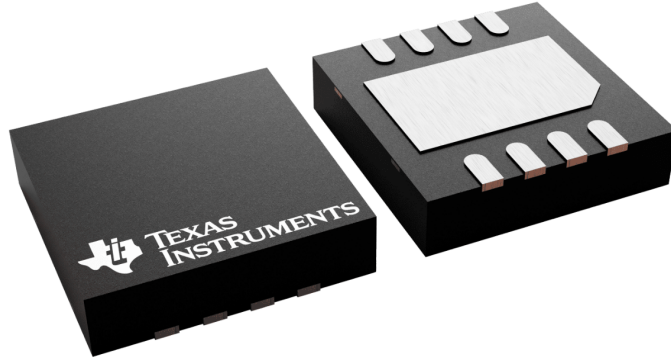


Figure 2.14: The OPA818 from Texas Instruments and its WSON package. Taken from [68]

Taking into account the large capacitance of the SiPM sensor, the Op-Amp will be configured in an inverting configuration. This provides better stability when dealing with input capacitance due to proper compensation[69][66]. Furthermore, in the non-inverting configuration, the OPA818 would require the parallel combination of gain resistors to remain below 50Ω to prevent stability issues. However, this value is close to the series resistor $R_S = 5 \Omega$, which could allow excessive current to flow through the feedback branch [51].

As the configuration is set, the gain of each Op-Amp has to be determined. The Op-Amp will operate in a large signal mode, as the output voltage must be sufficiently high to be read after the amplification stages. Moreover, with a wide input range, the Op-Amp output will saturate when the input signal reaches a certain threshold and will also produce large signal swing in this case [51][66]. This is important as when large signals are involved, the OPA818's GBP is reduced to $GBP_L = 400 \text{MHz}$, and the maximum bandwidth, as a function of the gain G , is calculated as follows [66]:

$$B_L = \frac{GBP_L}{G} \quad (2.14)$$

Applying equation (2.14) with an absolute gain of $G = 20$ provide a usable bandwidth of $B_L = 20$ MHz. This bandwidth exceeds the one required in the specification section. However, it provides a safety margin against potential variations up to 60% of the GBP due to design and temperature fluctuations. It also ensures that the harmonics of the 8-DPIM pulse remains within the signal bandwidth [66]. To achieve such gain, two resistors, R_G and R_F , are added as shown in figure 2.15, and the gain is calculated as follows [70]:

$$G = \frac{V_{out}}{V_{in}} = -\frac{R_F}{R_G} = -20 \quad (2.15)$$

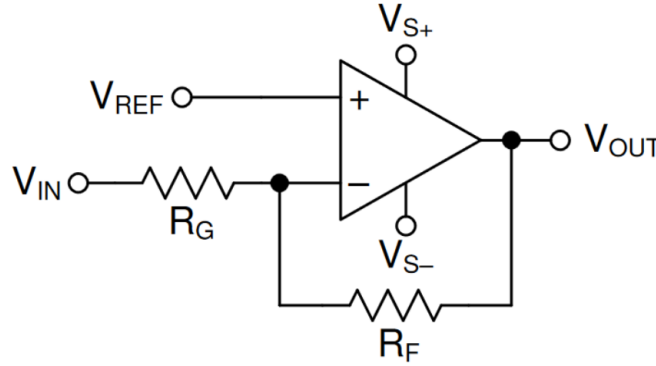


Figure 2.15: The OPA818 used in inverting configuration with R_G and R_F . Taken from [51] p.15

With V_{out} as the output voltage of the amplifier, V_{in} as the input voltage previously defined and the negative gain indicating the inverting configuration of the Op-Amp. The values of R_G and R_F must be carefully selected to minimize thermal noise, which increases with resistor value [66][71]. However, choosing resistors that are too low would interfere with the series resistance and inject excessive current into the feedback branch. Therefore, R_G and R_F are set to $100\ \Omega$ and $2\ \text{k}\Omega$, respectively. These values ensure that only a small percentage of current flows through the feedback branch, remaining within the Op-Amp's limitations as specified in the datasheet [51].

Finally, since the OPA818 is decompensated, i.e. having no internal compensation elements in order to reach high GBP, a compensation capacitor, C_F , is placed in parallel to the feedback resistance to ensure a better stability for the Op-Amp [72][51]. It will act as a low-pass filter, and its value is calculated as follows [72]:

$$C_F = \frac{1}{2\pi R_F B_L} \approx 5\ \text{pF} \quad (2.16)$$

With $B_L = 20$ MHz, the large signal bandwidth of the Op-Amp at a gain of $|G| = 20$. Once the first stage is defined, additional Op-Amp stages might be added to achieve a

sufficient overall gain, especially when the input signal is at its lowest with $V_{in}^{min} = 95 \mu\text{V}$. The final required output variation between low (no pulse) and high (pulse) states is set at $V_{out}^{L \rightarrow H} = 2 \text{ V}$. It seems suitable for reading or sending the signal to the comparator stage and dealing with the Op-Amp's peak noise voltage, as discussed below. Given the desired output variation, the minimum required gain is:

$$G_{min} = \frac{V_{out}^{L \rightarrow H}}{V_{in}^{min}} \approx 21000 \quad (2.17)$$

Assuming each Op-Amp operates at the maximum allowed gain of $G = 20$, the number of required stage is comprised between three and four. To achieve the desired gain with only three stages, resulting in $G_{tot} = -8000$, and to avoid an additional stage, the emitter power implemented in the next chapter will be increased from $P_{emitter} = 1 \text{ W}$ to $P_{emitter} = 3 \text{ W}$.

With this new light power, the minimum current flowing through the SiPM, I_{SiPM}^{min} , when the receiver is at 50 m, is recomputed. As a result, the SiPM sensor will output at minimum a current of $I_{SiPM}^{min} \approx 51 \mu\text{A}$ using the narrow beam setup. The output current $I_{SiPM}(d)[\text{A}]$ from the SiPM sensor as a function of the distance is shown in figure 2.16.

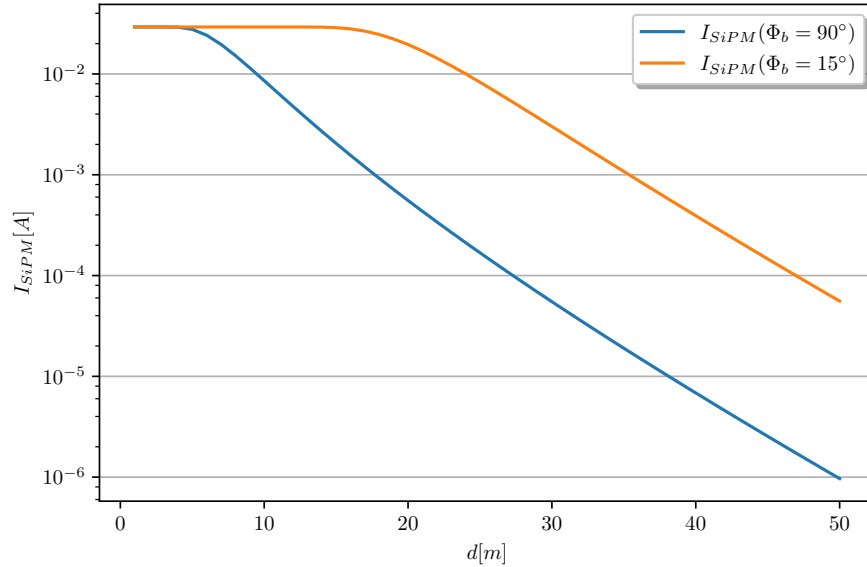


Figure 2.16: Output current $I_{SiPM}(d)[\text{A}]$ from the SiPM sensor as a function of the distance, d , for different beam angles with a luminous power $P_l = 3 \text{ W}$.

With this new configuration, and employing equation (2.12) combined with I_{SiPM}^{min} , the minimum input voltage at the first amplification stage is calculated as :

$$V_{in}^{min} = I_{SiPM}^{min} R_s = 255 \mu\text{V} \quad (2.18)$$

After three amplification stages, the minimum output swing will be $V_{out}^{min} = |2.04| \text{ V}$ - an acceptable level. The output voltage swing is in absolute value as, after three stages, the

global gain is negative.

To power the various Op-Amps, a separate DC supply board has been implemented providing a positive supply voltage of $V_{S+} = 5\text{ V}$ and a negative supply voltage of $V_{S-} = -5\text{ V}$ [51]. The non-inverting input of the different Op-amp's will be grounded to avoid DC offset when the input signal is null [55]. Given the ultra-low bias current of the OPA818, no canceling resistor is needed between the non-inverting input and ground[73][51]. The final Op-amp stage schematic is shown in figure 2.14

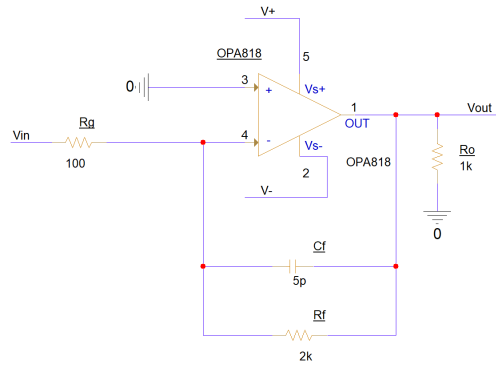


Figure 2.17: Schematic of the implemented amplification stage using OPA818 from Texas Instruments.

Finally to mitigate residual solar light DC noise and the DC offset voltage from the OPA818, high-pass filters are implemented after the first and second amplification stages[71]. Each filter is composed of a resistor and a capacitor, as shown in figure 2.18. The high-pass cutoff frequency, f_{3dB} , is set using :

$$f_{3dB} = \frac{1}{2\pi R_{hp} C_{hp}} = \frac{1}{2\pi 500\Omega 500\text{ nF}} = 637\text{ Hz} \quad (2.19)$$

With respectively R_{hp} and C_{hp} the resistor and the capacitor of the high pass filter.

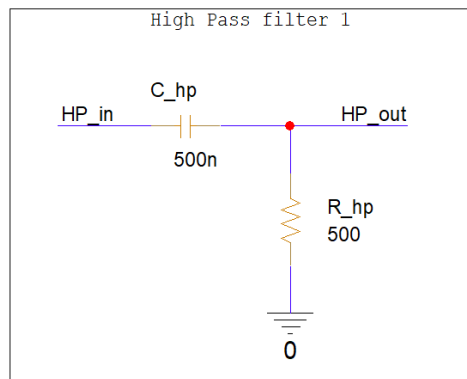


Figure 2.18: Schematic of the implemented high pass filter using resistor and capacitor.

With the different amplification stages defined, the overall noise generated by the amplification stages is evaluated. For this different noise sources are considered [66][71][51]:

- Op-Amp Noise:
 - The voltage pink noise: $e_{1/f}$
 - The voltage white noise: e_n
 - The current noise: i_n
- Resistor Noise:
 - The thermal or Johnson noise: e_{Rn}

As high-pass filters are implemented, the pink noise can be ignored as it is inversely proportional to the frequency. The current's noise is also negligible due to the OPA818's ultra-low input current noise and the low values of R_G and R_F . Excluding these noise sources, only the white noise at the Op-Amp input and the thermal noise from the resistors remain. The total Root Mean Square (RMS) Op-Amp white noise is calculated as follows[66][71][51]:

$$B_n = \frac{GBP K_n}{G_{N-I}} \approx 202 \text{ MHz} \quad (2.20)$$

where $G_{N-I} = 21$ is the gain of the Op-Amp in non-inverting configuration, as noise calculations always use the non-inverting gain, $K_n = 1.57$ is the brick wall correction factor, and $GBP = 2.7 \text{ GHz}$ is the small-signal gain bandwidth product of the Op-Amp. Then using the noise bandwidth, the RMS noise from the Op-Amp is calculated as:

$$E_n = e_n \sqrt{B_n} \approx 31.27 \mu\text{V} \quad (2.21)$$

With $e_n = 2.2 \frac{\text{nV}}{\sqrt{\text{Hz}}}$, the Op-amp voltage white noise.

Afterwards, the thermal noise from the gain resistors is calculated using [66][71]:

$$E_{Rn} = \sqrt{4kTR_{n-eq}B_n} \approx 17.78 \mu\text{V} \quad (2.22)$$

With k , the Boltzmann constant, $T = 298\text{K}$ the temperature and $R_{n-eq} = R_G \parallel R_F = 95.24\Omega$.

Having now the different noise source at the Op-amp input, the total RMS noise is calculated as [66][71]:

$$E_{in} = \sqrt{E_n^2 + E_{Rn}^2} \approx 35.97 \mu\text{V} \quad (2.23)$$

And the the total RMS noise at the output of the first Op-Amp using :

$$E_{out-1} = E_{in} G_{N-I} \approx 755.37 \mu\text{V} \quad (2.24)$$

Finally, the total RMS noise at the final amplification stage is given as follow :

$$E_{out} = E_{out-1} G_2 G_3 \approx 302 \text{ mV} \quad (2.25)$$

With $G_2 = 20$ and $G_3 = 20$ the gain of the next two Op-amp.

Since the noise of the subsequent Op-Amps will be similar to the first one, but with lower remaining gain, it is expected to be significantly lower and is thus ignored. While the RMS value provides a mean estimate of the noise present at the output of the amplification stage, noise can occasionally exceed this value, necessitating a higher margin. For this, the peak voltage noise is calculated using three times the standard deviation $\sigma = E_{out}$ as the noise mean $\mu = 0$ and give [71][66]:

$$E_{out-p} = 3 E_{out} \approx 909\text{mV} \quad (2.26)$$

With 0.3% chance to exceed this peak value which is more acceptable.

Comparator stage design

The amplification stages and noise calculations specified, the comparator stage can now be designed. The non-inverting comparator operates as follows: the amplified signal, V_{out}^{Ampl} , is connected to the non-inverting input of the comparator, and a reference voltage, V_{ref} , is connected to the inverting input [74]. The comparator's output will swing between low and high states depending on whether the amplified signal is below or above the reference voltage, as shown in table 2.2. This configuration digitizes the output of the UWOCs receiver circuit into low or high levels without intermediate states. Since the gain is negative, the amplified signal will set the comparator to low when a pulse occurs and to high when not.

Input	Output
$V_{out}^{Ampl} \geq V_{ref}$	$V_{out} = V_H \approx V_{s+}$
$V_{out}^{Ampl} < V_{ref}$	$V_{out} = V_L \approx V_{s-}$

Table 2.2: Input-output relationship for the comparator circuit. Adapted from [74]

To implement the comparator in the UWOCs receiver, the TLV3601 from Texas Instruments is chosen [75]. This comparator is one of the fastest available from Texas Instruments at the time of writing this Master Thesis. It features a propagation delay of only 2.5 ns, which is negligible compared to the pulse duration of the 8-DPIM modulation. It also accepts a wide input signal range within the supply voltages, which are set at $V_{s+}^{comp} = 2.5\text{ V}$ and $V_{s-}^{comp} = -2.5\text{ V}$ [76][75].

As the comparator's supply voltage range is the half of the OPA818, the output signal from the amplification stage must be divided accordingly. A voltage divider is set using two resistors, $R_{c1} = 2\text{ k}\Omega$ and $R_{c2} = 2\text{ k}\Omega$, with the comparator input voltage V_{in}^{Comp} calculated as follows [71]:

$$V_{in}^{Comp} = V_{out}^{Ampl} \frac{R_{c2}}{R_{c1} + R_{c2}} \quad (2.27)$$

Afterwards, the comparator's supply voltage is derived directly from the board supply used for the OPA818 via two low dropout voltage regulators (LDO): the AMD7160 (AUJZ-2.5-R2)

from Analog Devices for the positive supply and the ADP7182 (AUJZ-2.5-R7) for the negative supply [71][77].

Both LDOs are low noise and capable of supplying the TLV3601's maximum output current of $I_{out}^{max} = 50 \text{ mA}$, as each is capable of providing up to 200 mA [78][79][75]. As the LDO voltage drop of $V_{drop} = 2.5 \text{ V}$, combined with the maximum current drawn by the TLV3601, $I_{out}^{max} = 50 \text{ mA}$, will result in thermal dissipation of $P_D^{max} = V_{drop} I_{out}^{max} = 125 \text{ mW}$ this will need to be managed in order to avoid exceeding the maximum operating temperature of $T_{LDO}^{max} = 125^\circ\text{C}$ [71][79][78]. Thus, the LDO temperature increase, T_r , is calculated assuming an initial temperature of $T_{ini} = 25^\circ\text{C}$ and results in:

$$T_r = T_{ini} + P_D \Theta_{JA} = 46.25^\circ\text{C} < T_{LDO}^{max} = 125^\circ\text{C} \quad (2.28)$$

With $\Theta_{JA} = 170 \frac{^\circ\text{C}}{\text{W}}$ the junction to ambient thermal resistance for both the LDO in their TSOT package. As shown in equation (2.28), the LDOs will remain within their operational temperature limits.

Lastly, the reference voltage at the inverting input of the comparator is set using a voltage divider [71]. As the gain is negative, the reference voltage will also be negative, using the negative supply of the comparator, $V_{s-}^{comp} = -2.5 \text{ V}$, at the input of the voltage divider. The reference voltage is set at $V_{ref}^{comp} = 0.5 \text{ V}$, which is slightly above the output noise of the amplification stages (regarding the previous voltage division). The two resistors are set to $R_{cr1} = 8 \text{ k}\Omega$ and $R_{cr2} = 2 \text{ k}\Omega$. The final schematic of the comparator stage is shown in figure 2.19.

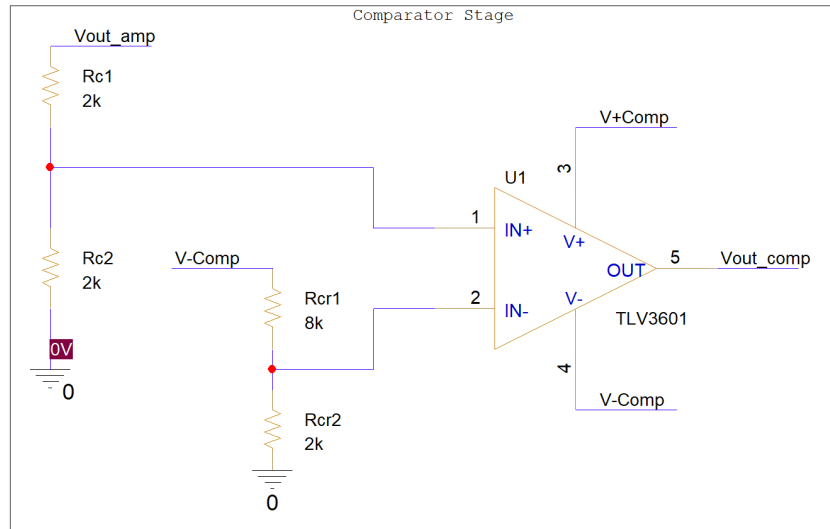


Figure 2.19: Schematic of the implemented comparator stage using TLV3601 comparator.

2.1.3 Emitter board simulation

The designed architecture requires to be simulated in order confirm it performs as expected before implementing the printed circuit board (PCB).

The simulation is conducted using Cadence Spice software, with the OPA818 and TLV3601 Spice models obtained directly from Texas Instruments's website to ensure accurate simulation [80][68][81]. Since there is no Spice model available for the SiPM sensor, it is modeled with two current sources: one representing the useful signal I_{SiPM} and another representing the DC current caused by solar noise I_n . The solar noise is calculated using equation (2.2), with the highest light power $P_{\text{sun}}^{70} \approx 82 \text{ nW}$ at a depth of 70 m, which is the minimum operational depth defined previously. This results in a DC noise current of $I_n = 8.97 \text{ mA}$. Additionally, the SiPM capacitance $C_{SiPM} = 4140 \text{ pF}$ is connected in parallel with the two current sources. The schematic is shown in figure 2.20, with R_1 representing the series resistor.

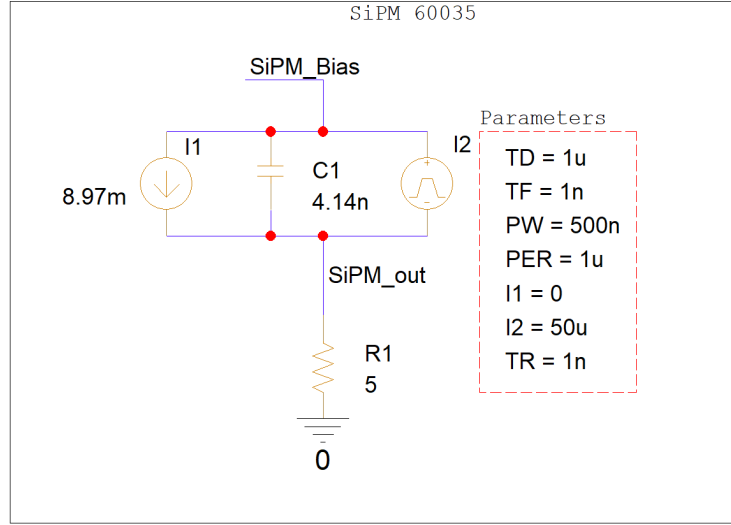


Figure 2.20: Schematic of the modeled SiPM MicroFJ-60035 used for Pspice simulation.

The amplification stages, along with their high-pass filters, are then set up using the OPA818 model, as shown in figure 2.21, figure 2.22 and figure 2.23. A resistor with the value $R_{O4} = 50 \Omega$ is placed at the output of the Op-Amp to control the output impedance to a standard 50Ω , preventing reflections as an output port will be included on the PCB to monitor the output of the amplification stage [71][82]. Additionally, a random white noise source is introduced at the first Op-Amp stage to model resistor noise at the value calculated in the previous section. Inspecting the OPA818 Spice model confirms that it includes the noise of the Op-Amp as expected.

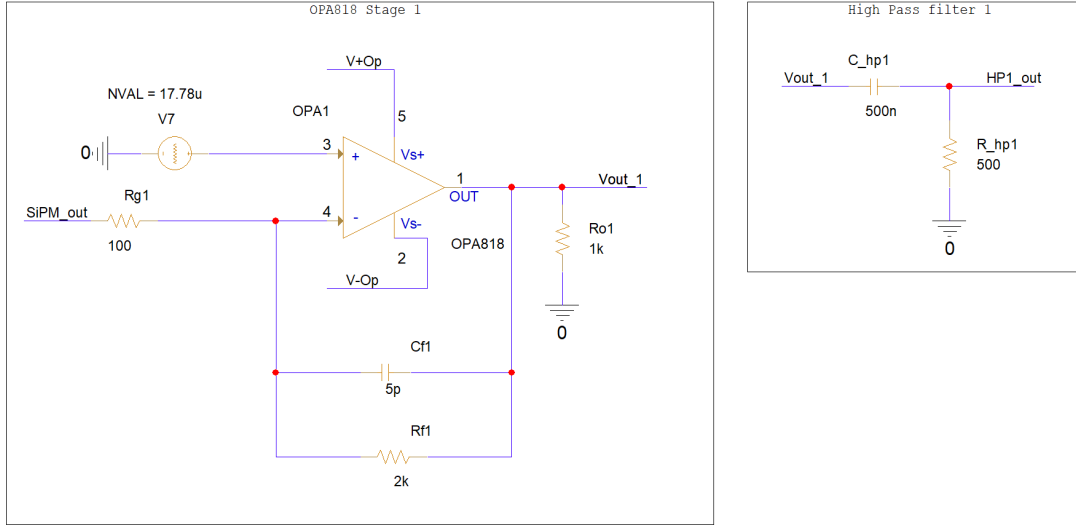


Figure 2.21: Schematic of the first amplification stage with its associated High Pass filter stage.

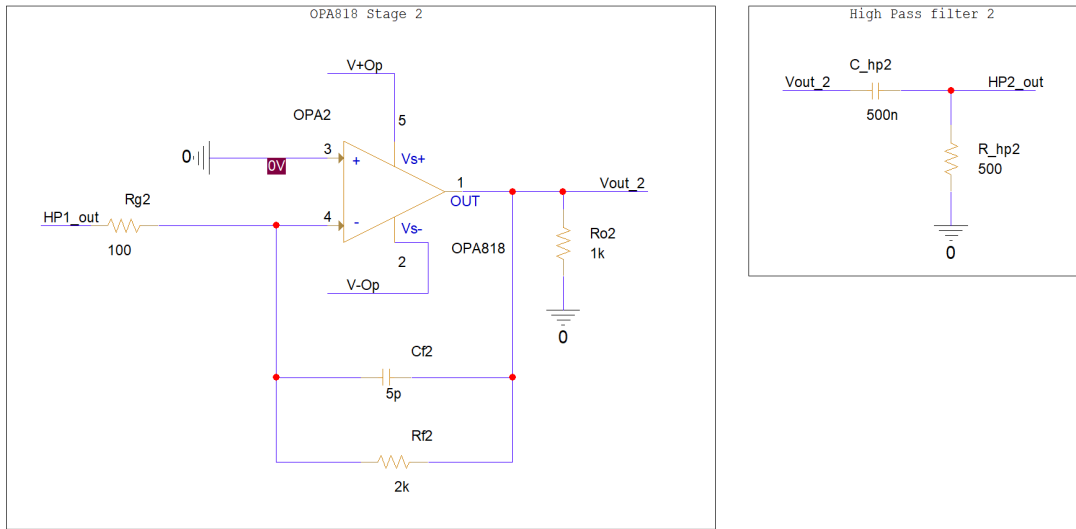


Figure 2.22: Schematic of the second amplification stage with its associated High Pass filter stage.

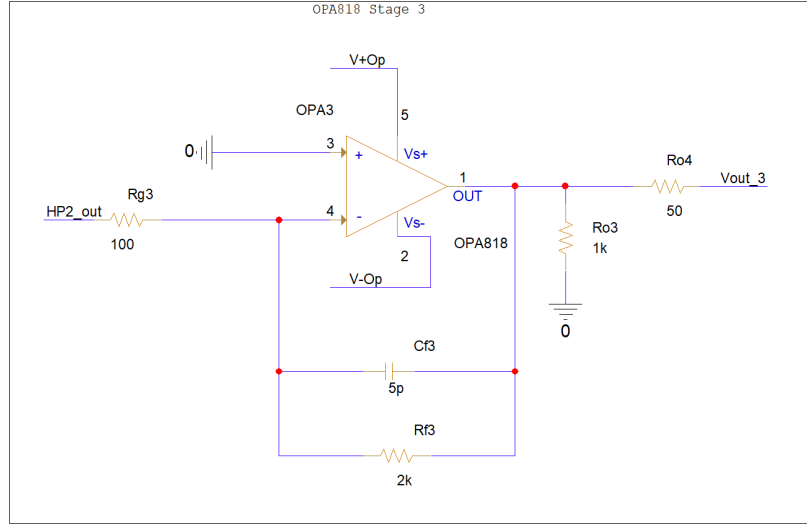


Figure 2.23: Schematic of the last amplification stage with a $50\ \Omega$ output resistance.

The comparator stage is then set up, as shown in figure 2.24. The output of the comparator will be measured using an oscilloscope, and an SMA port will be added when the PCB is built to connect the board to the oscilloscope via an RG58 coaxial cable. The RG58 coaxial cable has a capacitance of $C_{Coax} = \pm 100\ \frac{\text{pF}}{\text{m}}$, forming a low-pass filter with the output resistance of the TLV3601, potentially affecting the output signal [71][75][83]. Therefore, a capacitance $C_{f4} = \pm 100\ \text{pF}$, representing the capacitance of 1 m of RG58 cable, is added at the output of the comparator stage to check for any potential issues.

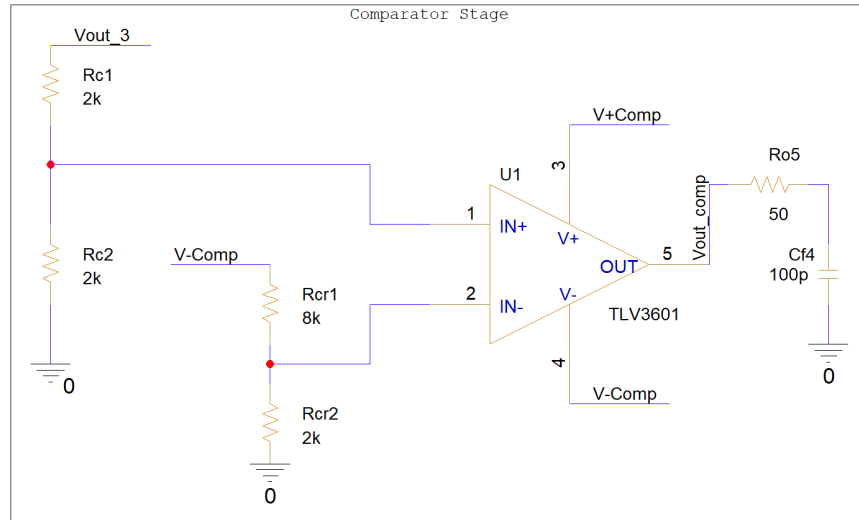


Figure 2.24: Schematic of the comparator with the different voltage divider and the simulated .

Transient simulation

With the circuit modeled, various simulations are performed. The transient simulations check if the circuit work as expected using the minimum and maximum expected current from the SiPM sensor, with the shortest and longest pulse intervals based on the 8-DPIM modulation scheme.

The first simulation is conducted with the minimum expected SiPM output current $I_{SiPM} = 51\mu\text{A}$ and a pulse duration of $T_p = 500\text{ns}$, followed by a no-pulse period of $T_l = 500\text{ns}$, representing the first symbol from the 8-DPIM modulation scheme. The simulation is set to transient with a running time of $3\mu\text{s}$ to show multiple pulses. Through trial and error, the maximum step size of the simulation is set to 1ns to achieve maximum resolution given the tight rise time of the Op-Amp and comparator [51][80]. The results of the simulation are shown in figure 2.25, figure 2.26 and figure 2.27.

In figure 2.25, the utility of the comparator stage is obvious. With the minimum SiPM output current, the third amplification stage does not saturate, and the output does not reach a perfect high state, while the comparator successfully reaches its high state as its input signal is below the reference voltage. The delay between the pulsed current signal and the comparator output is minimal. The high-state output voltage at the third amplification stage is slightly below the expected $V_{out-3} = |2.04|\text{V}$, but it is still sufficient to correctly threshold the comparator.

Then, the output voltage of the first amplification stage and the high pass filter is inspected using figure 2.26 and figure 2.27. As expected, the DC noise from sunlight is present at the Op-Amp output and is subsequently removed by the high-pass filter.

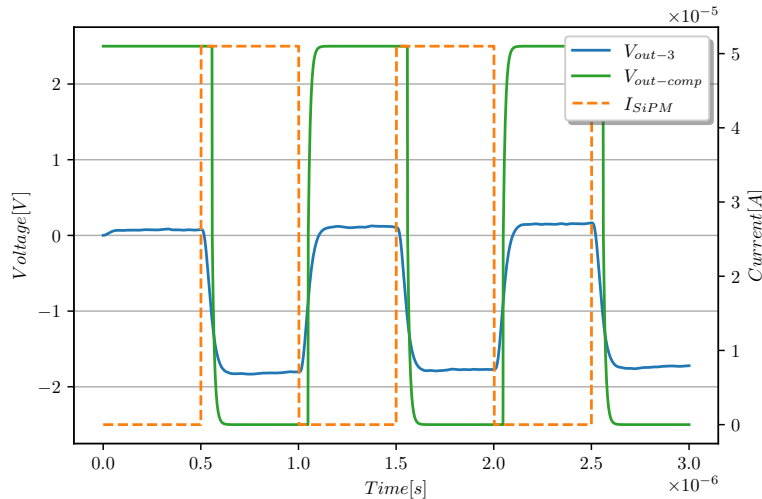


Figure 2.25: Transient simulation of the receiver board showing both output voltage of the last amplification stage and comparator and the SiPM output current. This simulation uses the shortest pulse interval and the SiPM minimum output current.

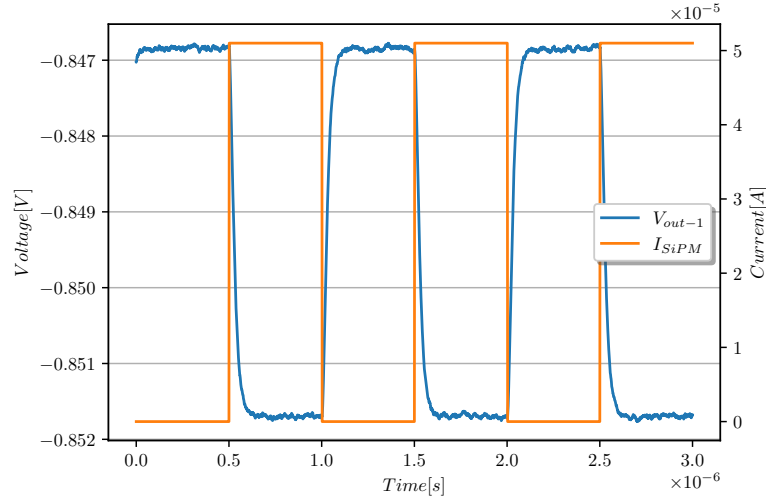


Figure 2.26: Transient simulation of the receiver board showing the output voltage of the first amplification stage and the SiPM output current. This simulation uses the shortest pulse interval and the SiPM minimum output current.

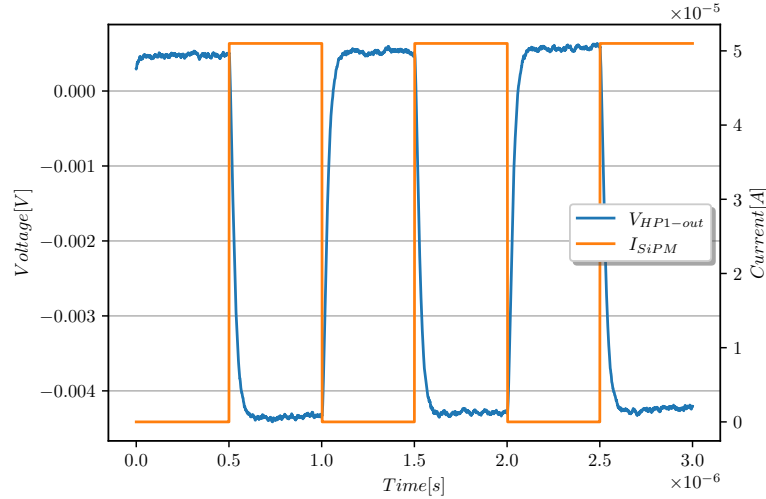


Figure 2.27: Transient simulation of the receiver board showing the output voltage of the first high pass filter and the SiPM output current. This simulation uses the shortest pulse interval and the SiPM minimum output current.

The second simulation is performed using the same parameters except the output current of the SiPM which is set now to its highest value. The results are shown on figure 2.28, figure 2.29 and figure 2.30.

The figure 2.28 shows the output of the third amplification stage saturating at its maximum swing output, regarding the OPA818 datasheet [68]. Like before, the comparator provides a reliable digital high and low level, but it is interesting to note a slight delay in

the High-to-Low transition. This can be explained using the figure 2.29, which shows the output voltage of the SiPM sensor in series with R_s . The series resistor, while limiting the SiPM sensor current, also forms a low-pass filter with the SiPM's internal capacitance. It causes the pulses to be less square, which impacts the entire amplification chain. When the SiPM current is at its maximum, the Op-Amps saturate, and the SiPM voltage must decrease sufficiently so that the last amplification stage could decrease. However, since 8-DPIM uses intervals between pulses⁷, this situation does not affect system performance.

Finally, as the SiPM output current is at its maximum in this simulation, an analysis of the current entering the first Op-Amp and the maximum power dissipated by both the first Op-Amp and the comparator is performed. The first Op-Amp is chosen as it is the closest to the SiPM sensor and is most likely to be affected. The figure 2.30 shows the current flowing through the feedback and output pins of the first OPA818 and the power dissipated by both the first Op-Amp and the comparator. For the Op-Amp, the maximum currents are within safe limits according to the OPA818 datasheet, and the average power dissipated is $\hat{P}_{OPA-1} \approx 150 \text{ mW}$, well below the limit, considering the junction-to-ambient thermal resistance $\Theta_{JA} = 54.6 \frac{^\circ\text{C}}{\text{W}}$ of the OPA818, as discussed in the LDO design [71][51]. The comparator, despite having a higher junction-to-ambient thermal resistance of $\Theta_{JA} = 176.5 \frac{^\circ\text{C}}{\text{W}}$, dissipates an average power below 50 mW, so the thermal situation is also within acceptable limits.

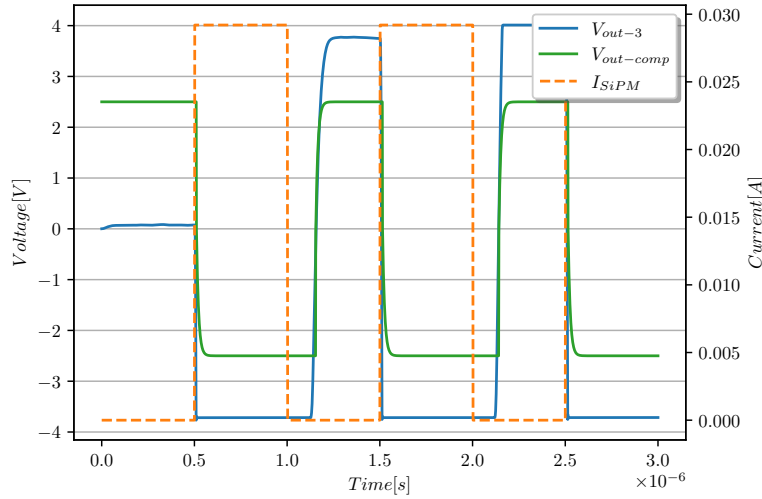


Figure 2.28: Transient simulation of the receiver board showing both output voltage of the last amplification stage and comparator and the SiPM output current. This simulation uses the shortest pulse interval and the SiPM maximum output current

⁷Explained in section 1.2

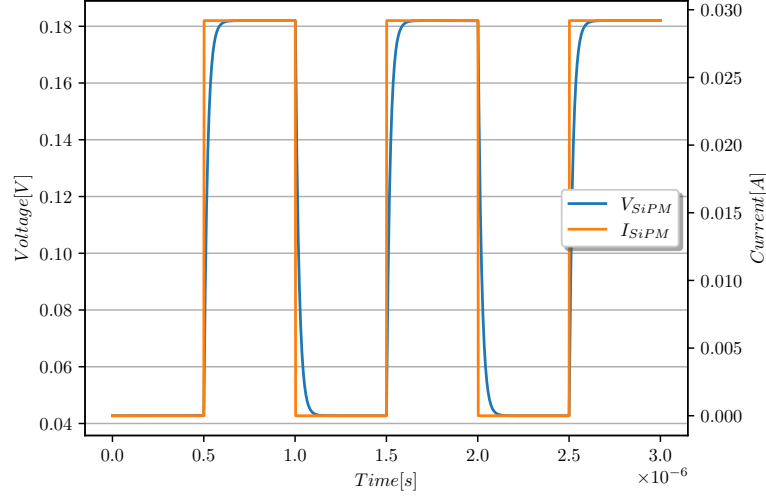


Figure 2.29: Transient simulation of the receiver board showing the output voltage of the SiPM sensor and the SiPM output current. This simulation uses the shortest pulse interval and the SiPM maximum output current

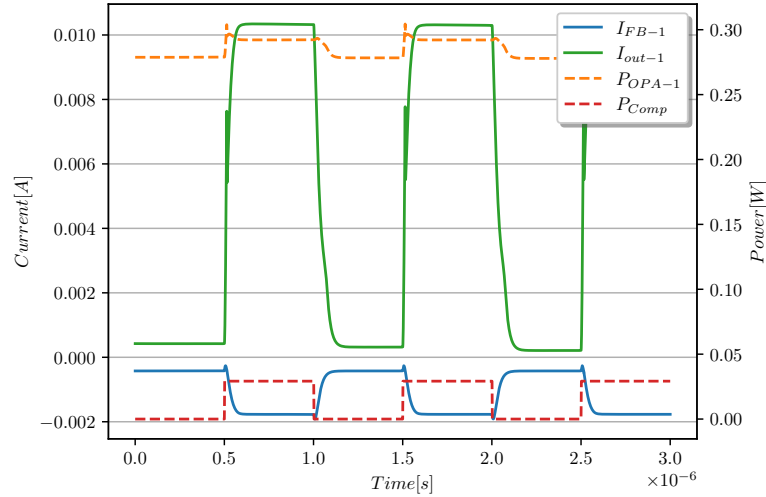


Figure 2.30: Transient simulation of the receiver board showing the current through the feedback and output pin of the first Op-amp and the output power of the first Op-Amp and comparator. This when the SiPM maximum output current occurs.

After these results, a final transient simulation is performed, now taking the longest period between pulses and the lowest SiPM output current to check stability during longer pulses. The results are shown in figure 2.31. As with the previous simulations, the circuit performs as required with the expected output swing at both the last amplification stage and the comparator stage.

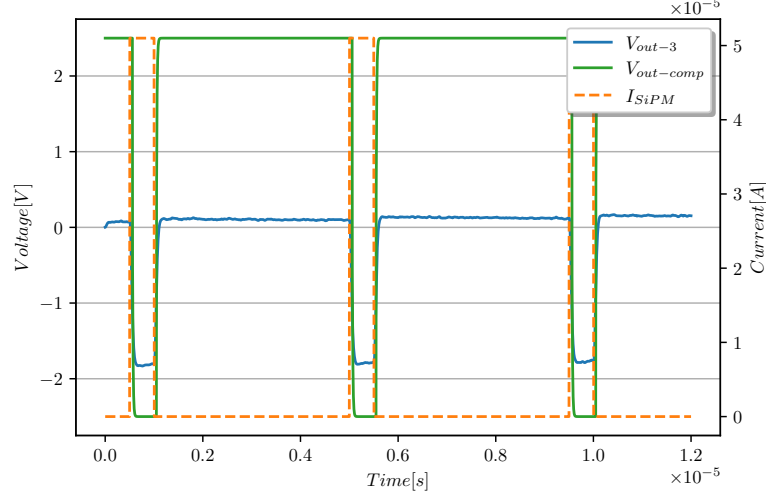


Figure 2.31: Transient simulation of the receiver board illustrating both output voltage of the last amplification stage and comparator and the SiPM output current. This simulation uses the longest pulse interval and the SiPM minimum output current.

AC simulation

Two AC simulations are then performed to verify the bandwidth and phase of the amplification stages. The first AC simulation, conducted using the lowest SiPM current, is illustrated in figure 2.32. As expected, the gain within the desired bandwidth is just below $G = |8000|$. The lowest frequencies are attenuated by the two high-pass filters, and the highest frequencies are limited by the bandwidth of the Op-Amp and the low-pass filter formed by the SiPM capacitance and the series resistor. Additionally, the phase shift within the desired bandwidth is approximately $\Delta\phi \approx -180^\circ$, indicating the expected negative gain induced by the inverting configuration of the three Op-Amps. A similar AC simulation was conducted using the highest SiPM output current, and the results are similar to the first simulation.

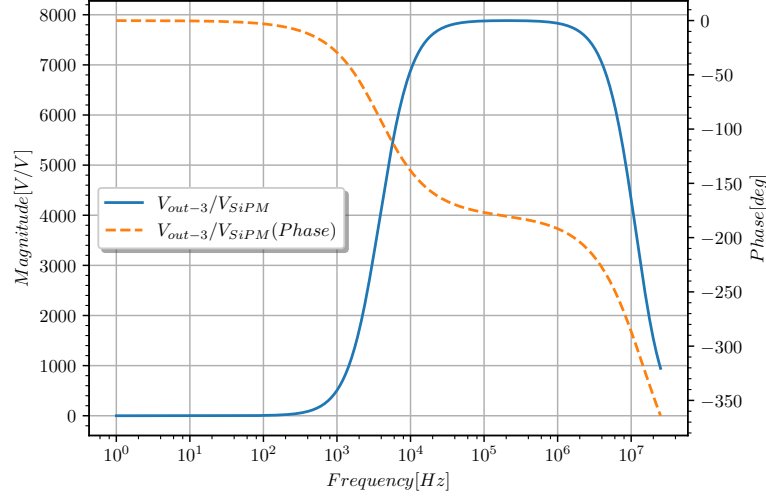


Figure 2.32: AC simulation of the receiver board showing the gain between the last amplification stage output and the SiPM output voltage, using the lowest SiPM output current.

2.1.4 Printed Circuit Board (PCB) design

Following the positive results of the simulations, the PCB is designed using Altium Designer, both for the final schematics and the PCB board design.

PCB schematics

The first step in designing the PCB is to select the various components and ensure their availability from suppliers. These components are then placed on the PCB schematic, including all auxiliary components such as decoupling capacitors, input and output ports, and others not previously considered. Special attention is given to ensuring that the component schematics and footprints are available from Ultra Librarian or Samacys, which simplifies the design process and avoids the need to create component footprints from scratch [84][85]. These requirements being highlighted, the different schematics sections can thus be defined.

The first section focuses on all input and output ports of the PCB. The components needed include:

- A 4-input power connector for the different power supplies and ground connection.
- A 3-pin PCB header to enable or disable the Op-Amps.
- A 3-pin PCB header to route the amplification stage signal either to the comparator or directly out of the PCB for measurement purposes.
- An SMA coaxial connector at the output of the amplification stage

- A test pad at the output of the amplification stage
- An SMA coaxial connector at the output of the comparator

For readability, if not mentioned here, the list of the chosen components is shown in the Bill of Materials (BOM) provided in figure A.1 in Appendix A. Special attention is given to the selection of the SMA connector to ensure it has a characteristic impedance of 50Ω to avoid reflections [71]. The selected SMA connector from Samtec is shown in figure 2.33. Similarly, the test pad size is chosen to be as small as possible to minimize parasitic issues. The selected test pad from Keystone is available in figure 2.34.



Figure 2.33: Picture of the selected SMA connector from Samtec. Taken from [86]

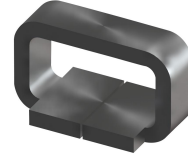


Figure 2.34: Schematic of the 5019 test pad from Keystone. Taken from [87]

Regarding the supply side, ferrite beads are placed immediately after the $\pm 5\text{ V}$ inputs to filter high-frequency signals and avoid perturbation on the Op-Amp or comparator side [88][89]. Additionally, six decoupling capacitors with high capacitance of $C_d = 2.2\text{ }\mu\text{F}$ are placed in accordance with OPA818 and TLV3601 requirements [51][75]. The same is applied for the SiPM bias voltage inputs [90]. Due to their large capacitance, these capacitors filter lower frequencies and require a lower reaction time [51][71]. Therefore, they are placed immediately after the input supply ports, and a larger 1206 SMD package size is selected. The maximum voltage of the capacitors is 50 V , corresponding to the bias voltage of the SiPM sensor.

The different components are then placed, and the output and selection ports schematic is illustrated in figure 2.35, while the supply ports, ferrite beads, and decoupling capacitors schematics are exhibited in figure 2.36. This establishes the different power and signal nets for the remaining parts of the schematics.

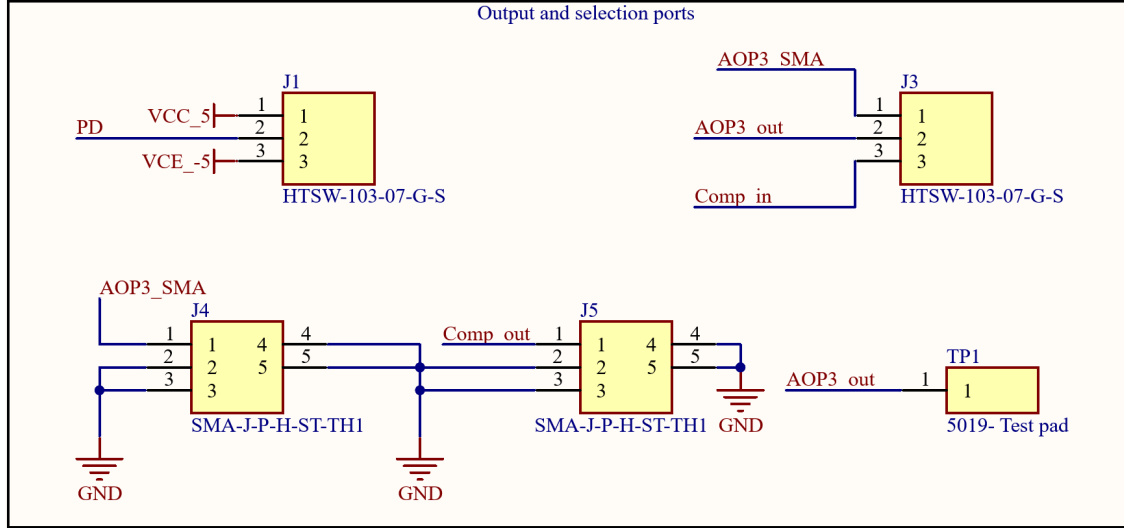


Figure 2.35: Schematic of the output and selection ports of the UWOCs receiver board

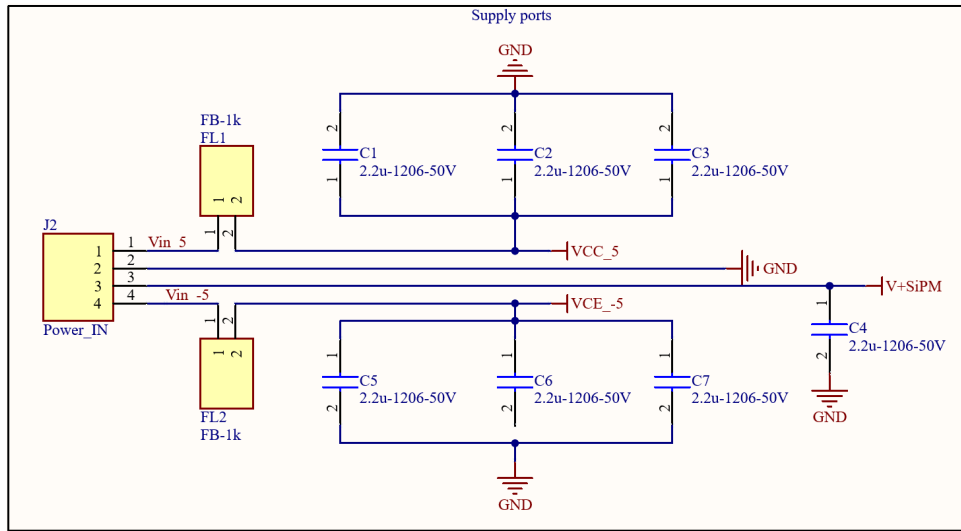


Figure 2.36: Schematic of the output and selection ports of the UWOCs receiver board

Following this, the SiPM MicroFJ60035 is placed. As previously explained, the sensor uses a Ball Grid Array (BGA) packaging, as shown in figure 2.37 and figure 2.38. It has 36 small ball connectors with a diameter of 0.26 mm. According to the SiPM datasheet, most of these connectors are unconnected, but nevertheless help with the thermal dissipation of the board [61]. Since the unused area of the PCB's top layer will be set as grounded copper planes, the unused pads, which are electrically isolated, are connected to the ground. This provides a large copper plane under the sensor to dissipate heat effectively. Similar to the supply section, additional decoupling capacitors are added. Given their lower capacitances, they are placed as close as possible to the SiPM's cathode, and their size is minimized employing the 0603 SMD package, as shown in figure 2.39 for the 100 nF capacitor. These capacitors are multilayer ceramic with a specifically chosen C0G/NP0 dielectric, providing better stability

than the traditional X7R or X5R dielectric [71]. Finally, they are doubled, as the MicroFJ has two cathode input ports. The SiPM schematic with its decoupling capacitors stage is depicted in figure 2.40.

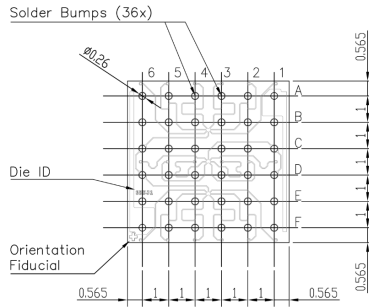


Figure 2.37: Picture of the BGA pads of the MicroFJ-60035. Dimension in [mm]. Taken from [61]

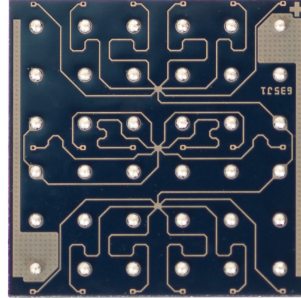


Figure 2.38: Schematic of the BGA pads of the MicroFJ-60035. Taken from [61]



Figure 2.39: Picture of a 100 nF capacitor using 0603 package

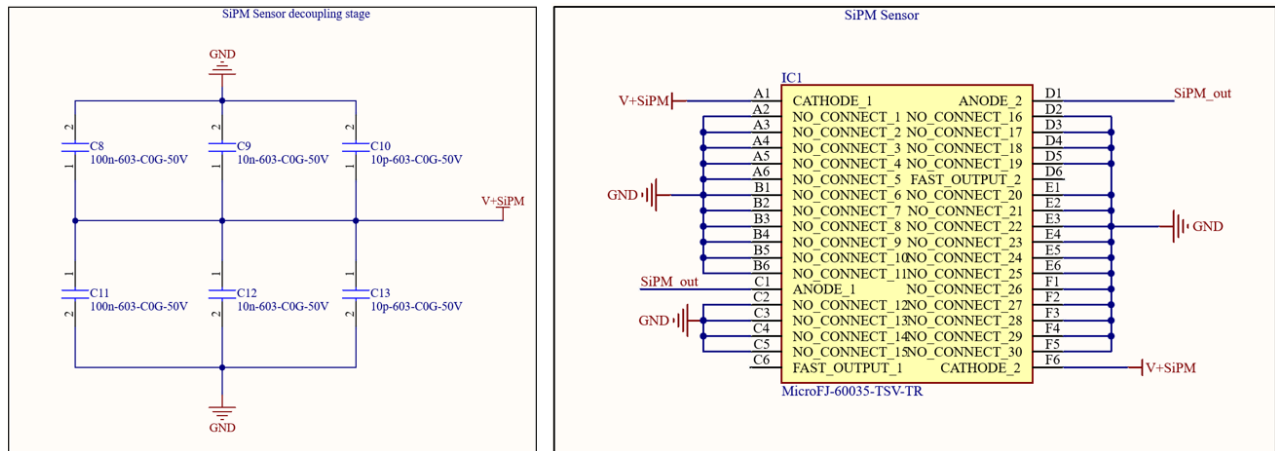


Figure 2.40: Schematic of the SiPM sensors connections and its decoupling capacitors

Afterwards, the different amplification stages are placed. Like the SiPM, different decoupling capacitors of different values will be placed close to the various Op-Amp OPA818 for both the positive and negative supplies. The capacitors are chosen according to the datasheet and application note [89][51]. Most of the resistors involved in the amplification stage are thin-film resistors, which are well-suited for high-speed applications due to their small tolerance, low temperature coefficient, low noise, and better moisture resistance, which is advantageous for underwater environments [71][91]. All components close to the Op-Amp will use 0603 SMD packaging, while others will use 0805 and 1206 packaging that are larger and easier to place. The PD pin of the OPA818 is connected to the 3-pin PCB headers, allowing the Op-Amp to be enabled or disabled by connecting it to either 5 V or -5 V [51]. The thermal pad of the Op-Amps is connected to the ground to provide better heat dissipation. Finally, the gain

resistors are selected with a tolerance $T_R \leq 1\%$ to ensure precise amplification gain. The schematic for the first amplification stage is shown in figure 2.41 and in figure 2.42.

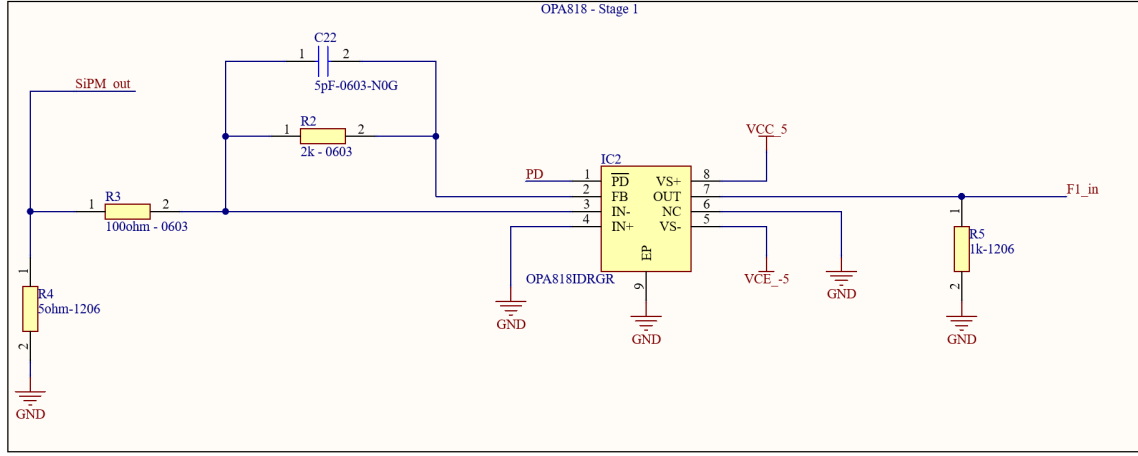


Figure 2.41: Schematic of the first amplification stage using OPA818

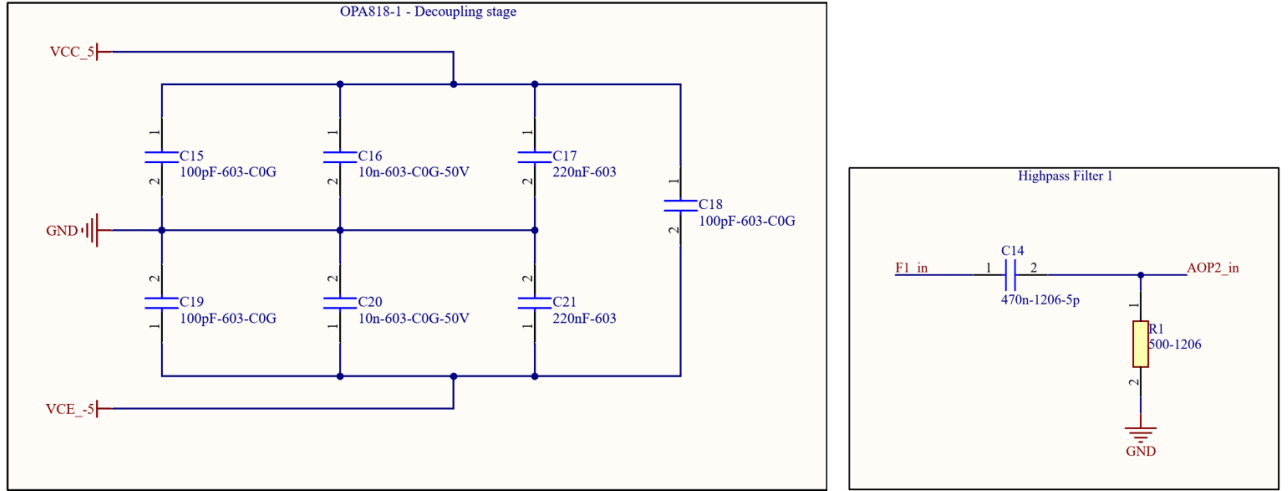


Figure 2.42: Schematic of the decoupling stage of the first Op-Amp and the first high-pass filter

Finally, after setting the amplification stage schematics, the comparator stage components are placed. Like the OPA818 and SiPM, different decoupling capacitors are placed near the supply ports of the TLV3601. Then, the voltage dividers are placed, and to supply the TLV3601 correctly, the supply stage with the two LDOs is also implemented. Various decoupling capacitors are added in the supply stage as suggested in the LDOs' datasheets [78][79]. The schematics are shown in figure 2.43 and figure 2.44.

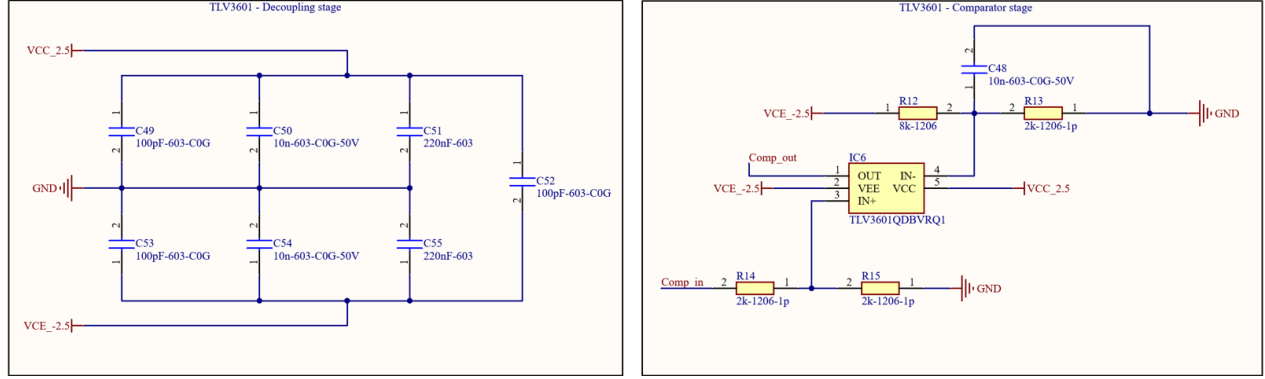


Figure 2.43: Schematic of the TLV3601 comparator with the different voltage divider and its decoupling capacitors

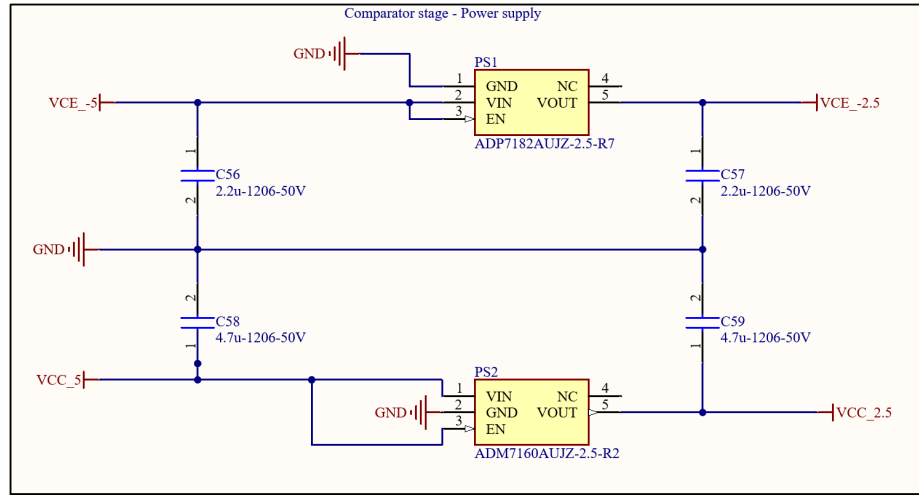


Figure 2.44: Schematic of the comparator stage power supply

PCB Board design

Before placing the components effectively placed on the PCB schematics, the next step is the design of the PCB board itself, which involves determining how the PCB board must be shaped and parameterized.

The shape of the PCB will be circular to fit easily into any circular pressure tanks if tested underwater. Its diameter is limited to 10 cm as it is sufficiently large to place all the components. All inputs and output ports will be placed on the bottom side of the PCB to allow the SiPM sensor and its filter to be easily placed in front of the windows separating the board and the water environment. Then the PCB stack-up is parameterized. A four-layer PCB is chosen to have different power and ground planes and to control the track impedance. The PCB stackup parameters are taken from the PCB manufacturer "PCBWay" and are shown in figure 2.45 [92].

	Layer	Material	Thickness (mm)	Thickness after lamination(mm)
L1-CU	L1-CU	Outer Base Copper 0.5OZ	0.0175	0.0175 (Plating to 1OZ)
PP	PP	7628 RC46% DK:4.56	0.1960	0.1855
L2-CU	L2-CU	Inner Copper 1OZ	0.0350	1.1 (Core with Cu)
L3-CU	CORE	Core DK:4.6	1.0300	
PP	L3-CU	Inner Copper 1OZ	0.0350	
L4-CU	PP	7628 RC46% DK:4.56	0.1960	0.1855
	L4-CU	Outer Base Copper 0.5OZ	0.0175	0.0175 (Plating to 1OZ)

Figure 2.45: Stackup of the designed PCB. Taken from [92]

The first layer will be used to place all surface-mounted device (SMD) components and most of the signal tracks to avoid signal passing through the via and causing parasitic inductance [93][94]. The second layer will be used as a ground plane, whereas the third layer can be employed as a power plane with $V_{L3} = +5V$, and the last layer serves as a power plane as well with $V_{L4} = -5V$ when not used to place the different inputs and outputs components. As it is desirable to control the impedance and set it at 50Ω to avoid signal reflection, the signal track width is calculated using Altium and the different PCB parameters such as the dielectric constant of the dielectric sheet between the top and 1st inner layer, its thickness, and the copper conducting layer thickness [71]. All parameters are thus taken into account to obtain a 50Ω impedance with a track width of $t_w = 12mils$. A mil represents a thousandth of an inch. Finally, the manufacturer's design specifications are taken into account using a systematic design rule check with all limits set. Thanks to this setting, if any rule violation occurs during the design, the software alerts the user and prevents rejection from the manufacturer.

The PCB being parameterized, the components can be placed. The SiPM footprint shown in figure 2.48 is set first in the middle of the board to ease the alignment with the outer window. With the exception of its decoupling filter, no components are placed within a 1.25 cm radius to facilitate the placement of the optical filter mount depicted in figure 2.46 and its schematic in figure 2.47 [95]. When inspecting figure 2.48, it is pertinent to compare the size of the series resistor R4 footprint with the SiPM BGA footprint.



Figure 2.46: Picture of a 50nm hard coated optical filter from Edmund optics. Taken from [95]

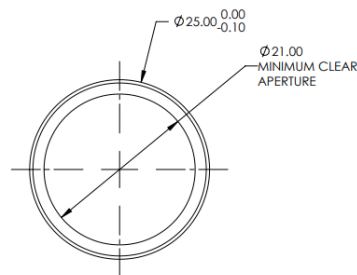


Figure 2.47: Schematic of a 50nm hard coated optical filter from Edmund optics. Taken from [95]

The supply components are then placed, followed by all other components in the order detailed in the making the schematics, in a clockwise direction around the SiPM sensor. As shown in figure 2.49, the different resistors and capacitors involved in the gain of the different Op-Amps are placed close to each Op-Amp's inverting input to avoid parasitic capacitance [51]. This is achievable thanks to the 0603 packaging of the components and the feedback pin being close to the inverting input.

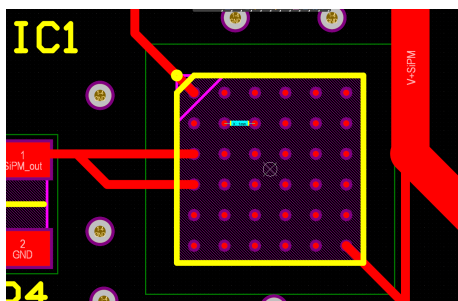


Figure 2.48: Picture of the SiPM footprint on the designed PCB.

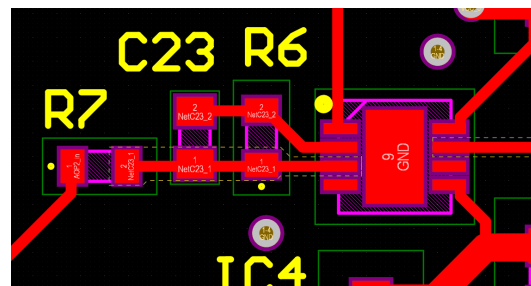


Figure 2.49: Picture of the gain resistor and capacitor of one of the OPA818 on the designed PCB.

Different vias are then used to connect the various power planes to the components and to couple the two ground planes uniformly. The PCB with placed components and their different tracks is shown in figure 2.50. Finally, the different ground and power planes are poured to give the final PCB version, as shown in figure 2.51 and figure 2.52 for the bottom face. Since the different Op-Amps are decompensated to reach high speed - they are very sensitive to any parasitic capacitance, especially at the inverting and output pins [51]. Therefore, all the different copper planes under these inputs are removed until the next component, as visible in figure 2.53.

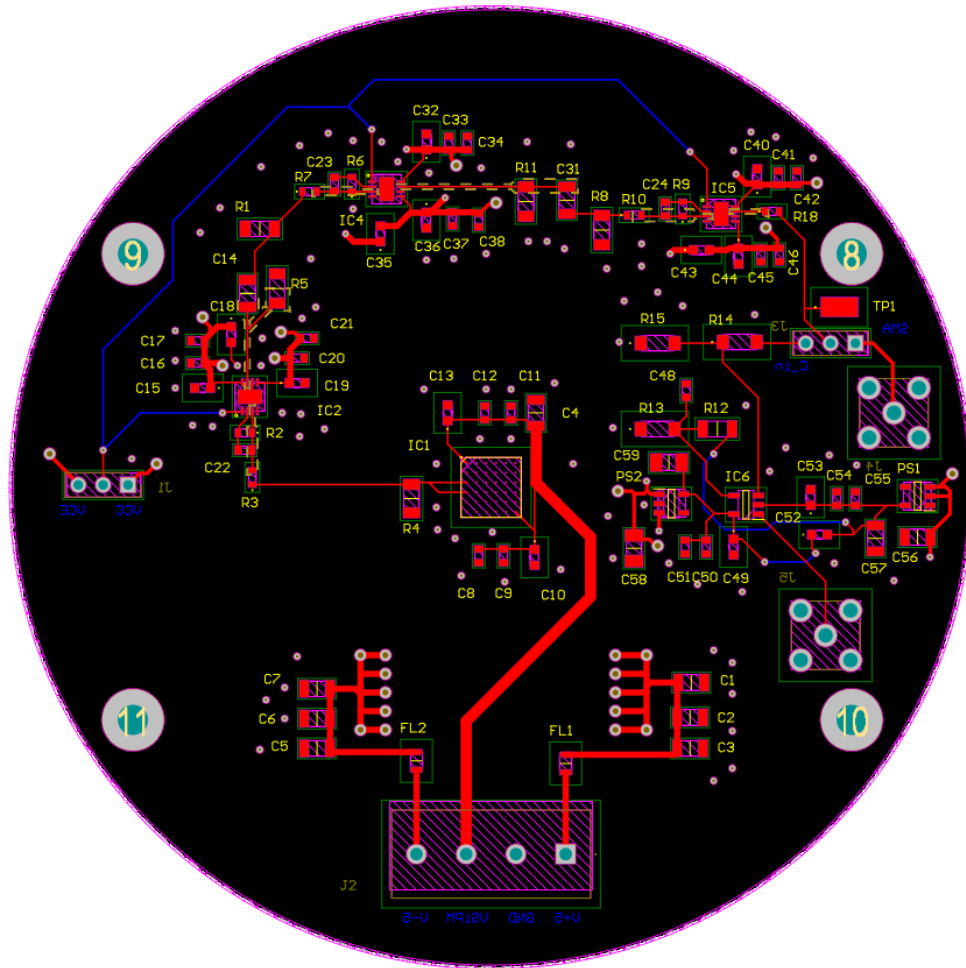


Figure 2.50: Picture of the final PCB layout without the mass and power planes

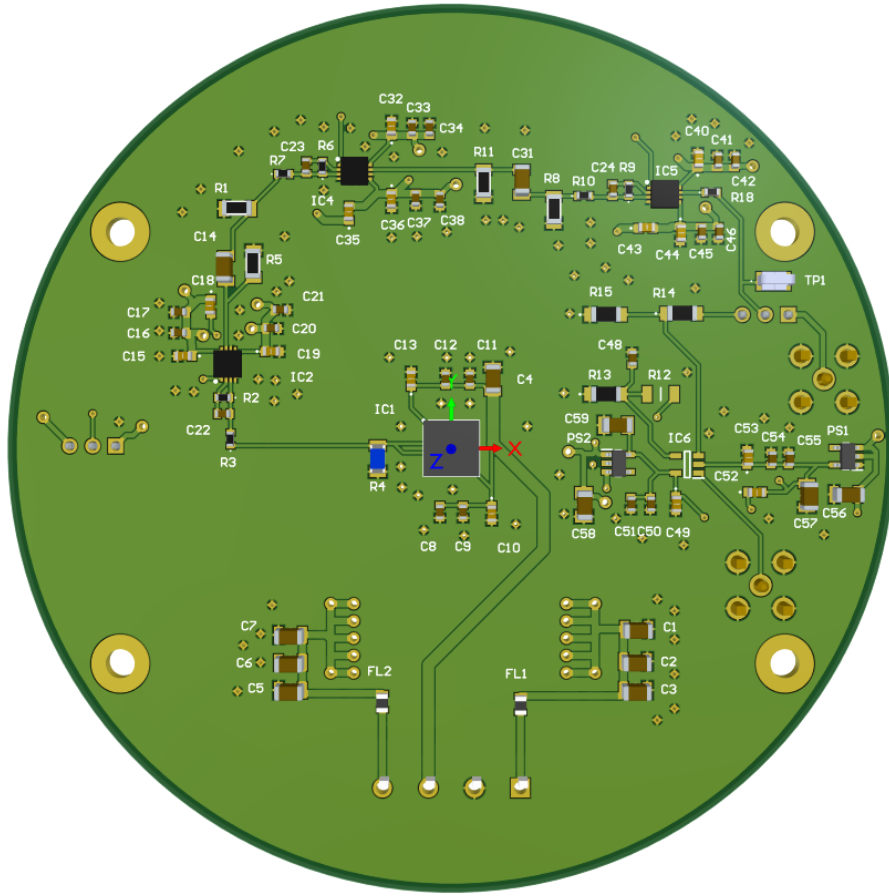


Figure 2.51: 3D image of the final UWOCS receiver PCB.

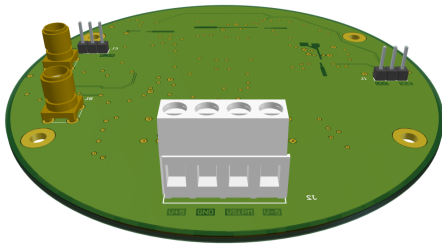


Figure 2.52: 3D image of the bottom of the final UWOCS receiver PCB.

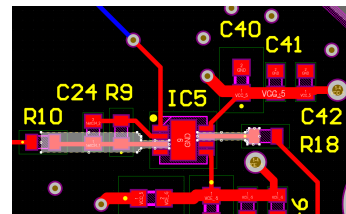


Figure 2.53: Picture of the cut-out plane through the different PCB layer at the inverting input and output of the OPA818

2.1.5 PCB Board realization

With the PCB fully designed, it can be submitted to the manufacturer. For this process, the Gerber and Drill files are exported. Typically, the PCB surface is finished using Hot Air Solder Leveling (HASL), which is the most cost-effective method [96]. However, in this case, due to the BGA pads smaller than 0.3 mm, the surface finish technique selected is Electroless Nickel/Immersion Gold (ENIG). ENIG provides excellent electrical properties and offers highly precise finishing, making it ideal for small footprints like BGA pads. Additionally, a solder stencil will be ordered along with the PCB. The solder stencil helps to gain precision when applying solder paste, as shown below, to solder the various SMD components onto the PCB [97]. Following these requirements, the PCB is manufactured. The unsoldered PCB is shown in figure 2.54.

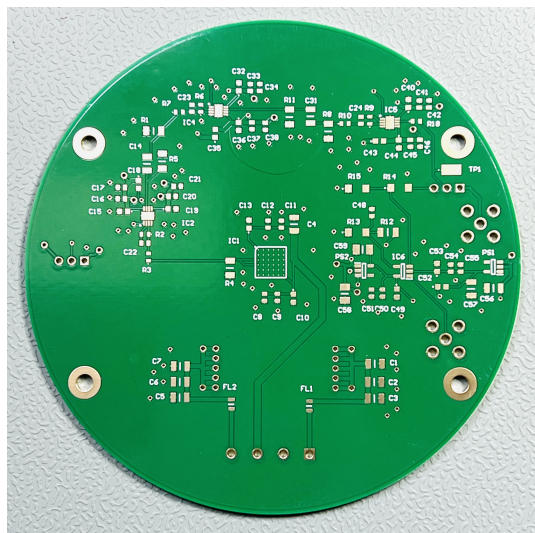


Figure 2.54: Unsoldered manufactured PCB of the UWOCs receiver.

Afterwards, the components have to be placed on the PCB, starting with the SMD components. This process involves applying solder paste to the various footprints on the PCB using the stencil. After the components are set one by one, the PCB, along with the components, is reflowed in a reflow oven to heat the solder paste and solder the components to the PCB [94]. Finally, the through-hole components are soldered using a soldering iron, solder wire, and solder flux. To secure the PCB during this process, it is fixed using another PCB boards, and the stencil is held in place with painter's tape as illustrated in figure 2.55. Then, solder paste is applied and spread over the stencil with a plastic card, as shown on footprints seen on microscope in figure 2.56.

The solder paste, shown in figure 2.57, was specifically chosen for its low-temperature profile, which allows reflowing the components at a lower temperature, as seen in figure 2.58 [98]. This is crucial because the MicroFJ sensor is sensitive to high temperatures and must be reflowed at a lower temperature than other components [61].

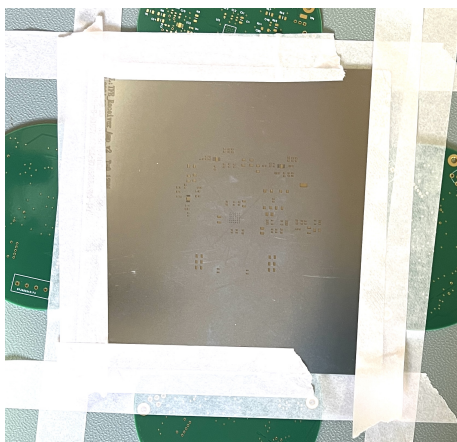


Figure 2.55: UWOCS receiver PCB fixed under its stencil before applying the solder paste

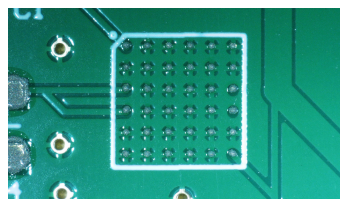


Figure 2.56: Some footprint of the receiver PCB viewed on microscope after applying the solder paste



Figure 2.57: Picture of the solder paste 4902P tube from MG Chemicals. Taken from [98]

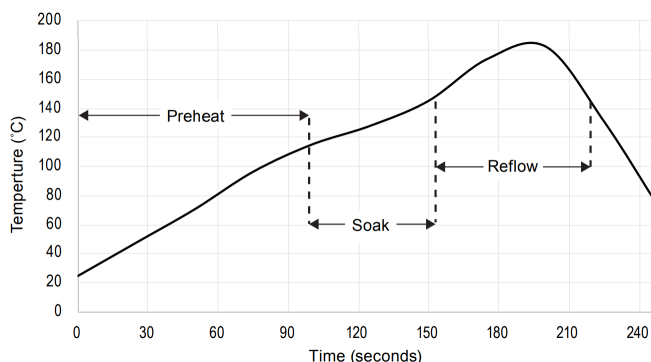


Figure 2.58: Temperature reflow profile of the 4902P solder paste from MG Chemichals. Taken from [98]

The solder paste applied to the various footprints, the SMD components will be placed. All components, except for the capacitors and resistors, are sensitive to Electro-Static Discharge (ESD) and can be damaged if exposed [94]. Therefore, appropriate precautions have to be taken, including the use of an anti-static wrist strap and mats properly grounded with a 1 M Ω resistor to handle the components. Operating with these protections, along with a digital microscope and tweezers, the components are placed one by one, as shown in figure 2.59 and figure 2.60.

At this stage, the PCB is ready to be reflowed. Since a reflow oven was not available, an alternative technique had to be used. This technique involves using a controlled temperature hot plate with a metal container filled with pure white sand [99]. The sand is pre-heated, and then the PCB is placed in the metal container. The hot plate is set slightly over the different required temperatures to reflow the PCB following the heating curve.

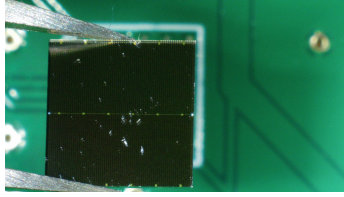


Figure 2.59: The SiPM sensor when placed on the receiver PCB

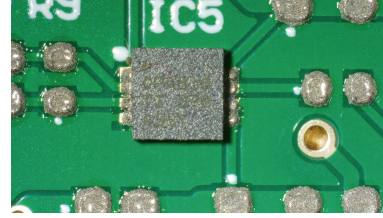


Figure 2.60: Placed components and awaiting footprint with the solder paste

The entire process is monitored using a HIKMICRO B10 thermal camera. This alternative reflow system is depicted in figure 2.61, as well as a thermal monitoring image during reflowing in figure 2.62.



Figure 2.61: Picture of the implemented alternative reflow system.

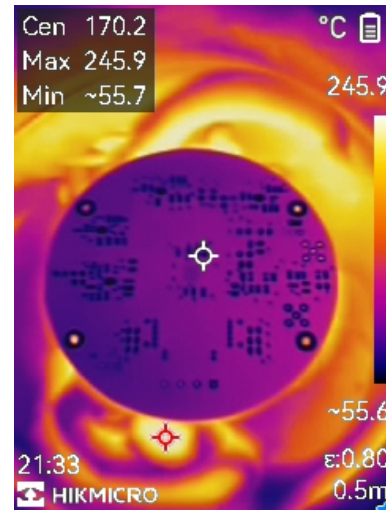


Figure 2.62: Thermal image when the PCB is reflowed

Finally, the remaining through-hole components are hand-soldered, and the PCB is cleaned using ESD-safe pre-saturated isopropyl alcohol wipes. The fully assembled PCB is shown in figure 2.63.

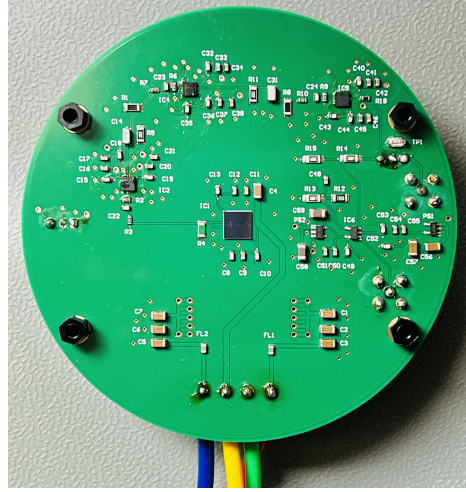


Figure 2.63: Picture of the completed UWOCS receiver PCB

2.1.6 Receiver power supply design and realization

The receiver board completed, the realization of its power supply board follows. Two separate power supplies are designed: the first provides $\pm 5\text{ V}$ to the various operational amplifiers and the comparator via the two LDOs, and the second supplies the 27 V bias voltage required by the SiPM sensor.

The first power supply is implemented using the DKMW15F-05, an isolated DC/DC converter from Meanwell [100]. This converter offers several advantages, such as no minimum load requirement, a wide input voltage range of $I_{in} \in [9\text{ V} - 36\text{ V}]$, and a maximum output current of 1500 mA , sufficient for all active components on the board. Additionally, to enhance supply stability during power bursts, large capacitors are added at both the input and output, which also improves electromagnetic compatibility (EMC) [100][71]. The circuit schematic is shown in figure 2.64.

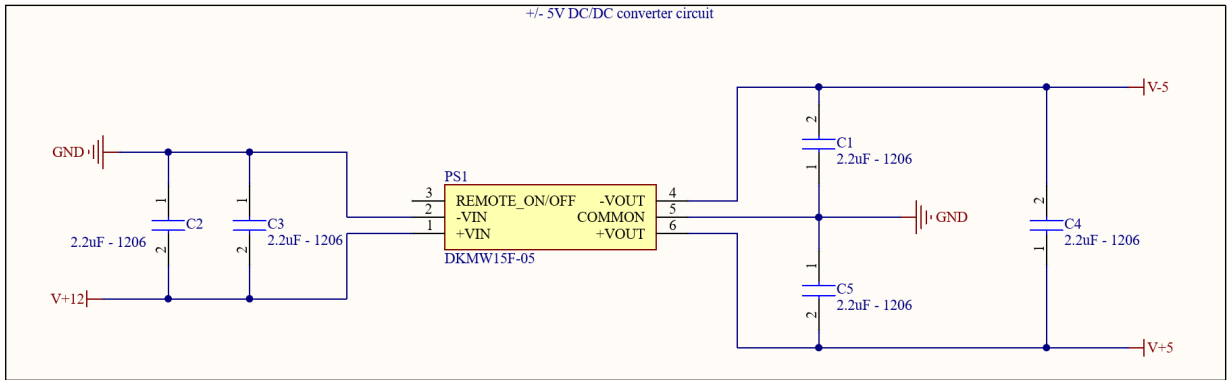


Figure 2.64: Schematic of the $\pm 5\text{ V}$ DC/DC Meanwell converter

Following the $\pm 5\text{ V}$ DC/DC Meanwell converter, the SiPM bias voltage supply is designed.

Since no suitable DC/DC converters are directly available, a boost converter is used, taking the positive 5V output from the Meanwell converter and elevating it to +27V. The chosen boost converter is the ZXLD1615ET5TA from Diodes Incorporated [101]. Additional circuitry is implemented to achieve the required output voltage from the input, as specified in the boost converter datasheet, and shown in figure 2.65.

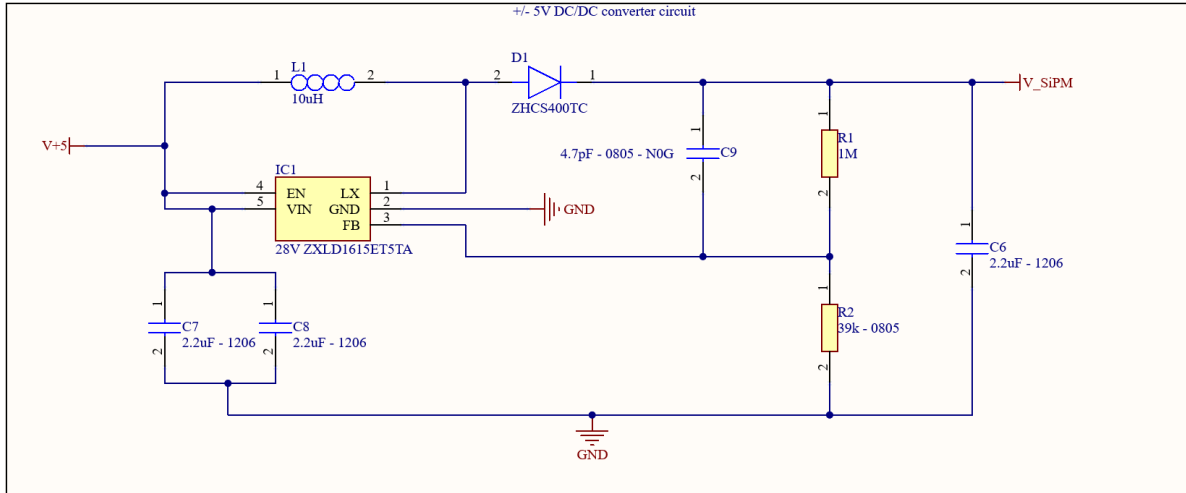
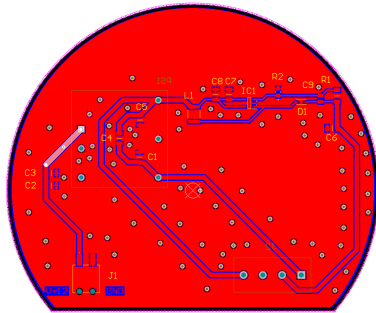


Figure 2.65: Schematic of the boost converter with its auxiliaries components

The PCB for the power supply is then designed similarly to the receiver board, except that only two layers are required, and part of the circular shape is removed to allow space for the various supply cables. Here, no 50 Ω track impedance is required, but the tracks are made wider according to IPC-2221 standards to accommodate higher currents without causing excessive heating and voltage drop [94][71][102]. The bottom layer is grounded to minimize interference, and the PCB layout is presented in figure 2.66 and the final realized PCB in figure 2.67.



2.1.7 Alternative UWOCS receiver design

To conclude the section focusing on the receiver, an alternative design for the PCB receiver board was developed. This alternative design was created to mitigate the risk of malfunction due to the narrow spacing between the BGA pads of the SiPM sensor and the high sensitivity of the OPA818 to parasitic elements, given its decompensated characteristics[61][51]. This, in addition to the thesis deadline and the long PCB manufacturing and delivery times if the first circuit does not work properly.

In this alternative design, the LT1222 operational amplifier from Analog Devices was used, as shown in figure 2.68, along with the SiPM evaluation board, which utilizes wide through-holes instead of the SiPM BGA package [103][61]. The LT1222 is less sensitive to parasitic elements and more stable, as described in its datasheet, while the SiPM evaluation board reduces the risk of short circuits. However, this operational amplifier has disadvantages, including a lower gain-bandwidth product (GBP) and slightly higher noise compared to the OPA818, which could limit the operational range of the implemented UWOCS. Moreover, the through-hole layout of the SiPM evaluation board is not optimal and may introduce unwanted effects [103][61][94].

Nevertheless, this circuit is intended as a contingency plan, to be used if issues arise during testing with the original circuit design. The final PCB design for the alternative solution is shown in figure 2.70.

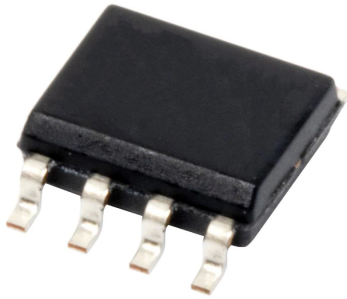


Figure 2.68: Picture of the LT1222 from Analog Devices. Taken from [104]

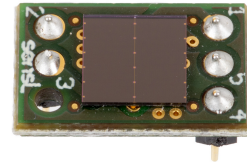


Figure 2.69: Picture of the evaluation board for the SiPM MicroFJ 60035 taken from [61] p.6

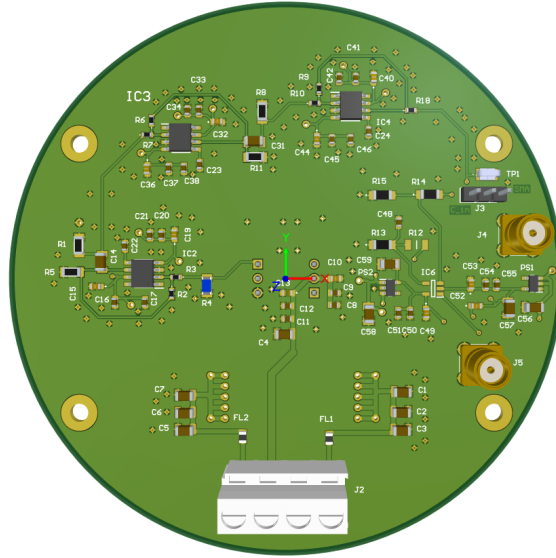


Figure 2.70: Picture of the alternative UWOCs receiver PCB layout

2.2 Emitter Design

This section details the implementation of the emitter part of the UWOC system. It starts with the review and selection of a suitable LED that offers sufficient bandwidth and power for the intended application, along with appropriate lenses or optical concentrators to focus the light into a narrower beam. Afterwards, the LED switching circuit, which manages the LED modulation, is determined. Finally, the operational PCB is designed.

2.2.1 LED review

The light-emitting diode (LED) is a semiconductor device consisting of a forward-biased p-n junction that emits light when the injected carriers undergo radiative recombination [105][38][106].

Electrical characteristics and bandwidth

Electrically, LEDs are similar to other types of diodes and exhibit a comparable current-voltage relationship, as expressed by [71][38][106]:

$$I_{led} = I_s(e^{\frac{V_{led}}{nV_T}} - 1) \quad (2.29)$$

where I_{led} is the current passing through the LED, I_s is the reverse saturation current, V_{led} is the voltage at the LED's anode, n is an ideality factor, and $V_T = \frac{kT}{q} \approx 26$ mV at $T = 300$ K is the thermal voltage. The Figure 2.71 shows the relationship between the current and voltage of a diode. In the figure, V_f represents the forward voltage of the diode, which is the voltage at which the diode begins to conduct a significant amount of current. For LEDs, the forward voltage is typically higher.

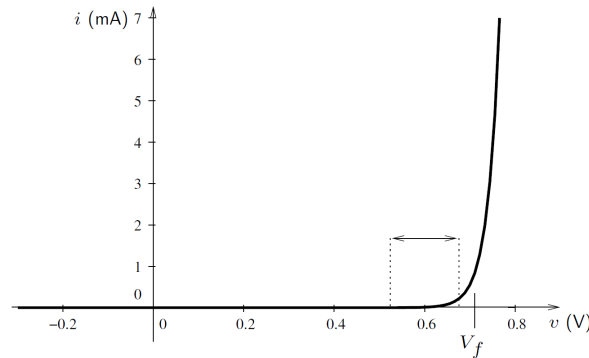


Figure 2.71: Graph of the I-V curve of a diode. Adapted from [107].

The market currently offers a wide range of LEDs with output currents ranging from the milliampere up to several amperes. Regarding bandwidth, LEDs are mainly limited by their internal resistance and junction capacitance, functioning as a low-pass filter with a cutoff frequency given by [38][71]:

$$f_c = \frac{1}{2\pi RC_j} \quad (2.30)$$

where R is the junction resistance and C_j is the junction capacitance. Other factors that influence LED bandwidth include the injected current, the doping level, and the carrier lifetime. Practically, an empirical review of available LEDs shows that few manufacturers provide detailed bandwidth information, especially for high-power LEDs, which are primarily used for general lighting applications and do not require high dimming frequencies. However, past practical visible light communication (VLC) systems have shown that high-power single-color LEDs can generally be used at frequencies up to a few MHz [108][13][18].

Luminous characteristics

Regarding the light emission, the wavelength of the emitted light is primarily determined by the material used in the LED's substrate, while the packaging influences the light emission pattern and efficiency [38]. The table 2.3 presents various substrates used for LED fabrication and their corresponding wavelengths. White LEDs are typically produced by using a blue LED with a wavelength of approximately $\lambda \approx 460$ nm, where phosphor is incorporated into the LED's body to convert part of the blue light into yellow light. This results in a broader spectrum distribution. The Figure 2.72 depicts the emission spectrum of three different white LEDs, with the original intensity peak in the blue region of the electromagnetic (EM) spectrum and a second, broader peak in the yellow region. Due to the presence of phosphor, the LED's bandwidth is more limited, but a blue filter at the receiver - i.e., a filter that restricts the received power to the blue frequency of the EM spectrum - can retrieve the original bandwidth of the blue LED, making white LEDs also suitable for UWOC applications [109].

LED material/substrate	Peak wavelength or range (nm)
AlGaIn/GaN	230–350
InGaIn/GaN	360–525
ZnTe/ZnSe	459
SiC	470
GaP	470
GaAs _{0.15} P _{0.85}	589
AlGaInP/GaAs	625–700
GaAs _{0.35} P _{0.65} /GaAs	632
GaAs _{0.6} P _{0.4} /GaAs	650
GaAsP/GaAs	700
GaAs	910–1020
InGaAsP/InP	600–1600

Table 2.3: Common LED materials and their optical radiation wavelengths. Table taken and adapted from:[38], p.45

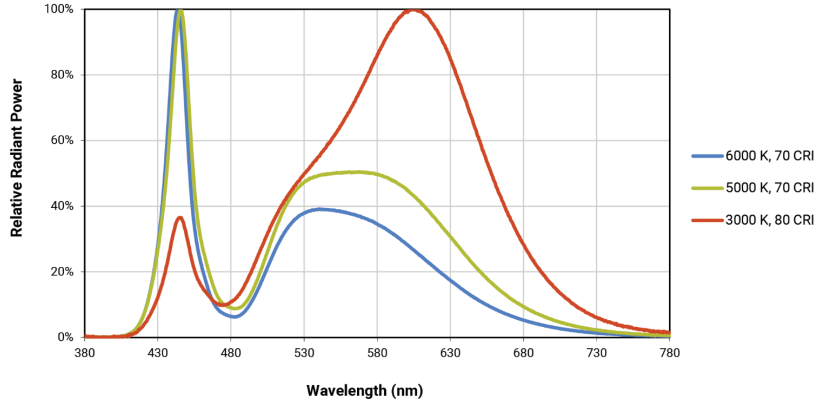


Figure 2.72: The emission spectrum of three Led XLamp XHP35.2 from Cree. Graph taken from [110].

Regarding packaging, the simplest type is the planar structure, as shown in figure 2.73 [38]. In this configuration, the LED emits light in all directions except in the ohmic contact direction. The maximum intensity is emitted perpendicularly to the planar surface, with reduced intensity at the sides, as illustrated in figure 2.74 and described by [38]:

$$I_{led}(\theta) = I_0 \cos(\theta) \quad (2.31)$$

where $I_{LED}(\theta)$ is the light intensity at angle θ , and I_0 is the maximum light intensity at $\theta = 0^\circ$. While the planar package is the simplest, its external quantum efficiency—the number of externally emitted photons relative to the number of carriers passing through the p-n junction—is lower compared to other packages. To improve efficiency, a dome structure is typically used, where the n-type substrate is formed into a hemisphere around the p-type substrate, as shown in figure 2.75 [38].

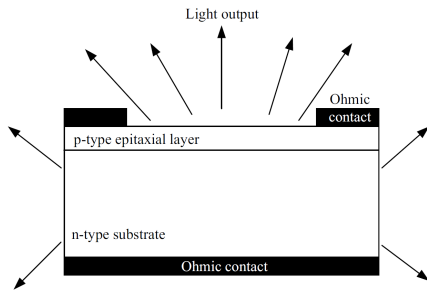


Figure 2.73: Schematic of a Planar LED structure taken from [38] p.46

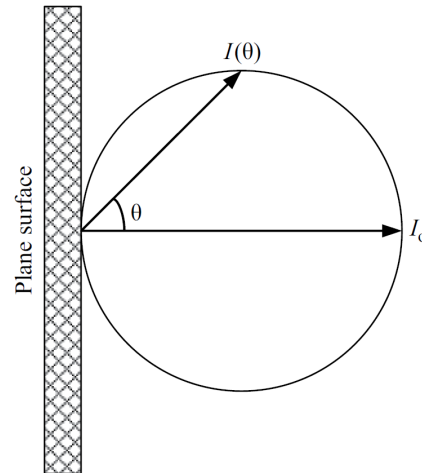


Figure 2.74: Lambertian light intensity distribution of a Planar LED structure taken from [38]

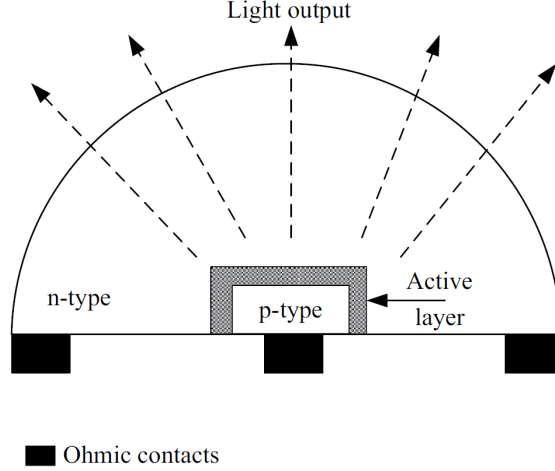


Figure 2.75: Schematic of a Dome led structure taken from [38] p.47

Luminous flux and optical power

As highlighted in the previous sections, maximizing the power received by the UWOCs receiver is crucial. One way to increase this is by enhancing the optical power emitted by the source. Typically, UWOCs systems have optical power outputs ranging from milliwatts to up to 10 watts for high-power devices [13]. However, manufacturers do not always provide information on the LED's optical power but rather on the luminous flux, expressed in lumens [38]. The luminous flux is the optical power weighted by the human eye's sensitivity, normalized to one at the maximum sensitivity of $\lambda = 555 \text{ nm}$, as shown in figure 2.76 and given by [111]:

$$\phi_{lf} = K_m \int_{380}^{830} V(\lambda) P_{op}(\lambda) d\lambda \quad (2.32)$$

where ϕ_{lf} is the luminous flux, $K_m = 683 \frac{\text{lm}}{\text{W}}$ is a scaling factor, P_{op} is the optical power, and $V(\lambda)$ is the normalized human eye sensitivity. For monochromatic sources, the normalized human eye sensitivity can be approximated using [111]:

$$V(\lambda) = 1.019e^{-285.4(\lambda-0.559)^2} \quad (2.33)$$

where λ is expressed in micrometers. An example from [111] illustrates how two lasers, one red and one green, each with the same optical power of 5 mW but with wavelengths of $\lambda = 650 \text{ nm}$ and $\lambda = 532 \text{ nm}$ respectively, appear differently in brightness to the human eye. Using equation (2.33), the red laser has a luminous flux of $\phi_{lf,red} = 0.33 \text{ lm}$, while the green laser has $\phi_{lf,green} = 2.83 \text{ lm}$. This means the green laser will appear approximately 8.5 times brighter to the human eye, even though it does not deliver more optical power.

Lastly, LEDs generally have a spectral width, i.e., the windows in the EM spectrum where 50% of the power of the Led is emitted, of $\Delta\lambda \in [30 \text{ nm} - 60 \text{ nm}]$ at $\lambda = 850 \text{ nm}$ [38]. The Figure 2.77 shows the electromagnetic spectral power distribution of various LEDs from Lumileds.

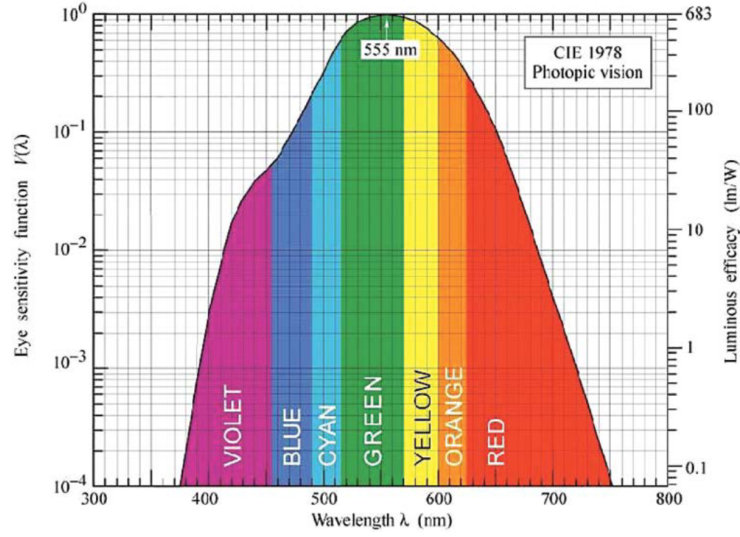


Figure 2.76: Eye sensitivity function and Luminous efficacy functions of the Wavelength λ . Taken from [38] p.50

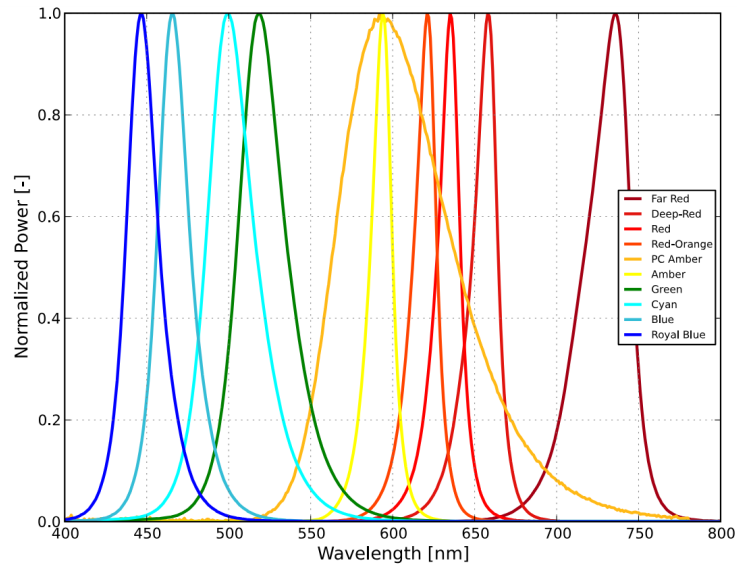


Figure 2.77: Electromagnetic spectral power distribution of different Leds from Lumileds. Taken from [112] p.7

Optical lens

To conclude this review, it can be ascertained that optical lenses or concentrators can be added to the LED structure to reduce the original beam spread and increase the irradiance at the receiver. However, this improvement comes at the cost of requiring a more precise alignment [54]. As such, the final beam angle typically ranges between 10° and 120° .

2.2.2 Led and driver selection

Following this review of LEDs and their characteristics, the appropriate LED has to be selected while considering the requirements outlined in the UWOCs specification and receiver sections.

The first consideration is to ensure an optical power of $P_l \geq 3 \text{ W}$ to provide sufficient power when the receiver is far from the emitter. The LED should emit within the optimal EM spectrum range for clear ocean water, meaning a peak wavelength between $\lambda = 450 \text{ nm}$ and $\lambda = 500 \text{ nm}$, with a small margin if necessary. White LEDs are not considered since a significant portion of their power is emitted outside the required EM wavelength band. Regarding the necessary bandwidth, the selected LED should be capable of handling square pulse signals up to 2 MHz, in line with modulation requirements. Lastly, the LED should be easily available from marketplaces like Farnell, Mouser, or Digikey, should not be at the end of its lifecycle, and should have compatible lenses or optical concentrators available for handling both narrow and wide beam angles.

The table 2.4 show a synthesis of the different requirements in order to select the appropriated Led from the market.

Features		Requirement
Optical Power		$P_l \geq 3 \text{ W}$
Number of LEDs		Multiple if needed
EM Spectrum band	$\lambda_{P-50\%} = [\lambda = 450 \text{ nm}, \lambda = 500 \text{ nm}]$	
Bandwidth		$B \geq 2 \text{ MHz}$
Availability		Farnell - Mouser - Digikey
Lifecycle		Not end-of-life status
Beam handling	Lenses or optical concentrators available	

Table 2.4: LED Requirements for the proposed system.

After a brief overview of the marketplace, the LED GD CSSRM3.14-AJAM-24-1-700-R33 from AMS Osram, shown in Figure 2.78, is selected [113]. This recent high-power LED has a peak wavelength set at $\lambda = 445 \text{ nm}$, as shown in Figure 2.79, and a luminous power of at least $P_l = 1500 \text{ mW}$ with a current of $I_{LED} = 700 \text{ mA}$. Additionally, the half-power spectral bandwidth of the LED is $\lambda_{P(50\%)} = 18 \text{ nm}$, which is compatible with the receiver's optical filter bandwidth.

To power the LED, a suitable driving circuit must be implemented. Typically, a high-speed LED driver circuit consists of a LED in series with a resistor to limit the current, along with a MOSFET transistor that controls the current flow through the LED (High state for allowing current passing, Low state for blocking it) [114]. The MOSFET gate is controlled by a MOSFET driver, which is triggered by the modulated signal, as shown in Figure 2.80. However, this configuration introduces additional steps between the input signal and the LED's light output, which may cause delays and uncertainties in pulse intervals. Given the fixed pulse duration of $T_p = 500 \text{ ns}$, a simpler solution is to use the MOSFET driver directly

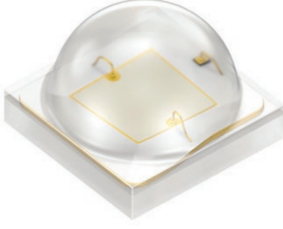


Figure 2.78: Picture of the LED GD CSSRM3.14 from OSRAM. Taken from [113] p.1

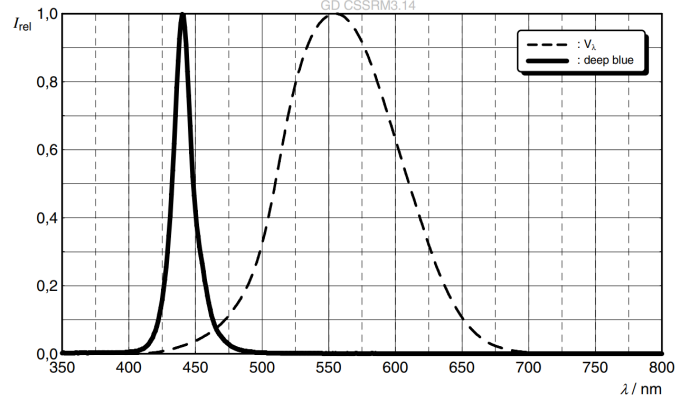


Figure 2.79: Spectral bandwidth of the LED GD CSSRM3.14 from OSRAM. Taken from [113] p.8

to power the LED, as shown in Figure 2.81. This approach reduces circuit complexity, and since MOSFET drivers can deliver high peak current, they will quickly charge the LED's capacitance $C_{LED} \approx 100$ pF, thereby increasing the circuit's switching speed [71][115][116].

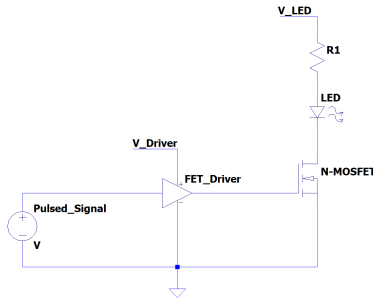


Figure 2.80: Schematic of a usual high speed LED driver circuit. Adapted from [114] p.2

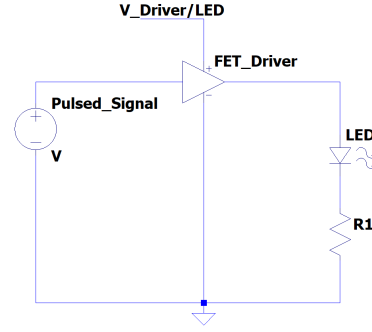


Figure 2.81: Proposed high speed LED driver circuit. Taken from [113] p.8

For this application, the MIC4422AYM driver from Microchip was selected [115]. According to its datasheet, this driver is capable of functioning as a pulse generator, delivering a peak current up to 9A, with a low delay time of $T_d \approx 15$ ns.

The driver being selected, the next step is to configure the circuit parameters. First, the LED current needs to be set, ensuring that the driver does not overheat in this configuration. After analysis, the LED current is set at $I_{LED} = 1250$ mA. This current, which is below the maximum pulsed current specified in the LED's datasheet, will result in a forward voltage of $V_{f-LED} \approx 3$ V [113]. Using the typical output resistance of the driver $R_o = 0.6 \Omega$ and Kirchhoff's law, the series resistance is calculated as [71][115]:

$$R_s = \frac{V_{driver} - R_o I_{led} - V_{f-LED}}{I_{Led}} \quad (2.34)$$

where V_{driver} is the supply voltage of the driver. To optimize the driver's bandwidth according to its supply voltage, V_{driver} is set at 5 V, resulting in a series resistance of value, $R_s = 1 \Omega$, and a peak power dissipation of $P_{Rs} = 1.25 \text{ W}$. With this current, the LED's optical power is $P_l = 2600 \text{ mW}$.

Afterwards, the power dissipation and temperature rise of the driver are evaluated to ensure that they remain within acceptable limits. The total power dissipation is calculated by summing the resistive load dissipation (P_R), capacitive load dissipation (P_C), quiescent power dissipation (P_Q), and transient power dissipation (P_T) [115][71][94]. The resistive load dissipation is calculated as:

$$P_R = I_{LED} R_o D = 375 \text{ mW} \quad (2.35)$$

where $D = 0.5$ is the duty cycle of the pulsed signal. For 8-DPIM modulation, the worst-case scenario occurs when multiple first symbols are transmitted, leading to a pulse of $T_p = 500 \text{ ns}$ followed by an absence of a pulse for $T_a = 500 \text{ ns}$. Then, the capacitive load dissipation is given by:

$$P_C = \frac{f_s C_{LED} V_{driver}^2}{2} \approx 1 \text{ mW} \quad (2.36)$$

where, $f_s = 1 \text{ MHz}$, is the switching frequency. As previously, regarding 8-DPIM modulation, the worst case occurs when multiple 1st symbols are transmitted. Following this, the quiescent power dissipation is calculated as:

$$P_Q = V_{driver} (D I_H + (1 - D) I_L) \approx 4 \text{ mW} \quad (2.37)$$

where I_H and I_L are the quiescent currents provided in the datasheet for high and low input states, respectively. Finally, the transient dissipation is calculated as:

$$P_T = 2 f V_{driver} A_s = 40 \text{ mW} \quad (2.38)$$

With $A_s = 4 \text{ nAs}$, the crossover energy given in the datasheet.

The total power dissipation is thus:

$$P_{tot} = P_R + P_C + P_Q + P_T = 420 \text{ mW} \quad (2.39)$$

The driver case temperature T_c is then calculated using the junction-to-case thermal resistance $\Theta_{JC} = 38.8 \frac{^\circ\text{C}}{\text{W}}$ [71][115][94]. The driver's case temperature rise will be efficiently dissipated using an aluminum board and a proper heatsink, with an initial temperature of $T_{ini} = 25 \text{ }^\circ\text{C}$. The result is:

$$T_c = T_{ini} + P_{tot} \Theta_{JC} \approx 41 \text{ }^\circ\text{C} \quad (2.40)$$

The values remain within the limits specified in the datasheet [115]. In these calculations, the internal resistance of the driver was taken as $R_o = 0.6 \Omega$, which is the typical value. However, the internal resistance, according to the driver's datasheet, can reach exceptionally reach a maximum value of $R_o = 1 \Omega$. Accounting on this resistance value, the LED current should

decrease to $I_{LED} = 1000 \text{ mA}$, while the forward voltage remains approximately the same. The previous calculations are repeated with this new resistance and LED current, resulting in a case temperature of $T_c \approx 46^\circ\text{C}$, which remains slightly higher but is nevertheless still acceptable.

After deciding the driver specifications, the number of LEDs has to be stipulated. As explained previously, the first LED with a larger beam will be used to provide a wide operating area at a shorter distance. The 10170 optical concentrator from Carclo Technical Plastics will be employed with a beam angle of $\Theta_W \approx 75^\circ$ [117], as shown in figure 2.82. For longer distances, two LEDs will be selected to meet the optical power requirement defined earlier, and the "Regina" narrow beam optical concentrator from Ledil will be used with a beam angle of $\Theta_N \approx 8^\circ$, as shown in figure 2.83[118].



Figure 2.82: Picture of the wide beam optical reflector used in the emitter board. Taken from [117]



Figure 2.83: Picture of the narrow beam optical reflector used in the emitter board. Taken from [118]

2.2.3 Emitter PCB design and realization

Given that the LEDs, their drivers, and optical concentrators are specified, the emitter PCB has to be designed next. Similar to the receiver board, the remaining components have first to be selected, including auxiliary parts such as decoupling capacitors and input ports. Special attention is given to the selection of the series resistor to ensure a proper heat dissipation. The schematic of the first LED circuit is shown in figure 2.84. The other LED circuits are similar.

Then, the PCB itself is designed. As the LED and driver need to dissipate heat, the PCB core material will be made of aluminum. The components are placed and the track widths are made sufficiently large according to the IPC 2221 standard to avoid overheating and voltage drop [94][102]. To accommodate this imperative, the input ports are doubled to maintain acceptable track widths, as shown in figure 2.85. Additionally, no components are placed within a 15 mm radius from the LED centers to allow for the placement of the optical concentrators. The final PCB layout is shown in figure 2.86. All components are SMD, as it is difficult to solder through-hole devices on an aluminum board due to its high heat dissipation capabilities [119]. As a result, when hand soldering is practiced, the board

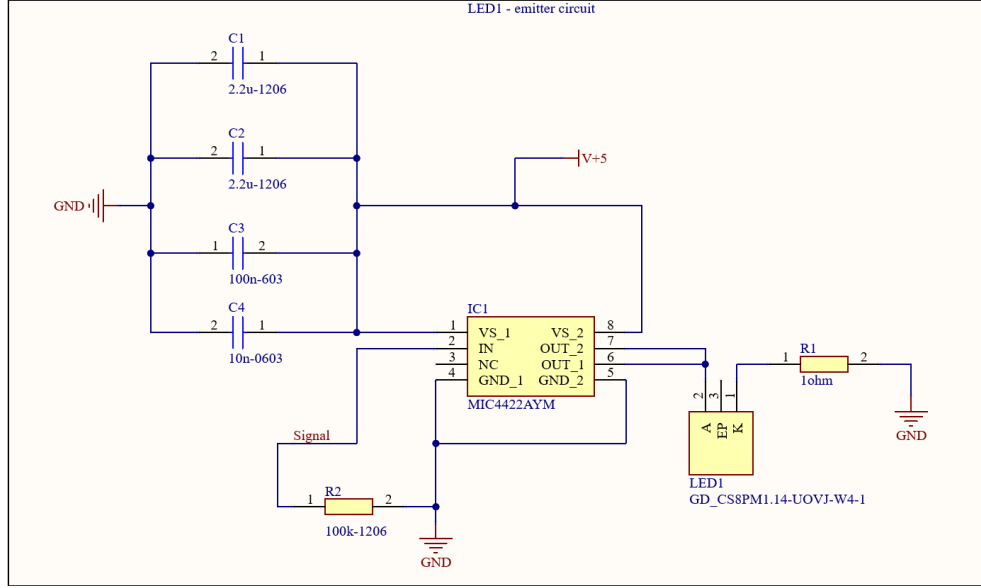


Figure 2.84: Schematic of the first LED circuit of the UWOCs emitter board

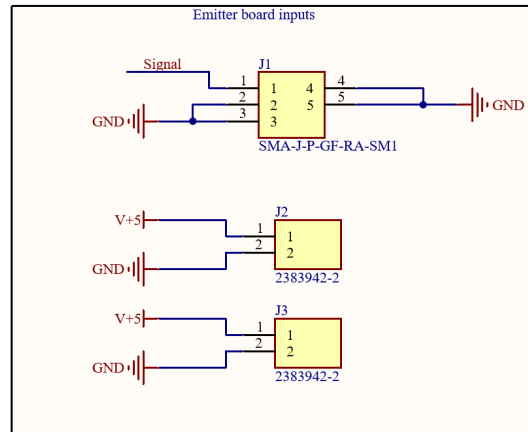


Figure 2.85: Schematic of the input ports of the UWOCs emitter board

remains cold, and the solder does not adhere to the PCB while when reflowing the SMD all the board is heated and the temperature remains constant along its structure.

Finally, the aluminum core PCB is ordered, and the manufactured PCB is shown in figure 2.87. Similar to the receiver board, the components are placed using solder paste applied on the footprint with a dedicated stencil, as shown in figure 2.88. After component placement, the PCB is reflowed using the same low reflow temperature profile as the receiver board, since the LEDs are also sensitive to high reflow temperatures [94][113]. The final assembled PCB with the optical concentrators is shown in figure 2.89.

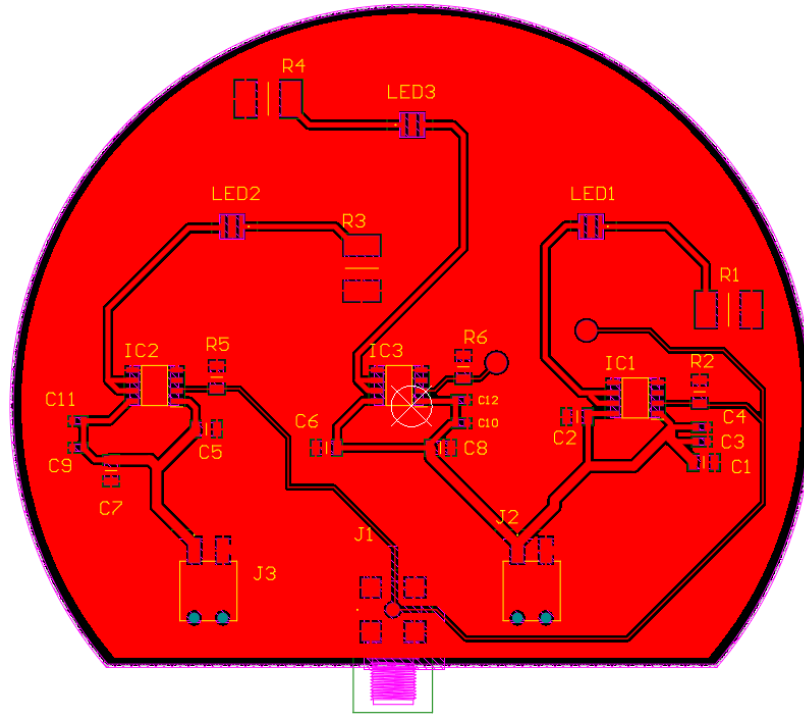


Figure 2.86: Design of the UWOCS emitter board

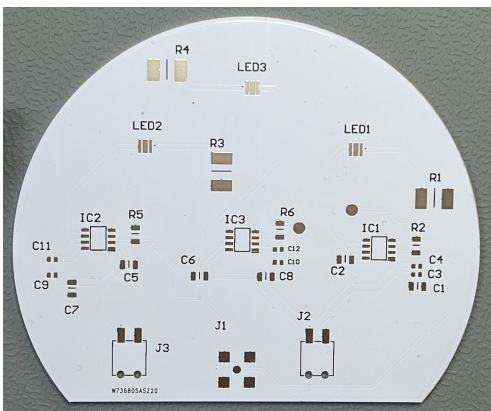


Figure 2.87: Picture of the manufactured UWOCS Emitter board

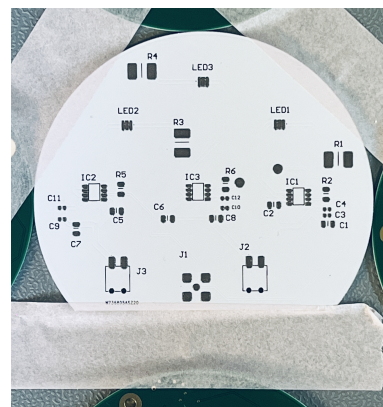


Figure 2.88: UWOCS Emitter board with solder paste applied on it

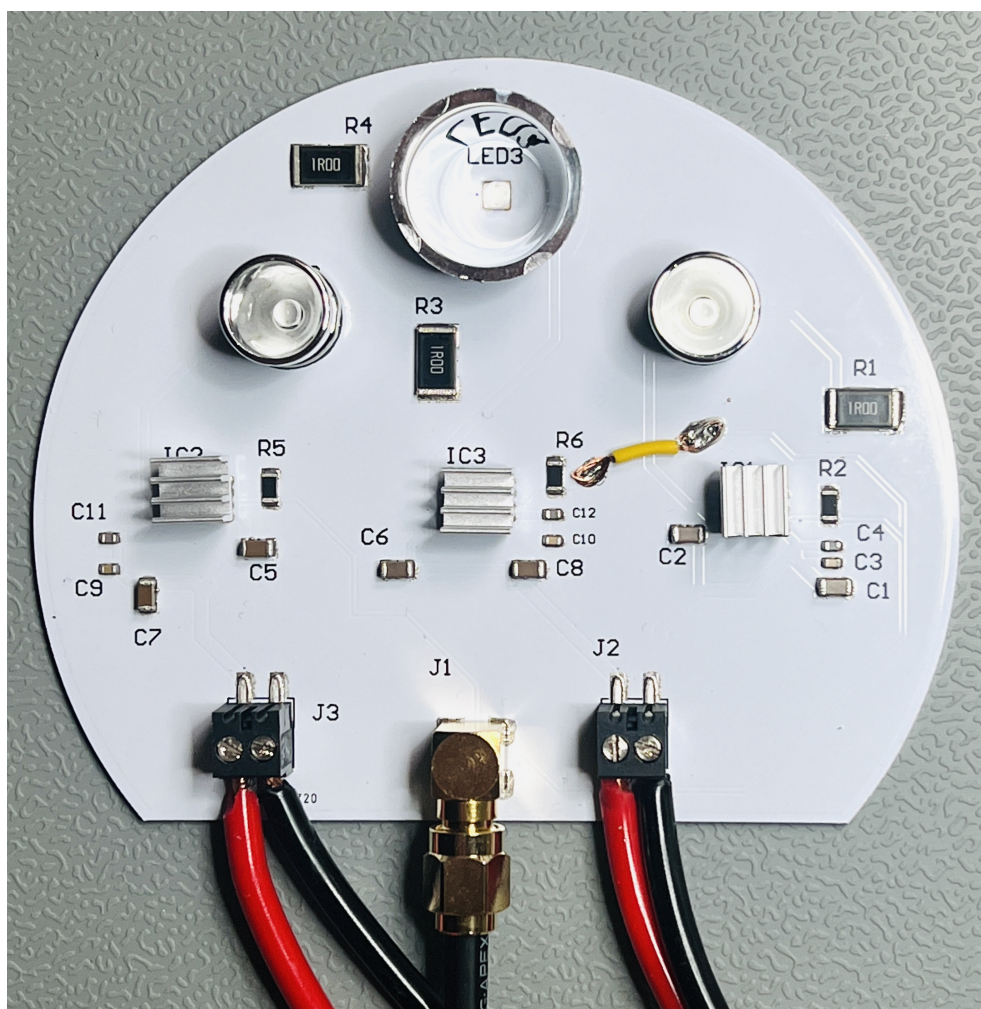


Figure 2.89: Final assembled UWOCS emitter board with their optical concentrators

2.2.4 Receiver power supply design and realization

With the emitter board completed, the implementation of its power supply board follows, utilizing the RSDW60F-05, an isolated DC/DC converter from Meanwell [100]. As is the case for the receiver board, this converter offers several advantages, notably no minimum load requirement, a wide input voltage range of $I_{in} \in [9V - 36V]$, and a maximum output current of 12 A. It is largely sufficient to supply the LEDs and their driver. This circuit also has the advantage of requiring no additional components to function. However, to comply with the EMC Class A standard, additional capacitors and inductors are placed at the input and between the input and output of the DC/DC converter. This is shown in figure 2.90, in accordance with the converter's datasheet [120].

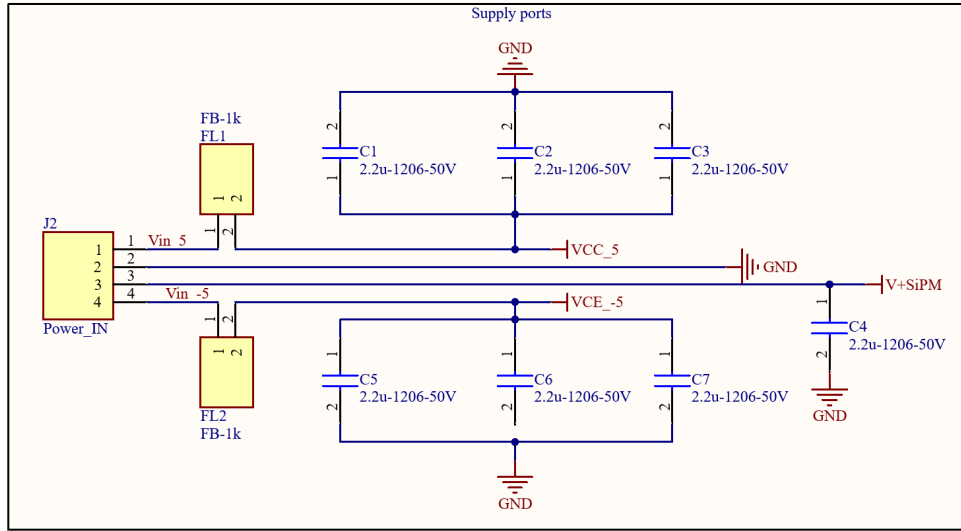


Figure 2.90: Schematic of the RSDW60F-05 DC/DC Meanwell converter

The PCB is then designed with two layers, similarly to the receiver supply board, with a section of the circular shape removed to allow space for the supply cables. The tracks are also made wider according to IPC-2221 standards to accommodate the LED supply currents without causing excessive heating or voltage drop [94][71][102]. The bottom layer is set to the output voltage to provide the largest supply path, while the unused upper layer is grounded. The final PCB layout is shown in figure 2.91.

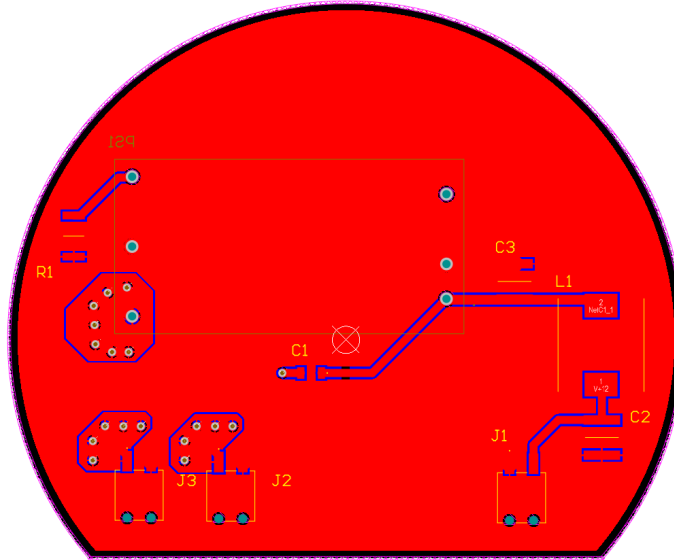


Figure 2.91: Picture of the final emitter supply PCB layout

Finally the PCB is manufactured and the figure 2.92 and figure 2.93 show the final Emitter supply board with all its components placed employing the same method described for the previous boards.

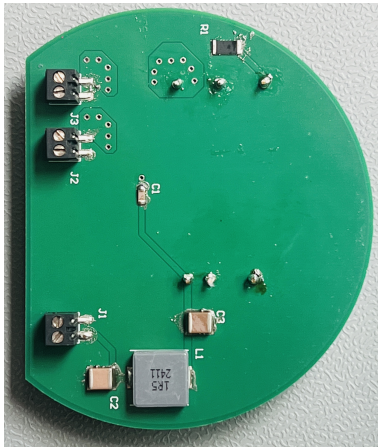


Figure 2.92: Picture of the emitter supply board with its components placed on it



Figure 2.93: Picture of the emitter supply board with its components placed on it (bottom)

CHAPTER 3

SYSTEM EVALUATION AND DISCUSSION

As the emitter and receiver are realized, the complete system is evaluated in this section. Firstly the design and realisation of a test bench is described. Then the implemented UWOCs is tested at different distances and powers in order to validate its operability within the requested range. Finally the different results are discussed, particularly in regards to the objectives of this Master Thesis.

3.1 Test bench design and realization

3.1.1 Test bench design

In order to evaluate the system, a test bench is designed and crafted. To reproduce a realistic clear ocean underwater condition, both emitter and receiver board are placed in a light hermetically closed box and where a water pipe is fixed in between with a transparent glass and the box. Then the water pipe is filled with salt water using 34.7 g per Kg of pure water [121]. On the emitter side, a function generator is employed to generate the pulse signal while on the receiver side an oscilloscope is used to analyse the received signal quality. This is achieved with the oscilloscope raw signal, a Fast Fourier Transform and an eye diagram. The schematic of the test bench is showed in figure 3.1.

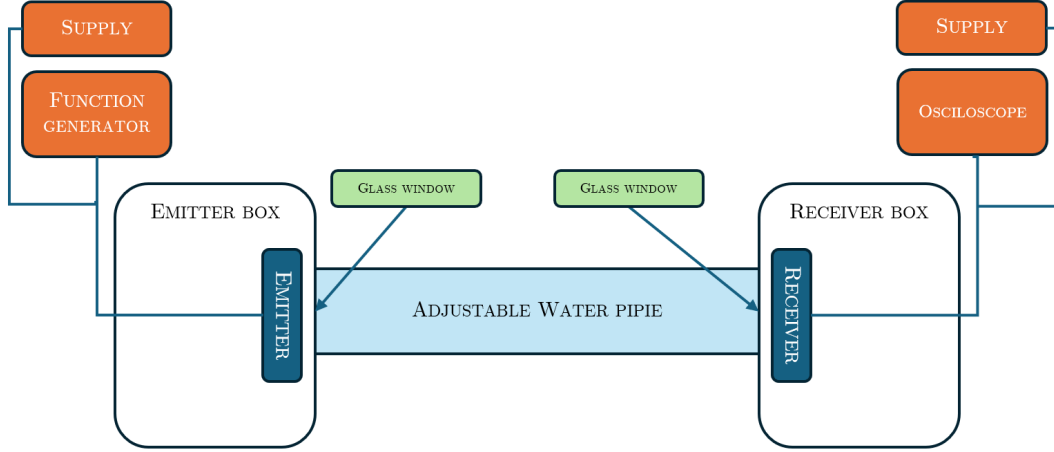


Figure 3.1: Schematic of the implemented test bench in order to evaluate the UWOCs.

3.1.2 Test bench realization

The test bench is crafted using marine plywood to construct the two boxes that should received the emitter and receiver while the pipe is made of a PVC tube. A 100 mm hole is drilled in each of the front plywood planks in order to fix the pipe support as shown in *figure 3.2* and *figure 3.3*. Then the pipe support is glued on the test bench with the first pipe section. On each side, the first pipe section has an additional conduct in order to fill and evacuate the water while also avoiding air bubbles. Then the internal glass is fixed as depicted in *figure 3.5* and the plywood box is assembled as shown on *figure 3.4*. Afterwards, the plywood boxes are isolated from outdoor light using black speed tape and the pipe is assembled, linking the two boxes. The final test bench is shown in *figure 3.6* and the pipe tube as seen from inside the box in *figure 3.8*. Lastly, the emitter and receiver are fixed in their respective box as shown for the receiver in *figure 3.8*.



Figure 3.2: Pipe support of the test bench under construction

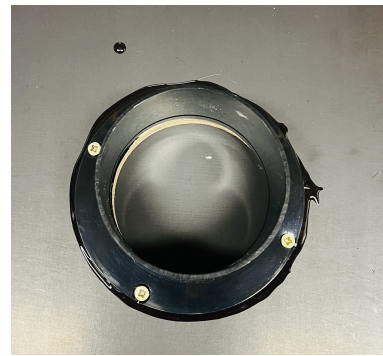


Figure 3.3: Test bench pipe's support glued

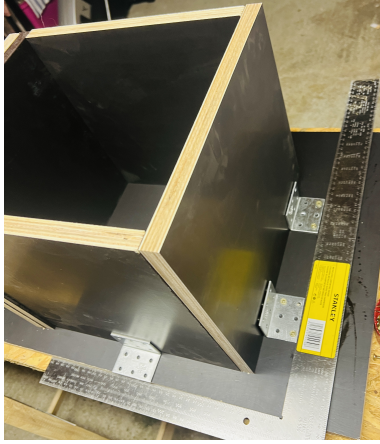


Figure 3.4: Emitter and receiver isolated box under construction



Figure 3.5: Test bench's internal glass



Figure 3.6: Test bench deployed with the pipe extension along it.

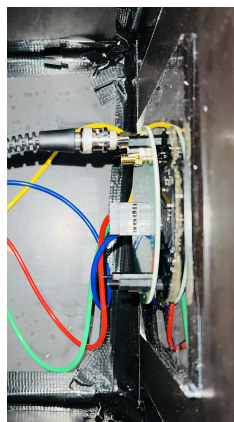


Figure 3.7: Receiver fixed on the test bench

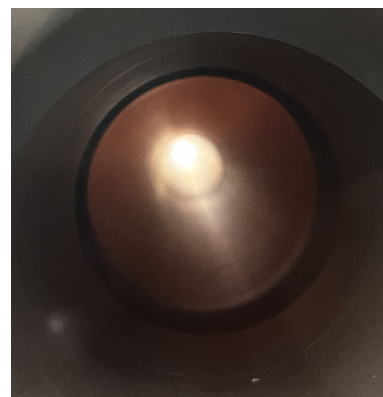


Figure 3.8: Test bench pipe

3.1.3 UWOCS evaluation

The test bench is completed, the implemented UWOCS can be tested. The tests is to be conducted at different distances to evaluate the received signal across the desired operational range. To this end, the pipe section will be set at 4.5 m and 14.5 m, to allow the evaluation of the UWOCS at short and medium ranges. However, it is not feasible to extend the pipe up to 50 m, so an alternative approach had to be found for the longest range .

To simulate this condition, one LED will have its optical concentrator removed to increase the beam angle to 120° , while the other LEDs will be masked. Additionally, two crossed polarizer filters from KentFaith will be added in front of the unmasked LED, as shown in figure 3.9 and figure 3.10 [122][63]. According to their specifications, when positioned in a crossed orientation, these filters should reduce the incoming light by 99.9%.

With this configuration, using equation (2.2) and equation (2.3), and based on the initial LED light power, the current flow from the SiPM sensor at a distance of 4.5 m will be approximately $I_{SiPM}^{4.5m} \approx 33 \mu A$. This is slightly below the expected SiPM current when the receiver is at the maximum specified range. This setup will serve to demonstrate that the UWOCS is functional at its maximum distance using the implemented test bench.



Figure 3.9: Emitter superimposed by the two polarisers uncrossed

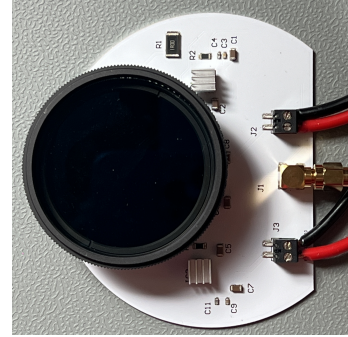


Figure 3.10: Emitter superimposed by the two polarisers crossed

Evaluation with an emitter-receiver distance of 4.5m

The first test presented is conducted with an emitter-receiver distance of 4.5m. The emitter's function generator is configured to generate an ongoing signal composed of a pulse of period $T_s = 500ns$ followed by an absence of pulse of period $T_a = 500ns$ representing the first symbol (1) from the 8-DPIM modulation. This signal is taken directly at the output of the comparator stage and the results are shown in figure 3.11, figure 3.12 and in figure 3.15.

The test was then repeated using an emitted signal representing the third and the last symbol, to observe how the signal is received with different symbols of the 8-DPIM modulation. The results for the third symbol are shown in figure 3.16, while the results for the last symbol

are presented in figure 3.13, figure 3.14, and figure 3.17. The three Fast Fourier Transforms illustrate how the signal is represented in the frequency domain, depending of the emitted symbol [36].

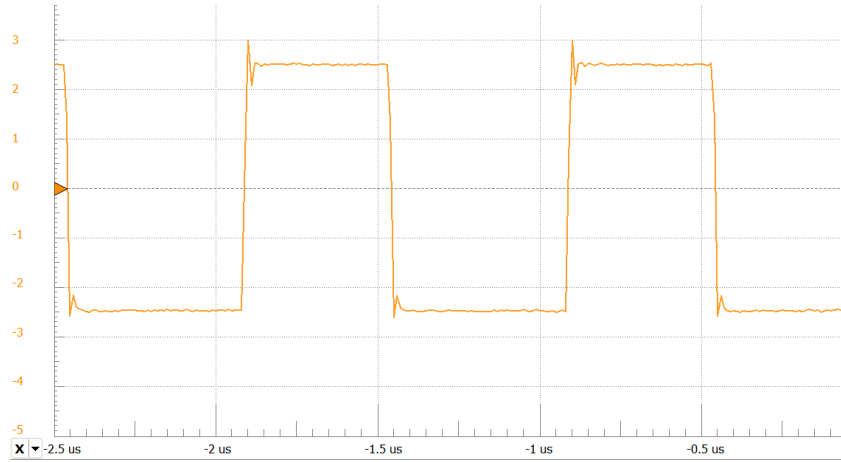


Figure 3.11: Comparator signal with the emitter and receiver at a distance of 4.5m and with symbol 1 transmitted

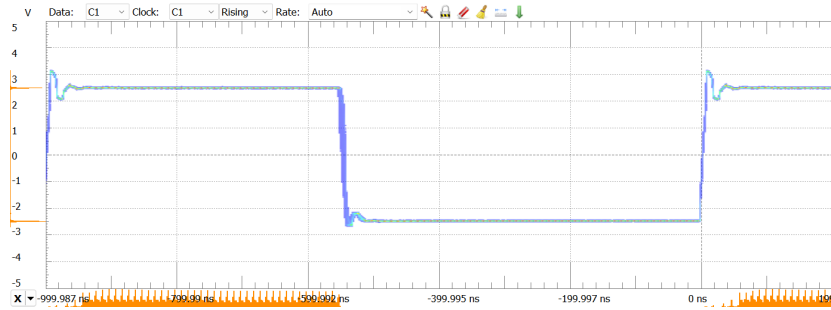


Figure 3.12: Eye diagram of the comparator signal with the emitter and receiver at a distance of 4.5m and with symbol 1 transmitted

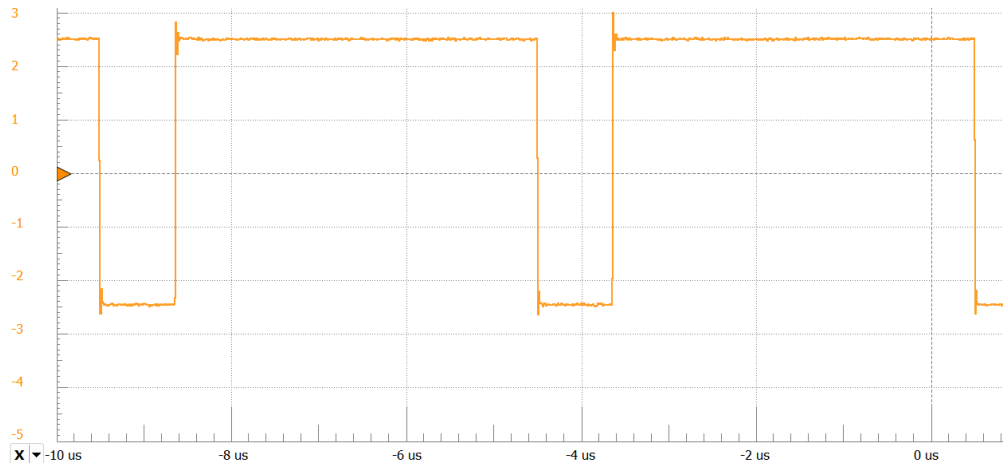


Figure 3.13: Comparator signal with the emitter and receiver at a distance of 4.5m and with symbol 8 transmitted



Figure 3.14: Eye diagram of the comparator signal with the emitter and receiver at a distance of 4.5m and with symbol 8 transmitted

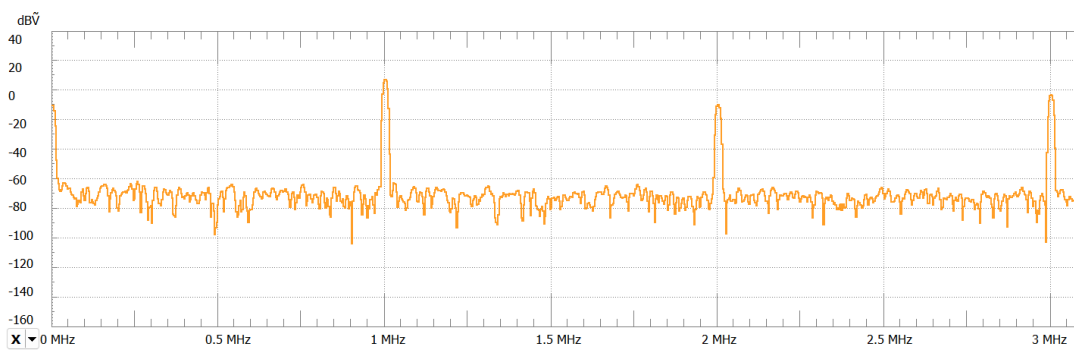


Figure 3.15: FFT of the comparator signal with the emitter and receiver at a distance of 4.5m and with symbol 1 transmitted

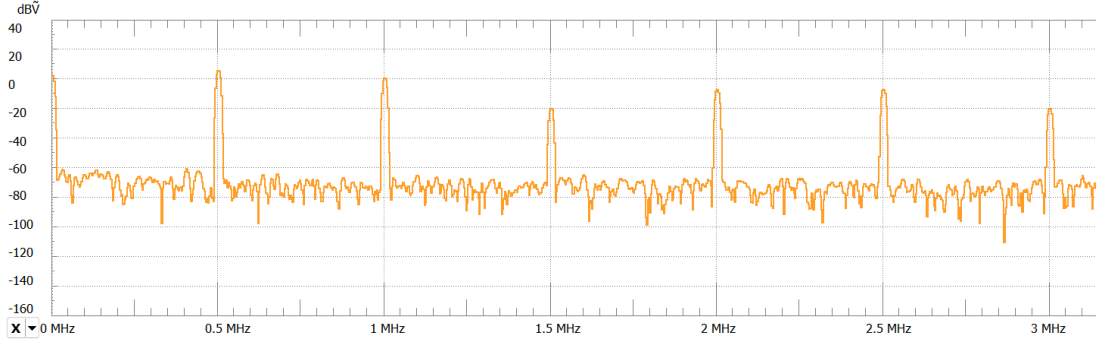


Figure 3.16: FFT of the comparator signal with the emitter and receiver at a distance of 4.5m and with symbol 3 transmitted

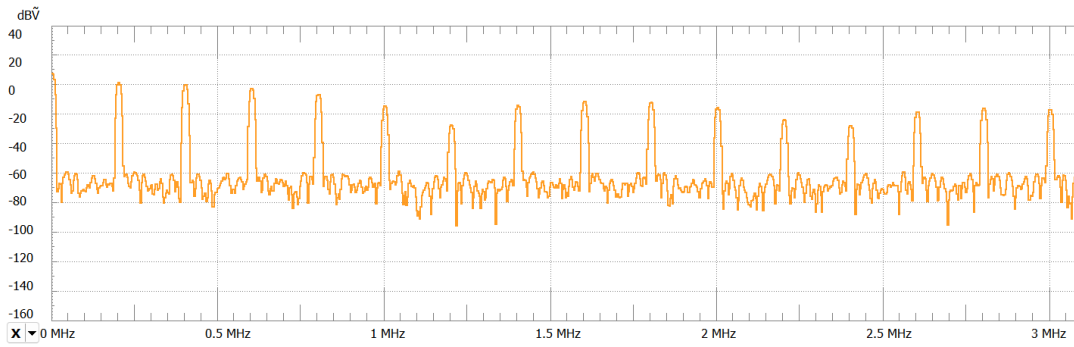


Figure 3.17: FFT of the comparator signal with the emitter and receiver at a distance of 4.5m and with symbol 8 transmitted

Evaluation with an emitter-receiver distance of 14.5m

Following the tests at 4.5m, the test are conducted with a distance of 14.5m to evaluate how the UWOCs performs at an intermediate range. The same tests as before are relaised with a signal corresponding to the first symbol of the 8-DPIM modulation. The results are shown in figure 3.18, figure 3.19 and in figure 3.20.

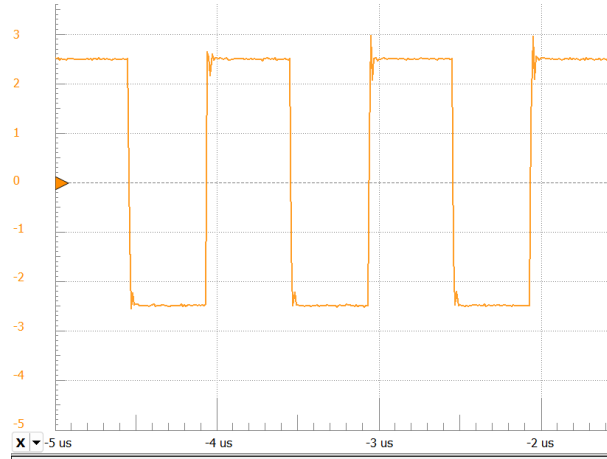


Figure 3.18: Comparator signal with the emitter and receiver at a distance of 14.5m and with symbol 1 transmitted

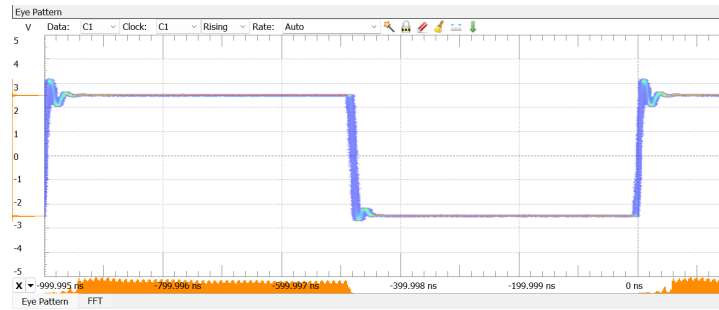


Figure 3.19: Eye diagram of the comparator signal with the emitter and receiver at a distance of 14.5m and with symbol 1 transmitted

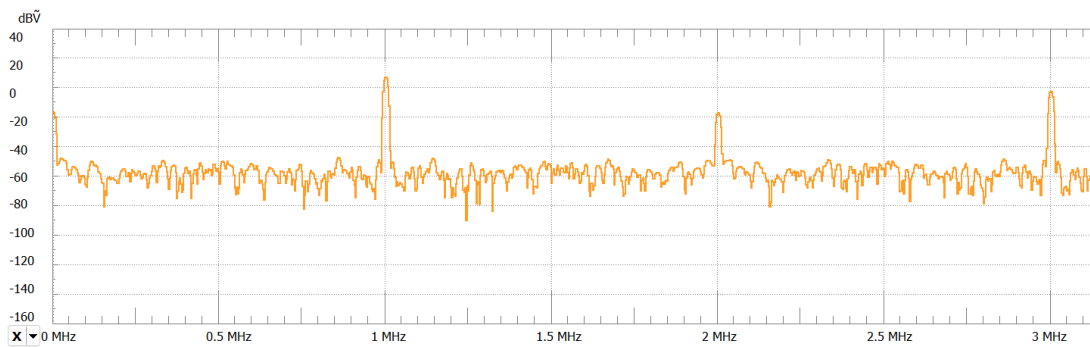


Figure 3.20: FFT of the comparator signal with the emitter and receiver at a distance of 14.5m and with symbol 1 transmitted

Evaluation with an emitter-receiver virtual distance of 50m

Finally the last tests are conducted in order to evaluate the UWOCS at its maximum range. This is executed by using the alternative configuration explained previously, in order to

simulate the longest distance and using the amplification stage in order to see how the raw signal is shaped before entering in the comparator stage. The different results are shown in figure 3.21, figure 3.22 and in figure 3.23.

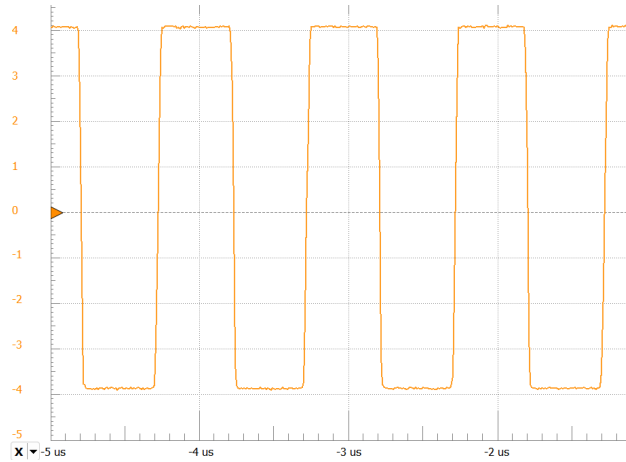


Figure 3.21: Amplification stage signal with the emitter and receiver at a distance of 50m and with symbol 1 transmitted

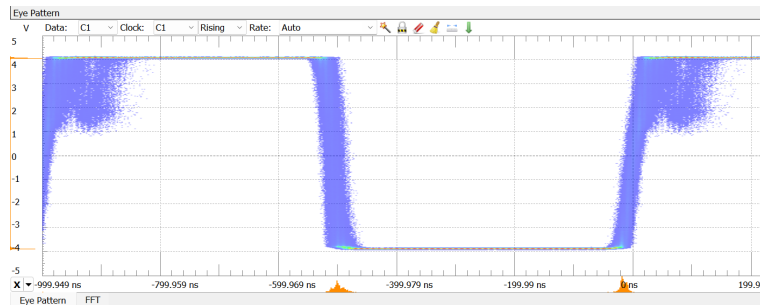


Figure 3.22: Eye diagram of the amplification stage signal with the emitter and receiver at a distance of 50m and with symbol 1 transmitted

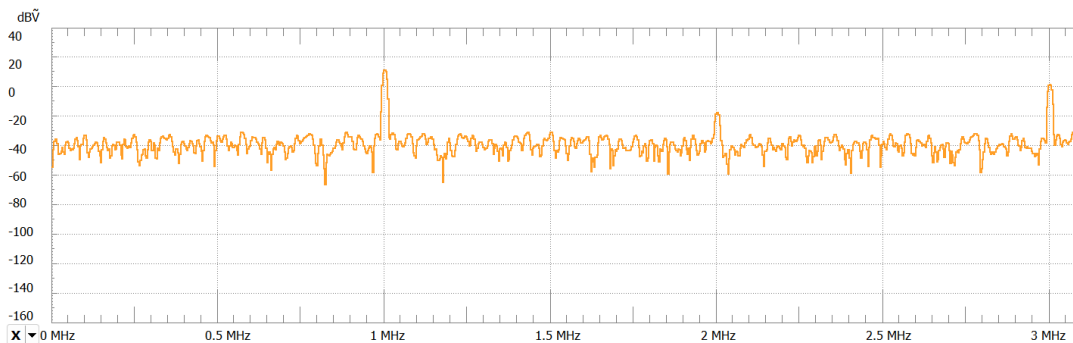


Figure 3.23: FFT of the amplification stage signal with the emitter and receiver at a distance of 14.5m and with symbol 1 transmitted

3.2 Discussion

The implemented UWOCs and the results obtained during its testing are now discussed in regard to the initial objectives enumerated in the introduction of this Master Thesis.

The primary objective was to develop a short-range, untethered transmission system capable of operating up to 50 meters between the ROV or AUV and the receiver. Based on the results obtained during testing, this objective appears at first to have been largely achieved. At the shortest test distance of 4.5 meters, the received signal was exceptionally clear on the oscilloscope, with the eye diagram indicating no significant overlap that could potentially close the eye. The pulses were well-aligned, consistent with expectations from circuit simulations [36]. This was true across all tested symbols. Although a minor peak was observed at the rising edge, it did not adversely affect the signal quality.

As the transmission distance increased, the oscilloscope continued to display a consistent signal, though the eye diagram began to show minor perturbations. However, given the width of the superimposed rising edges relative to the pulse length, these perturbations were not significant enough to impact the signal integrity.

At the maximum tested distance, the oscilloscope still displayed a signal similar to those observed at shorter ranges. However, the eye diagram exhibited more pronounced perturbations, with the rising edge width becoming more noticeable in relation to the pulse length. Despite this, the majority of the rising edges occurred within consistent intervals, as indicated by the orange distribution in the lower section of the eye diagram. This suggests a potential increase in Bit Error Rate (BER), though the overall system performance remained within acceptable parameters [36].

These results suggest that the implemented system operates effectively within the intended range. However, the results from the tests aimed at validating the maximum range should be interpreted cautiously. For the longer-range tests, the output signal was measured directly at the amplification stage. According to simulated results and the calculated gain of the amplification stage and the calculated SiPM current, the output signal should be below the saturation voltage of the final operational amplifier. This implies that the received power was likely underestimated, and while the tests represent a greater range than previous ones, they should not be taken as conclusive evidence of a 50-meter range between the emitter and receiver.

In conclusion, the implemented UWOCs has demonstrated its ability to operate effectively over various distances, likely approaching the 50-meter objective. Further testing, informed by the results of the final test, would be required to definitively confirm this range.

The second objective was to achieve a data rate within the Mbps range, suitable for transmitting multimedia content. Theoretically, this objective was met by implementing the 8-DPIM modulation scheme, which offers a bitrate of 1.09 Mbps. This achievement is corroborated by the results of the various tests, all of which demonstrated clear signal transmission across different symbols. The different FFT presented in the results section, further

supports this positive outcome by showing how the different symbols and their corresponding fundamental frequencies distinguish between themselves[36].

The final objective was to develop an UWOCS with a total Bill of Materials (BOM) under €1,000. This objective was also successfully met, as shown in the cost breakdown provided in table 3.1, which details the various cost components of the implemented UWOCS. However, one area of concern is the optical filter, which alone accounts for approximately 40% of the total system cost. This is an aspect that could be optimized in future iterations.

In conclusion, the implemented UWOCS has globally fulfilled the initial objectives set forth in the introduction of this Master’s thesis. As discussed, it would be beneficial to conduct additional testing to validate the maximum range of the UWOCS, as the tests performed may represent a shorter effective emitter-receiver distance than calculated.

Section	Price [€]
Receiver Board parts	109,56
50nm optical filter. Taken from Edmund Optics [123].	267,8
Receiver board supply parts	38,37
Emitter board parts	41,34
Emitter board supply parts	67,21
PCB’s manufacturing. Taken from PCBWay [92].	80,96
Shipping costs. Taken from PCBWay [92].	41,28
Total	646,52

Table 3.1: Total cost of the implemented UWOCS system.

CHAPTER 4

CONCLUSION AND PERSPECTIVES

The aim of this Master's thesis was to find a way of creating an innovative, high-speed underwater communication system that would be easy to develop, more accessible and less impeded by the restrictions caused by tethered systems.

In fact, a short assessment of the market shows that no existing solution provides both a highly reliable transmission system for critical operations and a data rate sufficient for multimedia content transmission at an affordable cost. Therefore, developing such a system offers new perspectives for underwater exploration.

As low-speed reliable transmitting system are already well implemented, the Master's thesis focused on studying the feasibility of implementing the high-speed part of this complete communication system. To implement such a system, various steps were necessary and the first was to select the appropriate communication channel. If firstly acoustic system was investigated finally the optical system has been selected.

First, through a review of the underwater environment and the existing Underwater Optical Communication Systems (UWOCS) presenting critical considerations to take into account when designing the system for this Master's thesis. On this basis, such a design was elaborated, and components selected for the optical emitter and receiver. Then the receiver and emitter board were designed and realized.

Thus realized, the UWOCS was tested and the results of these experiments were discussed in regards to the objectives of this Master's thesis.

Firstly, the objective to develop a short-range, untethered transmission system between the ROV or AUV operating up to 50 meters to the receiver can be considered as mainly achieved. However, further testing should be performed to definitely validate the maximum operational range.

The second objective sought to obtain a data rate within the Mbps range that could

transmit multimedia content. By relying on the 8-DPIM modulation scheme, this aim was reached, theoretically but also, first, throughout the various tests which demonstrated clear signal transmission across different symbols, and then the FFT which proved the demarcation between the different symbols and their corresponding fundamental frequencies.

The third objective of this Master's thesis was limit the Bill of Materials cost for the development of an UWOCs under €1,000. The cost breakdown assert that this last objective was also successfully met. Nevertheless, the significant cost of the optical filter could be further optimized in the future.

The research realized throughout this Master's thesis presented some limitations as previously highlighted. Nevertheless, its objectives can be considered as met. These results can provide opportunities for further developments.

The first factor to investigate would concern the lower depth limitation due to the background sunlight noise. This could certainly be improved by using some dynamic polarizers at the receiver side. Those would limit the incoming light when the background noise gets too high. A second avenue to explore would be the choice of modulation. If the 8-DPIM was chosen for its robustness and ease of implementation, it is not the most optimal modulation scheme for optical communication systems. Such complex modulation scheme as the Orthogonal Frequency Division Multiplexing (OFDM) would certainly increase the reliability of the system while increasing the bitrate [36]. Finally, adding light sources with different wavelength would certainly extend the operability of the UWOCs to some other water types such coastal waters.

As first expressed in our introduction, the oceans still hold many mysteries that humanity awaits to discover. The type of advances proposed by this Master's thesis, and the subsequent development of such projects, will hopefully make it possible to facilitate communication in underwater exploration and, by the same token, our knowledge of the deep and its secrets.

BIBLIOGRAPHY

- [1] *How much of the ocean has been explored? : Ocean Exploration Facts: NOAA Office of Ocean Exploration and Research*. URL: <https://oceanexplorer.noaa.gov/facts/explored.html> (visited on 07/08/2024).
- [2] Mehdi Rahmati and Dario Pompili. ‘SSFB: Signal-Space-Frequency Beamforming for Underwater Acoustic Video Transmission’. In: *2017 IEEE 14th International Conference on Mobile Ad Hoc and Sensor Systems (MASS)*. 2017 IEEE 14th International Conference on Mobile Ad-Hoc and Sensor Systems (MASS). Orlando, FL: IEEE, Oct. 2017, pp. 180–188. ISBN: 978-1-5386-2324-4. DOI: [10.1109/MASS.2017.71](https://doi.org/10.1109/MASS.2017.71). URL: <http://ieeexplore.ieee.org/document/8108742/> (visited on 12/08/2022).
- [3] M. Stojanovic. ‘Recent advances in high-speed underwater acoustic communications’. In: *IEEE Journal of Oceanic Engineering* 21.2 (Apr. 1996), pp. 125–136. ISSN: 03649059. DOI: [10.1109/48.486787](https://doi.org/10.1109/48.486787). URL: <http://ieeexplore.ieee.org/document/486787/> (visited on 02/08/2022).
- [4] JORDI Ribas Oliva. *Underwater wireless VIDEO TRANSMISSION USING ACOUSTIC OFDM*. OCLC: 1201667811. S.l.: LAP LAMBERT ACADEMIC PUBL, 2011. ISBN: 978-3-8433-8897-9.
- [5] J Ribas, D Sura and M Stojanovic. ‘Underwater wireless video transmission for supervisory control and inspection using acoustic OFDM’. In: *OCEANS 2010 MTS/IEEE SEATTLE*. 2010 OCEANS MTS/IEEE SEATTLE. Seattle, WA: IEEE, Sept. 2010, pp. 1–9. ISBN: 978-1-4244-4332-1. DOI: [10.1109/OCEANS.2010.5663839](https://doi.org/10.1109/OCEANS.2010.5663839). URL: <http://ieeexplore.ieee.org/document/5663839/> (visited on 22/07/2022).
- [6] *What is the difference between an AUV and a ROV?* URL: <https://oceanservice.noaa.gov/facts/auv-rov.html> (visited on 07/08/2024).
- [7] Josh Elvander and Graham Hawkes. ‘ROVs and AUVs in support of marine renewable technologies’. In: *2012 Oceans*. 2012 Oceans. ISSN: 0197-7385. Oct. 2012, pp. 1–6. DOI: [10.1109/OCEANS.2012.6405139](https://doi.org/10.1109/OCEANS.2012.6405139). URL: <https://ieeexplore.ieee.org/document/6405139/?arnumber=6405139> (visited on 07/08/2024).

- [8] G. Stenovec. ‘Systems overview of unmanned, untethered submersibles’. In: *Proceedings of the 1985 4th International Symposium on Unmanned Untethered Submersible Technology*. Proceedings of the 1985 4th International Symposium on Unmanned Untethered Submersible Technology. Vol. 4. June 1985, pp. 10–22. DOI: [10.1109/UUST.1985.1158547](https://ieeexplore.ieee.org/document/1158547?arnumber=1158547). URL: <https://ieeexplore.ieee.org/document/1158547?arnumber=1158547> (visited on 07/08/2024).
- [9] Yunxiu Zhang et al. ‘Development and Experiments of a Novel Deep-sea Resident ROV’. In: *2021 6th International Conference on Control and Robotics Engineering (ICCRE)*. 2021 6th International Conference on Control and Robotics Engineering (ICCRE). Apr. 2021, pp. 129–134. DOI: [10.1109/ICCRE51898.2021.9435653](https://ieeexplore.ieee.org/document/9435653?arnumber=9435653). URL: <https://ieeexplore.ieee.org/document/9435653?arnumber=9435653> (visited on 07/08/2024).
- [10] Z. H. Jiang. ‘Underwater acoustic networks-issues and solutions’. In: *Int. J. Intell. Control Syst.* 13.3 (2008), pp. 152–161.
- [11] N. Farr et al. ‘An integrated, underwater optical /acoustic communications system’. In: *OCEANS’10 IEEE SYDNEY*. OCEANS 2010 IEEE - Sydney. Sydney, Australia: IEEE, May 2010, pp. 1–6. ISBN: 978-1-4244-5221-7. DOI: [10.1109/OCEANSSYD.2010.5603510](https://ieeexplore.ieee.org/document/5603510). URL: <http://ieeexplore.ieee.org/document/5603510/> (visited on 15/08/2022).
- [12] John L. Butler. *Transducers and arrays for underwater sound*. New York, NY: Springer Science+Business Media, 2016. ISBN: 978-3-319-39042-0.
- [13] Hemani Kaushal and Georges Kaddoum. ‘Underwater Optical Wireless Communication’. In: *IEEE Access* 4 (2016), pp. 1518–1547. ISSN: 2169-3536. DOI: [10.1109/ACCESS.2016.2552538](https://ieeexplore.ieee.org/document/7450595). URL: [https://ieeexplore.ieee.org/document/7450595/](https://ieeexplore.ieee.org/document/7450595) (visited on 16/04/2024).
- [14] ‘Analysis and Design of Telecommunications Systems’. University Courses. University Courses. University of Liège, 2021.
- [15] M.A. Ainslie and J.G. McCollm. ‘A simplified formula for viscous and chemical absorption in sea water’. In: *Journal of the Acoustical Society of America* (1998), pp. 1671–1672.
- [16] *Absorption Overview :: Ocean Optics Web Book*. URL: <https://www.oceanopticsbook.info/view/absorption/absorption-overview> (visited on 16/04/2024).
- [17] Curtis D. Mobley. *Light and water: radiative transfer in natural waters*. San Diego: Academic Press, 1994. 592 pp. ISBN: 978-0-12-502750-2.
- [18] Yi Lou and Niaz Ahmed. *Underwater communications and networks*. Textbooks in telecommunication engineering. Cham: Springer, 2022. ISBN: 978-3-030-86649-5.
- [19] delResearch LLC. *Popoto Modem - Home*. Popoto Modem. 2021. URL: <https://www.popotomodem.com/> (visited on 16/08/2022).
- [20] *UTS-9500 Universal Topside*. URL: <https://www.teledynemarine.com/en-us/products/Pages/UTS-9500.aspx> (visited on 08/08/2024).
- [21] *Hydromea - Automating remote inspection of submerged assets - Switzerland*. Hydromea. URL: <https://www.hydromea.com> (visited on 23/09/2022).

- [22] *M2000*. Popoto Modem Store. URL: <https://popotomodem.square.site/product/m-series-modems/9> (visited on 08/08/2024).
- [23] Ikenna Chinazaekpere Ijeh. ‘Etude des effets aléatoires du canal de transmission pour les liaisons de communication optiques sous-marines sans-fil’. Thèse. Marseille: INSTITUT FRESNEL, 2021. 153 pp.
- [24] M. S. Martins et al. ‘High frequency wide beam PVDF ultrasonic projector for underwater communications’. In: *OCEANS 2017 - Aberdeen*. OCEANS 2017 - Aberdeen. Aberdeen, United Kingdom: IEEE, June 2017, pp. 1–5. ISBN: 978-1-5090-5278-3. DOI: [10.1109/OCEANSE.2017.8084677](https://doi.org/10.1109/OCEANSE.2017.8084677). URL: <http://ieeexplore.ieee.org/document/8084677/> (visited on 07/11/2022).
- [25] M. Martins et al. ‘Optimization of piezoelectric ultrasound emitter transducers for underwater communications’. In: *Sensors and Actuators A: Physical* 184 (Sept. 2012), pp. 141–148. ISSN: 09244247. DOI: [10.1016/j.sna.2012.06.008](https://doi.org/10.1016/j.sna.2012.06.008). URL: <https://linkinghub.elsevier.com/retrieve/pii/S0924424712003792> (visited on 07/11/2022).
- [26] William C. Cox. ‘A 1 Mbps Underwater Communication System Using a 405 nm Laser Diode and Photomultiplier Tube’. PhD thesis. North Carolina State University, 2007. 110 pp.
- [27] Laura Jane Johnson. ‘The Underwater Optical Channel’. In: (2015). Publisher: [object Object]. DOI: [10.13140/RG.2.1.1295.7283](https://doi.org/10.13140/RG.2.1.1295.7283). URL: <http://rgdoi.net/10.13140/RG.2.1.1295.7283> (visited on 20/04/2024).
- [28] Chadi Gabriel et al. ‘Channel modeling for underwater optical communication’. In: *2011 IEEE GLOBECOM Workshops (GC Wkshps)*. 2011 IEEE Globecom Workshops. Houston, TX, USA: IEEE, Dec. 2011, pp. 833–837. ISBN: 978-1-4673-0040-7 978-1-4673-0039-1 978-1-4673-0038-4. DOI: [10.1109/GLOCOMW.2011.6162571](https://doi.org/10.1109/GLOCOMW.2011.6162571). URL: <http://ieeexplore.ieee.org/document/6162571/> (visited on 20/05/2024).
- [29] Brandon M. Cochenour, Linda J. Mullen and Alan E. Laux. ‘Characterization of the Beam-Spread Function for Underwater Wireless Optical Communications Links’. In: *IEEE Journal of Oceanic Engineering* 33.4 (Oct. 2008), pp. 513–521. ISSN: 0364-9059, 1558-1691, 2373-7786. DOI: [10.1109/JOE.2008.2005341](https://doi.org/10.1109/JOE.2008.2005341). URL: <https://ieeexplore.ieee.org/document/4769674/> (visited on 01/06/2024).
- [30] Theodore J. Petzold. *Volume Scattering Functions for Selected Ocean Waters*: Fort Belvoir, VA: Defense Technical Information Center, 1st Oct. 1972. DOI: [10.21236/AD0753474](https://doi.org/10.21236/AD0753474). URL: <http://www.dtic.mil/docs/citations/AD0753474> (visited on 14/06/2024).
- [31] Frank Hanson and Stojan Radic. ‘High bandwidth underwater optical communication’. In: *Applied Optics* 47.2 (10th Jan. 2008), p. 277. ISSN: 0003-6935, 1539-4522. DOI: [10.1364/AO.47.000277](https://doi.org/10.1364/AO.47.000277). URL: <https://opg.optica.org/abstract.cfm?URI=ao-47-2-277> (visited on 16/04/2024).

- [32] Sermasak Jaruwatanadilok. ‘Underwater Wireless Optical Communication Channel Modeling and Performance Evaluation using Vector Radiative Transfer Theory’. In: *IEEE Journal on Selected Areas in Communications* 26.9 (Dec. 2008), pp. 1620–1627. ISSN: 0733-8716. DOI: [10.1109/JSAC.2008.081202](https://doi.org/10.1109/JSAC.2008.081202). URL: <http://ieeexplore.ieee.org/document/4686801/> (visited on 14/06/2024).
- [33] Jim Zyren. *Overview of the 3GPP Long Term Evolution Physical Layer*. July 2007. URL: <https://www.nxp.com/docs/en/white-paper/3GPPEVOLUTIONWP.pdf>.
- [34] *Data buffer*. In: *Wikipedia*. Page Version ID: 1225051048. 22nd May 2024. URL: https://en.wikipedia.org/w/index.php?title=Data_buffer&oldid=1225051048 (visited on 17/06/2024).
- [35] Marc Van Droogenbroeck. *Principes des télécommunications analogiques et numériques*. Liège, 2008. (Visited on 05/02/2024).
- [36] Bernard Sklar and Fred Harris. *Digital communications: fundamentals and applications*. Third edition. Boston, MA: Pearson, 2021. 1105 pp. ISBN: 978-0-13-458856-8.
- [37] *Modulation du signal*. In: *Wikipédia*. Page Version ID: 215110340. 15th May 2024. URL: https://fr.wikipedia.org/w/index.php?title=Modulation_du_signal&oldid=215110340 (visited on 18/06/2024).
- [38] Z. Ghassemlooy, W. Popoola and S. Rajbhandari. *Optical Wireless Communications: System and Channel Modelling with MATLAB®*. 2nd ed. Second edition. | Boca Raton, FL : CRC Press/Taylor & Francis Group, 2018.: CRC Press, 30th Apr. 2019. ISBN: 978-1-315-15172-4. DOI: [10.1201/9781315151724](https://doi.org/10.1201/9781315151724). URL: <https://www.taylorfrancis.com/books/9781498742702> (visited on 23/04/2024).
- [39] *Baseline wandering in digital transmission / Line coding to eliminate*. URL: <https://www.rfwireless-world.com/Terminology/What-is-Baseline-Wandering-in-digital-transmission.html> (visited on 19/06/2024).
- [40] Chadi Gabriel et al. ‘Investigation of suitable modulation techniques for underwater wireless optical communication’. In: *2012 International Workshop on Optical Wireless Communications (IWOW)*. 2012 International Workshop on Optical Wireless Communications (IWOW). Pisa, Italy: IEEE, Oct. 2012, pp. 1–3. ISBN: 978-1-4673-2735-0 978-1-4673-2733-6 978-1-4673-2734-3. DOI: [10.1109/IWOW.2012.6349691](https://doi.org/10.1109/IWOW.2012.6349691). URL: <http://ieeexplore.ieee.org/document/6349691/> (visited on 20/04/2024).
- [41] Zhaoquan Zeng et al. ‘A Survey of Underwater Optical Wireless Communications’. In: *IEEE Communications Surveys & Tutorials* 19.1 (2017), pp. 204–238. ISSN: 1553-877X. DOI: [10.1109/COMST.2016.2618841](https://doi.org/10.1109/COMST.2016.2618841). URL: <http://ieeexplore.ieee.org/document/7593257/> (visited on 12/10/2022).
- [42] *Sensor*. In: *Wikipedia*. Page Version ID: 1224583336. 19th May 2024. URL: <https://en.wikipedia.org/w/index.php?title=Sensor&oldid=1224583336> (visited on 24/06/2024).

- [43] *Hamamatsu, S1223-01 Full Spectrum Si Photodiode, Through Hole TO-5 / R.S.* URL: https://befr.rs-online.com/web/p/photodiodes/4155722?cm_mmc=BE-PLA-DS3A--google--CSS_BEFR_FR_Pmax_Test---_&matchtype=&gad_source=1&gclid=EAIaIQobChMIsmGgO632hgMVTXZBAh3h0g4pEAAYASAAEgLeqfD_BwE&gclsrc=aw.ds (visited on 25/06/2024).
- [44] *Si PIN photodiode S1223 / Hamamatsu Photonics.* URL: <https://www.hamamatsu.com/jp/en/product/optical-sensors/photodiodes/si-photodiodes/S1223.html> (visited on 25/06/2024).
- [45] *Hamamatsu S5344 / 3.0mm UV-VIS (200-1000nm), Si APD.* URL: <https://www.edmundoptics.com/p/30mm-uv-vis-200-1000nm-si-apd/15174/> (visited on 25/06/2024).
- [46] *Si APD S5344 / Hamamatsu Photonics.* URL: <https://www.hamamatsu.com/jp/en/product/optical-sensors/apd/si-apd/S5344.html> (visited on 25/06/2024).
- [47] *APD module C10508-01 / Hamamatsu Photonics.* URL: <https://www.hamamatsu.com/jp/en/product/optical-sensors/apd/apd-module/C10508-01.html> (visited on 25/06/2024).
- [48] ON Semiconductor. *A Brief Introduction to Silicon Photomultiplier (SiPM) Sensors.* Jan. 2019. (Visited on 22/06/2024).
- [49] Samir Cherian. *What You Need to Know about Transimpedance Amplifiers – Part 1.* Sept. 2016. URL: <https://www.ti.com/document-viewer/lit/html/SSZTBC4> (visited on 21/07/2024).
- [50] Samir Cherian. *2-What You Need to Know about Transimpedance Amplifiers – Part 2.* Sept. 2016. URL: <https://www.ti.com/document-viewer/lit/html/SSZTAY1> (visited on 21/07/2024).
- [51] Texas Instrument. *OPA818 2.7-GHz, High-Voltage, FET-Input, Low Noise, Operational Amplifier.* Mar. 2020. URL: https://www.ti.com/lit/ds/symlink/opa818.pdf?ts=1721976086563&ref_url=https%253A%252F%252Fwww.mouser.de%252F (visited on 26/07/2024).
- [52] Semiconductor Components Industries. *AND9782/D - Biasing and Readout of ON Semiconductor SiPM Sensors.* Apr. 2019. URL: <https://www.onsemi.com/pub/Collateral/AND9782-D.PDF> (visited on 14/07/2024).
- [53] Marc Van Droogenbroeck. ‘Analysis and Design of Telecommunications Systems’. Cours. Cours. University of Liège, 2022.
- [54] J.W. Giles and I.N. Bankman. ‘Underwater Optical Communications Systems Part 2: Basic Design Considerations’. In: *MILCOM 2005 - 2005 IEEE Military Communications Conference*. MILCOM 2005 - 2005 IEEE Military Communications Conference. Atlantic City, NJ, USA: IEEE, 2005, pp. 1–6. ISBN: 978-0-7803-9393-6. DOI: [10.1109/MILCOM.2005.1605919](https://doi.org/10.1109/MILCOM.2005.1605919). URL: <http://ieeexplore.ieee.org/document/1605919/> (visited on 15/04/2024).
- [55] Bruce Carter and Ron Mancini. *Op amps for everyone.* Fifth Edition. Oxford, United Kingdom Cambridge, MA: Newnes, 2018. 458 pp. ISBN: 978-0-12-811648-7.

- [56] Semiconductor Components Industries. *AND9770-D Introduction to the Silicon Photomultiplier (SiPM)*. Aug. 2023. URL: <https://www.onsemi.com/pub/Collateral/AND9770-D.PDF> (visited on 15/07/2024).
- [57] Edel Cashman. *C-Series J_Series Linearity model*. 10th Feb. 2020. (Visited on 16/07/2024).
- [58] Onsemi. *Linearity of the Silicon Photomultiplier*. Sept. 2018. (Visited on 12/07/2024).
- [59] *Réussir la conception d'un PCB avec une BGA | Altium*. URL: <https://resources.altium.com/fr/p/how-to-successfully-design-a-bga> (visited on 16/07/2024).
- [60] *INTERNATIONAL STANDARD - IEC 60364-7-702*. May 2010. URL: <https://cdn.standards.iteh.ai/samples/15568/55937377c3c849748625f0eda59993aa/IEC-60364-7-702-2010.pdf> (visited on 13/08/2024).
- [61] Semiconductor Components Industries. *MICROJSERIES/D Silicon Photomultipliers (SiPM), High PDE and Timing Resolution Sensors in a TSV Package*. Aug. 2021. URL: <https://www.onsemi.com/pdf/datasheet/microj-series-d.pdf> (visited on 14/07/2024).
- [62] *Low Pass Filter Calculator*. Omni Calculator. 29th July 2024. URL: <https://www.omnicalculator.com/physics/low-pass-filter> (visited on 14/08/2024).
- [63] *Introduction to Polarization | Edmund Optics*. URL: <https://www.edmundoptics.eu/knowledge-center/application-notes/optics/introduction-to-polarization> (visited on 21/08/2024).
- [64] *Transimpedance Amplifiers – Mouser Belgium*. URL: <https://www.mouser.be/c/semiconductors/integrated-circuits-ics/amplifier-ics/transimpedance-amplifiers/> (visited on 15/08/2024).
- [65] Hashemi Hooman. *Transimpedance Amplifiers (TIA): Choosing the Best Amplifier for the Job*. May 2017. URL: <https://www.tij.co.jp/jp/lit/an/snoa942a/snoa942a.pdf> (visited on 26/07/2024).
- [66] *Precision labs series: Op amps | TI.com*. URL: <https://www.ti.com/video/series/precision-labs/ti-precision-labs-op-amps.html> (visited on 26/07/2024).
- [67] *Stability Analysis of Voltage-Feedback Op Amps*. Mar. 2001. URL: https://www.ti.com/lit/an/sloa020a/sloa020a.pdf?ts=1723628542508&ref_url=https%253A%252F%252Fwww.google.com%252F (visited on 18/08/2024).
- [68] *OPA818 data sheet, product information and support | TI.com*. URL: <https://bit.ly/4cAh7kq> (visited on 10/08/2024).
- [69] Ron Mancini. *Op amp stability and input capacitance*. Jan. 2004. URL: https://www.ti.com/lit/an/slyt087/slyt087.pdf?ts=1723725168870&ref_url=https%253A%252F%252Fwww.google.com%252F (visited on 15/08/2024).
- [70] Ron Mancini. *Understanding Basic Analog – Ideal Op Amps*. Oct. 2016. URL: https://www.ti.com/lit/an/slaa068b/slaa068b.pdf?ts=1721545157064&ref_url=https%253A%252F%252Fwww.google.com%252F.

- [71] Paul Horowitz. *The art of electronics*. Third edition. New York, NY: Cambridge University Press, 2015. 1192 pp. ISBN: 978-0-521-80926-9.
- [72] Sergio Franco. *Design with operational amplifiers and analog integrated circuits*. 3. ed. , internat. ed. McGraw-Hill series in electrical and computer engineering. Boston, Mass.: McGraw-Hill, 2002. 658 pp. ISBN: 978-0-07-232084-8 978-0-07-112173-6.
- [73] Texas Instrument. *OPA657 Datasheet*. Aug. 2015. URL: https://www.ti.com/lit/ds/symlink/opa657.pdf?ts=1724189165055&ref_url=https%253A%252F%252Fwww.mouser.com%252F (visited on 25/07/2024).
- [74] Chi Nguyen. *An Overview on Comparators | Video | TI.com*. 3rd Mar. 2022. URL: <https://www.ti.com/video/single.html> (visited on 15/08/2024).
- [75] Texas Instrument. *TLV360x 325 MHz High-Speed Comparators with 2.5 ns Propagation Delay*. Apr. 2023. URL: https://www.ti.com/lit/ds/symlink/tlv3601.pdf?ts=1724221509676&ref_url=https%253A%252F%252Fhu.mouser.com%252F (visited on 16/08/2024).
- [76] *Comparators product selection | TI.com*. URL: <https://www.ti.com/amplifier-circuit/comparators/products.html> (visited on 16/08/2024).
- [77] *Linear & low-dropout (LDO) regulators | TI.com*. URL: <https://www.ti.com/power-management/linear-regulators-ldo/overview.html> (visited on 16/08/2024).
- [78] Analog Devices. *ADP7182 -28V,-200mA, Low Noise Linear regulator*. 2019. URL: <https://www.mouser.be/datasheet/2/609/ADP7182-1503408.pdf> (visited on 16/08/2024).
- [79] Analog Devices. *ADM7160 - Ultralow noise 200mA Linear Regulator*. 2014. URL: <https://www.mouser.be/datasheet/2/609/ADM7160-1503323.pdf> (visited on 16/08/2024).
- [80] *TLV3601 data sheet, product information and support | TI.com*. URL: <https://bit.ly/4dW38qb> (visited on 17/08/2024).
- [81] *PSpice*. URL: https://www.cadence.com/en_US/home/tools/pcb-design-and-analysis/analog-mixed-signal-simulation/pspice.html (visited on 17/08/2024).
- [82] PBElectronique. *Comment faire une trace 50 OHM ? (impédance caractéristique) - Altium Designer*. 9th June 2022. URL: <https://www.youtube.com/watch?v=OK4mfXoqBA8> (visited on 17/08/2024).
- [83] Pro-Power. *RG58 Coaxial Cable*. RG58 Coaxial Cable. 2012. URL: <https://www.farnell.com/datasheets/2095749.pdf> (visited on 17/08/2024).
- [84] *Home*. SamacSys. URL: <https://www.samacsys.com/> (visited on 18/08/2024).
- [85] *Free Online PCB CAD Library | Ultra Librarian*. Free Online PCB CAD Library. URL: <https://www.ultralibrarian.com/> (visited on 18/08/2024).
- [86] *SMA-J-P-H-ST-TH1 Samtec | Mouser*. Mouser Electronics. URL: <https://www.mouser.be/ProductDetail/Samtec/SMA-J-P-H-ST-TH1?qs=bkXR13BLxbHdaAB2Qwy6zw%3D%3D> (visited on 18/08/2024).

- [87] 5019 - TEST POINT, PCB, SMT. URL: <https://be.farnell.com/fr-BE/keystone/5019/test-point-pcb-smt/dp/2529475> (visited on 18/08/2024).
- [88] BLM21AG102SN1 datasheet. URL: https://www.mouser.be/datasheet/2/281/1/mure_s_a0010577385_1-2279215.pdf (visited on 18/08/2024).
- [89] Texas instruments. OPA818DRGEVM Evaluation Module. URL: <https://www.ti.com/lit/ug/sbou222a/sbou222a.pdf?ts=1722231017520> (visited on 18/08/2024).
- [90] Semiconductor Components Industries. AND9808-D Reference Designs for the TSV (J-Series) SMA. Mar. 2024. URL: <https://www.onsemi.com/pub/Collateral/AND9808-D.PDF> (visited on 14/07/2024).
- [91] Thin and Thick Film / Resistor Materials / Resistor Guide. URL: <https://eepower.com/resistor-guide/resistor-materials/thin-and-thick-film/> (visited on 18/08/2024).
- [92] Contact PCBWay. URL: <https://www.pcbway.com/> (visited on 21/08/2024).
- [93] How Do Pads and Vias Impact Total Capacitor Parasitic Inductance? Altium. 8th Apr. 2020. URL: <https://resources.altium.com/p/how-do-capacitor-mounting-structures-and-footprints-impact-total-inductance> (visited on 18/08/2024).
- [94] Raghbir Singh Khandpur. Printed circuit boards: design, fabrication, assembly and testing. OCLC: ocm62032512. New York: McGraw-Hill, 2006. 691 pp. ISBN: 978-0-07-146420-8.
- [95] Hard Coated OD 4.0 50nm Bandpass Filters / Edmund Optics. URL: <https://www.edmundoptics.eu/f/hard-coated-od-4-50nm-bandpass-filters/14321/> (visited on 18/08/2024).
- [96] Surface finish - PCB Prototype the Easy Way - PCBWay. URL: https://www.pcbway.com/pcb_prototype/Comparison_of_several_PCB_surface_finish_types.html (visited on 18/08/2024).
- [97] SMT Stencil - PCB Prototype the Easy Way - PCBWay. URL: https://www.pcbway.com/pcb_prototype/SMT_stencil_and_Laser_Stencil.html (visited on 18/08/2024).
- [98] 4902P - Sn42/Bi57/Ag1 Low Temperature Solder Paste T3 - Datasheet. URL: https://www.mouser.be/datasheet/2/265/tds_4902p-1149903.pdf (visited on 18/08/2024).
- [99] DD ElectroTech. How to Solder SMD Components using Sand. 30th Apr. 2019. URL: https://www.youtube.com/watch?v=aEn3Wb_zrts (visited on 18/08/2024).
- [100] SKMW15 & DKMW15 series - Datasheet. 30th Apr. 2024. URL: https://www.meanwell-web.com/content/files/pdfs/productPdfs/MW/DKMW15/SKMW15_DKMW15-spec.pdf (visited on 18/08/2024).
- [101] ZXLD1615 - Adjustable DC-DC Boost Converter with Internal Switch in TSOT23-5. Aug. 2004. URL: <https://www.diodes.com/assets/Datasheets/ZXLD1615.pdf> (visited on 19/08/2024).

- [102] Philip McGaw. *IPC 2221 standard trace widths*. PhilipMcGaw.com. 20th Feb. 2023. URL: <https://philipmcgaw.com/ipc-2221-standard-trace-widths/> (visited on 19/08/2024).
- [103] *LT1222 - 500MHz, 3nV/Hz, AV 10 Operational Amplifier - Datasheet*. URL: <https://www.analog.com/media/en/technical-documentation/data-sheets/1222fc.pdf> (visited on 20/08/2024).
- [104] *LT1222IS8#PBF Analog Devices / Mouser*. Mouser Electronics. URL: <https://www.mouser.be/ProductDetail/Analog-Devices/LT1222IS8PBF?qs=ytf1clh7QUV8za5Pg9krdQ%3D%3D> (visited on 20/08/2024).
- [105] Robert D. Guenther. *Encyclopedia of modern optics*. Online-ausg. Amsterdam [u.a.]: Elsevier Acad. Press, 2005. ISBN: 978-0-12-369395-2.
- [106] B. Vanderheyden. *ELEN0004 - Semiconductor Devices*. Liège, 20th Dec. 2023. (Visited on 07/07/2024).
- [107] B. Vanderheyden. *ELEN0074 - Electronique Analogique*. Liège, 17th Feb. 2024. (Visited on 07/07/2024).
- [108] Marek Doniec and Daniela Rus. ‘BiDirectional optical communication with AquaOptical II’. In: *2010 IEEE International Conference on Communication Systems*. 2010 IEEE International Conference on Communication Systems (ICCS). Singapore, Singapore: IEEE, Nov. 2010, pp. 390–394. ISBN: 978-1-4244-7004-4. DOI: [10.1109/ICCS.2010.5686513](https://doi.org/10.1109/ICCS.2010.5686513). URL: <http://ieeexplore.ieee.org/document/5686513/> (visited on 15/04/2024).
- [109] Yun-Han Chang et al. ‘Passive 100W High Power Bias-Tee for Visible Light Communication Systems’. In: *2020 Opto-Electronics and Communications Conference (OECC)*. 2020 Opto-Electronics and Communications Conference (OECC). Taipei, Taiwan: IEEE, 4th Oct. 2020, pp. 1–3. ISBN: 978-1-72815-445-9. DOI: [10.1109/OECC48412.2020.9273606](https://doi.org/10.1109/OECC48412.2020.9273606). URL: <https://ieeexplore.ieee.org/document/9273606/> (visited on 11/04/2024).
- [110] Cree corporation. *XLamp XHP35.2 LEDs*. 2024. URL: https://www.mouser.be/datasheet/2/723/XLamp_XHP35_2-3317367.pdf (visited on 07/07/2024).
- [111] Thorlabs. *Radiometric vs. Photometric Units*. URL: <https://www.thorlabs.de/catalogPages/506.pdf> (visited on 08/07/2024).
- [112] Lumileds. *LUXEON Rebel Color Line*. Lumileds. 2023. URL: <https://lumileds.com/wp-content/uploads/files/DS068-luxeon-rebel-color-line-datasheet.pdf> (visited on 08/07/2024).
- [113] ams-OSRAM. *OSRAM GD CSSRM3.14-AJAM-24-1-700-R33 - Datasheet*. 3rd Jan. 2022. URL: https://mm.digikey.com/Volume0/opasdata/d220001/medias/docus/4064/GD_CSSRM3.14_Ver1.0_3-1-22.pdf (visited on 17/08/2024).

- [114] Hubert Halbritter et al. ‘High-Speed LED Driver for ns-Pulse Switching of High-Current LEDs’. In: *IEEE Photonics Technology Letters* 26.18 (Sept. 2014). Conference Name: IEEE Photonics Technology Letters, pp. 1871–1873. ISSN: 1941-0174. DOI: [10.1109/LPT.2014.2336732](https://doi.org/10.1109/LPT.2014.2336732). URL: <https://ieeexplore.ieee.org/document/6851184/?arnumber=6851184> (visited on 17/07/2024).
- [115] *MIC4421A/22A - 9A Peak Low-Side MOSFET Drivers - Datasheet*. 2021. URL: https://www.mouser.be/datasheet/2/268/MIC4421A_22A_9A_Peak_Low_Side_MOSFET_Drivers_DS200-3441927.pdf.
- [116] *LUXEON Illumination LEDs - Circuit Design and Layout Practices to Minimize Electrical Stress*. 2016. URL: <https://lumileds.com/wp-content/uploads/files/AB06.pdf> (visited on 19/08/2024).
- [117] *10170*. DigiKey Electronics. URL: <https://www.digikey.be/en/products/detail/carclo-technical-plastics/10170/2641626> (visited on 19/08/2024).
- [118] *C11347_REGINA*. DigiKey Electronics. URL: <https://www.digikey.fr/fr/products/detail/ledil/C11347-REGINA/2350496> (visited on 19/08/2024).
- [119] *Premium Aluminum PCB Manufacturer - PCBWay*. URL: <https://www.pcbway.com/aluminum-pcb.html> (visited on 20/08/2024).
- [120] *Meanwell_RSDW60 Datasheet*. 21st May 2020. URL: https://www.mouser.be/datasheet/2/260/Meanwell_RSDW60_2cRDDW60-1855652.pdf (visited on 20/08/2024).
- [121] *Sea water*. Sea water. URL: <https://www.nio.res.in/files/view/29fbd01f222086c#:~:text=Density%20of%20cean%20is%20determined,parcel%20of%20seawater%20is%20exposed.&text=Density%20is%20lighter%20at%20the,ocean%20is%201.03%20g%2Fcm3..>
- [122] *K&F Concept Ø58mm Filtre Polarisant CPL True Color HD Nano-revêtement de 28 Couches Étanche Supprime Les Reflets pour Objectif Appareil Photo : Amazon.com.be: High-tech*. URL: <https://bit.ly/4dNrPD> (visited on 21/08/2024).
- [123] *Filtre Passe-Bande OD 4 Non Monté, Traitement Dur, 50 nm, CWL 450 nm, 25 mm de Dia*. URL: <https://www.edmundoptics.fr/p/450nm-cwl-25mm-dia-hard-coated-od-40-50nm-unmounted-bandpass-filter/43217/> (visited on 21/08/2024).

APPENDIX A

DIFFERENT USEFUL TABLES

A.1 Underwater environment.

λ [nm]	$a(\lambda)$ (m^{-1})
400	0.018
410	0.017
420	0.016
430	0.015
440	0.015
450	0.015
460	0.016
470	0.016
480	0.018
490	0.020
500	0.026
510	0.036
520	0.048

Table A.1: Absorption coefficient $a(\lambda)$ for various wavelength in the visible EM spectrum.
Adapted from [17] p.98

Distance [m]	$I_r(\Phi_b = 90^\circ)$	$I_r(\Phi_b = 15^\circ)$
1	2.74E-01	1.58E+01
5	5.98E-03	3.45E-01
10	7.03E-04	4.06E-02
15	1.47E-04	8.47E-03
20	3.88E-05	2.24E-03
25	1.17E-05	6.74E-04
30	3.81E-06	2.20E-04
35	1.32E-06	7.60E-05
40	4.74E-07	2.73E-05
45	1.76E-07	1.02E-05
50	6.70E-08	3.86E-06

Table A.2: Irradiance $[\frac{W}{m^2}]$ at the receiver side as a function of the distance, d , for different beam angles.

A.2 Bill of materials

The different components where either ordered from Mouser (url : mouser.com) or Digikey (url : digikey.com). The component's prices where updated on the 21/08/2024.

PCB - UWOCs Receiver v1 - Bill of material					
LibRef	Characteristics	Description	Designator	Quantity	Total price [€]
GCM31CR71H225KA55K	2.2u-1206-50V	Capacitor	C1, C2, C3, C4, C5, C6, C7, C56, C57	9	2,59 €
KAM15AR71H104KM	100n-603-C0G-50V	Capacitor	C8, C11	2	0,19 €
06035A103JAT2A	10n-603-C0G-50V	Capacitor	C9, C12, C16, C20, C33, C37, C41, C45, C48, C50, C54	11	3,07 €
C0603X100J1GACAU0	10p-603-C0G-50V	Capacitor	C10, C13	2	0,61 €
GRM31C5C1E474JB01L	470n-1206-5p	Capacitor	C14, C31	2	1,56 €
C0603X101J5GACTU	100pF-603-C0G	Capacitor	C15, C18, C19, C32, C35, C36, C40, C43, C44, C49, C52,	12	3,01 €
06035C224JAT2A	220nF-603	Capacitor	C17, C21, C34, C38, C42, C46, C51, C55	8	3,87 €
06035A5R0JAT2A	5pF-0603-N0G	Capacitor	C22, C23, C24	3	0,98 €
UMJ316BC7475KL8TE	4.7u-1206-50V	Capacitor	C58, C59	2	1,19 €
BLM21AG102SN1D	FB-1k	Filter	FL1, FL2	2	0,30 €
MICROFJ-60035-TSV-TR	-	SiPM	IC1	1	40,50 €
OPA818IDRGR	OPA818IDRGR	Integrated Circuit	IC2, IC4, IC5	3	21,81 €
TLV3601QDBVRQ1	TLV3601QDBVRQ1	Integrated Circuit	IC6	1	4,70 €
HTSW-103-07-G-S	HTSW-103-07-G-S	Connector	J1, J3	2	0,91 €
796949-4	Power IN	Connector	J2	1	1,14 €
SMA-J-P-H-ST-TH1	SMA connectors	Connector	J4, J5	2	10,80 €
ADP7182AUJZ-2.5-R7	ADP7182AUJZ-2.5-R7	Power Supply	PS1	1	4,78 €
ADM7160AUJZ-2.5-R2	ADM7160AUJZ-2.5-R2	Power Supply	PS2	1	2,33 €
ERA-8APB5110V	500-1206	Resistor	R1, R8	2	1,69 €
ERA-3AED202V	2k - 0603	Resistor	R2, R6, R9	3	0,34 €
ERA-3AED101V	100ohm - 0603	Resistor	R3, R7, R10	3	0,34 €
TNPW12064R99DEEA	5ohm-1206	Resistor	R4	1	0,61 €
ERA-8AEB102V	1k-1206	Resistor	R5, R11	2	0,69 €
CRCW12068K06FKEAC	8k-1206	Resistor	R12	1	0,09 €
ERJ-S08F2001V	2k-1206-1p	Resistor	R13, R14, R15	3	1,03 €
ERA-3AEB49R9V	49.9-603	Resistor	R18	1	0,12 €
5019	5019- Test pad	Test Point	TP1	1	0,32 €
				Total board price	109,56 €

Figure A.1: Bill of material (BOM) of the UWOCs receiver board

PCB - UWOCs Receiver Supply board - Bill of material					
LibRef	Characteristics	Description	Designator	Quantity	Total price [€]
GCM31CR71H225KA55K	2.2uF - 1206	Capacitor	C1, C2, C3, C4, C5, C6, C7, C8	8	2,32 €
08051A4R7BAT2A	4.7pF - 0805 - N0G	Capacitor	C9	1	0,47 €
ZHCS400TC	ZHCS400TC	Diode	D1	1	0,36 €
ZXLD1615ET5TA	28V ZXLD1615ET5TA	Integrated Circuit	IC1	1	1,00 €
2383942-2	2383942-2	Connector	J1	1	2,93 €
796949-4	796949-4	Connector	J2	1	1,14 €
LQW43FT100M0HL	10uH	Inductor	L1	1	2,64 €
DKMW15F-05	DKMW15F-05	Power Supply	PS1	1	25,64 €
RG3216N-1004-W-T1	1M	Resistor	R1	1	1,16 €
ERA-6ARW393V	39k - 0805	Resistor	R2	1	0,71 €
Total board price					38,37 €

Figure A.2: Bill of material (BOM) of the UWOCs receiver supply board

PCB - UWOCs Emitter - Bill of material					
LibRef	Characteristics	Description	Designator	Quantity	Total price [€]
GCM31CR71H225KA55K	2.2u - 1206	Capacitor	C1, C2, C5, C6, C7, C8	6	1,73 €
KAM15AR71H104KM	100n-603	Capacitor	C3, C9, C10	3	0,28 €
06035A103JAT2A	10n-0603	Capacitor	C4, C11, C12	3	0,84 €
MIC4422AYM	MIC4422AYM	Integrated Circuit	IC1, IC2, IC3	3	6,45 €
SMA-J-P-GF-RA-SM1	SMA-J-P-GF-RA-SM1	Connector	J1	1	8,13 €
2383942-2	2383942-2	Connector	J2, J3	2	5,86 €
GD_CS8PM1.14-UOVJ-W4-1	LED	LED	LED1, LED2, LED3	3	4,53 €
35401R0FT	1ohm	Resistor	R1, R3, R4	3	4,65 €
CRCW1206100KFKEAHP	100k-1206	Resistor	R2, R5, R6	3	0,70 €
10170	Carclo tech. Plastic	Concentrators	/	1	1,40 €
C11347_REGINA	-	Concentrators	/	2	6,78 €
Total board price					41,34 €

Figure A.3: Bill of material (BOM) of the UWOCs emitter board

PCB - UWOCs Emitter Supply board - Bill of material					
LibRef	Characteristics	Description	Designator	Quantity	Total price [€]
C1206C222GBGACAUTO	2200pF - 1206 - C0G	Capacitor	C1	1	0,55 €
KAM55CR72A106KV	10uF - 2220- XR7	Capacitor	C2, C3	2	5,32 €
2383942-2	2383942-2	Connector	J1, J2, J3	3	8,79 €
SRP1245CC-1R5M	1.5uH - 48A - 3.5mO	Inductor	L1	1	1,55 €
RSDW60F-05	RSDW60F-05	Power Supply	PS1	1	50,71 €
CRCW25128K66FKEG	8.66k - 2512 - 1W	Resistor	R1	1	0,29 €
Total board price					67,21 €

Figure A.4: Bill of material (BOM) of the UWOCs emitter supply board

APPENDIX B

USEFUL FIGURES

B.1 Simulation

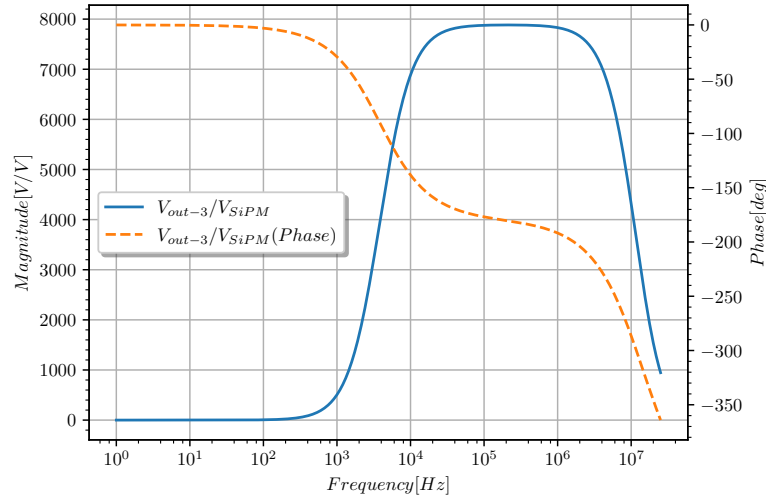


Figure B.1: AC simulation of the receiver board showing the gain between the last amplification stage output and the SiPM output voltage. This taking the highest SiPM output current

B.2 Schematics

Here are shown the complete schematics of the receiver board. The others boards schematics are already in the main text of this Master's Thesis.

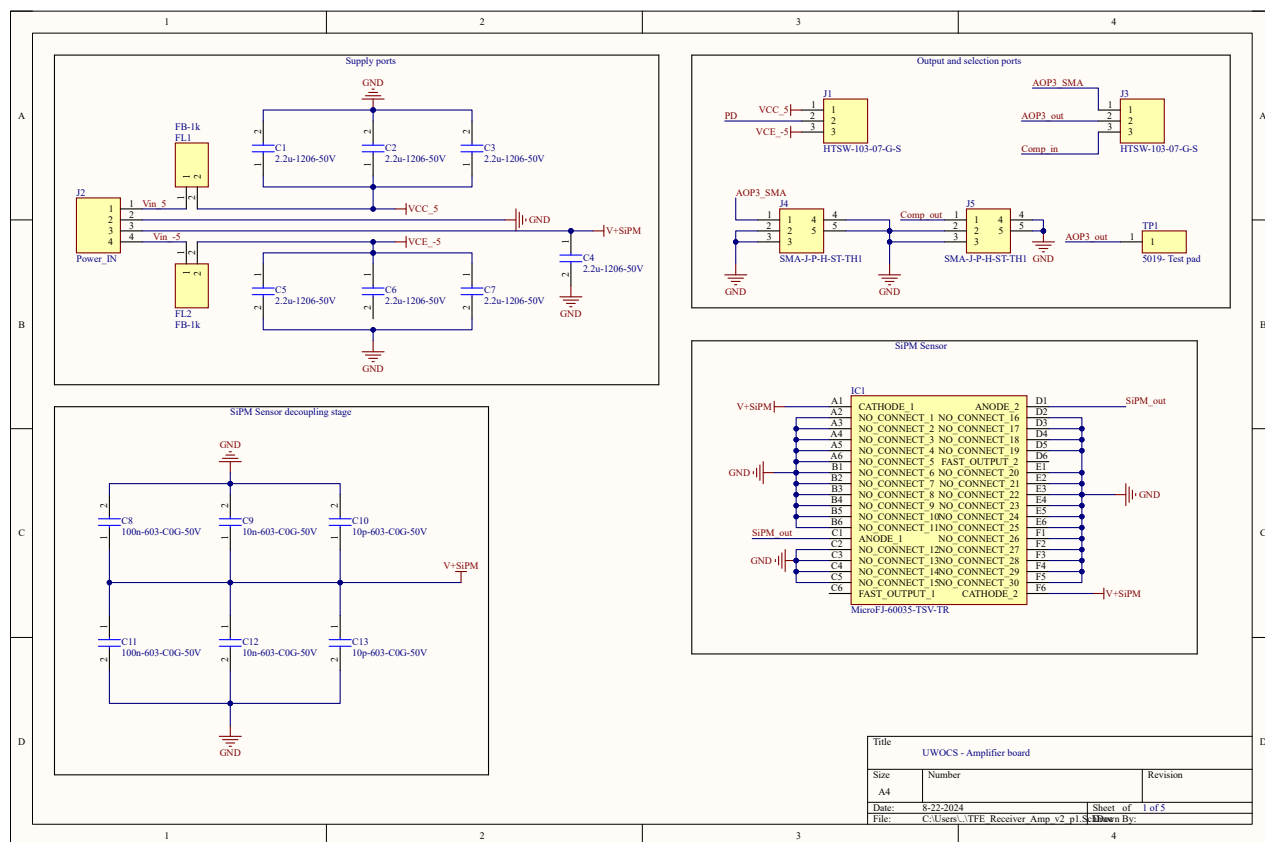


Figure B.2: Schematics of the receiver board. Page 1 of 5.

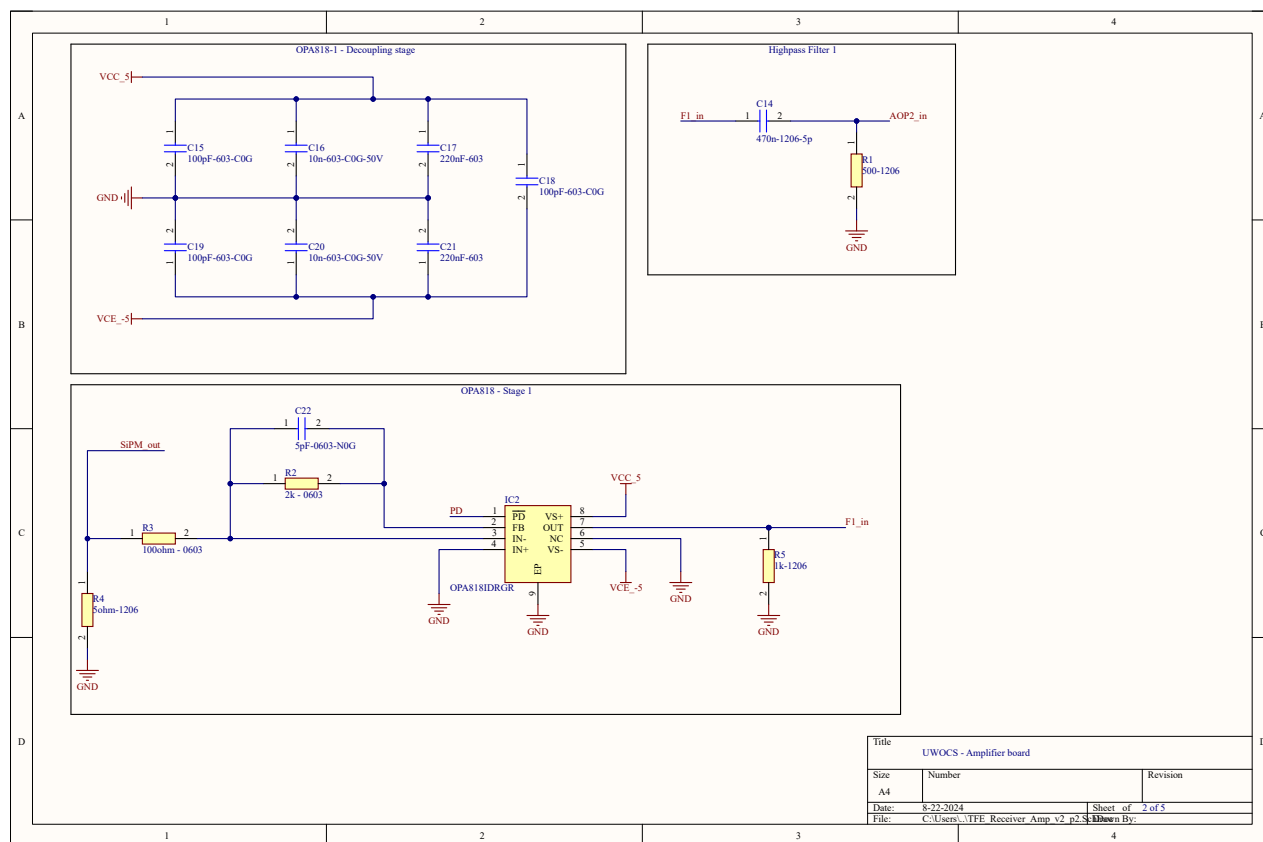


Figure B.3: Schematics of the receiver board. Page 2 of 5.

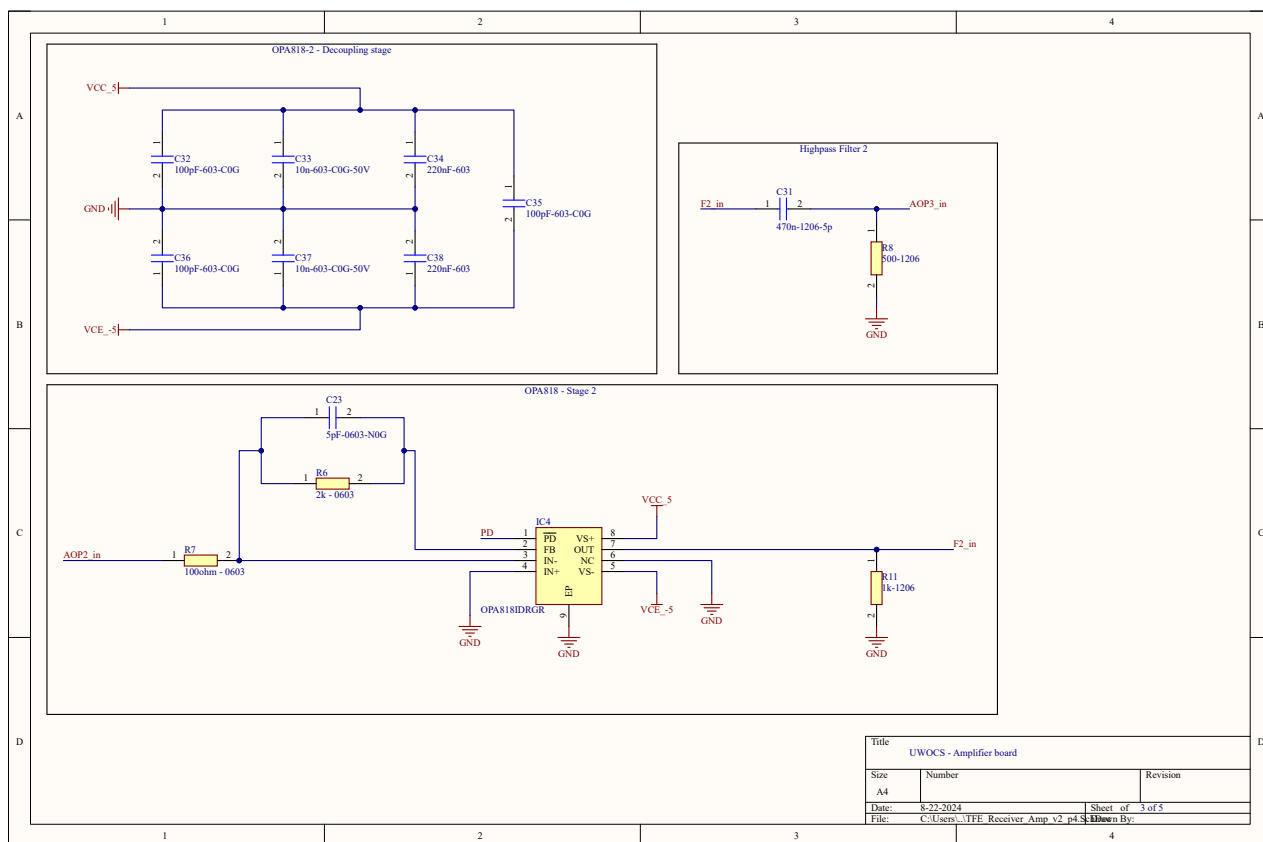


Figure B.4: Schematics of the receiver board. Page 3 of 5.

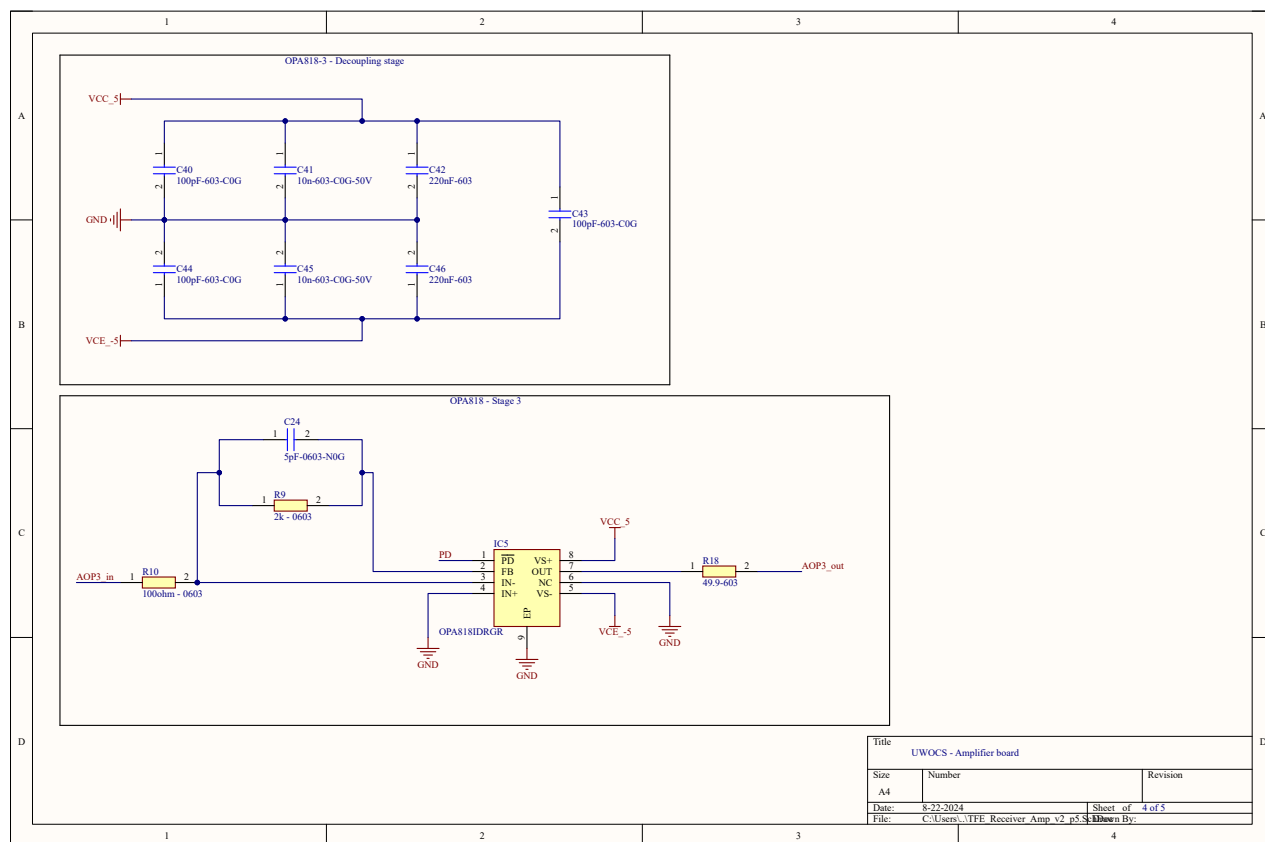


Figure B.5: Schematics of the receiver board. Page 4 of 5.

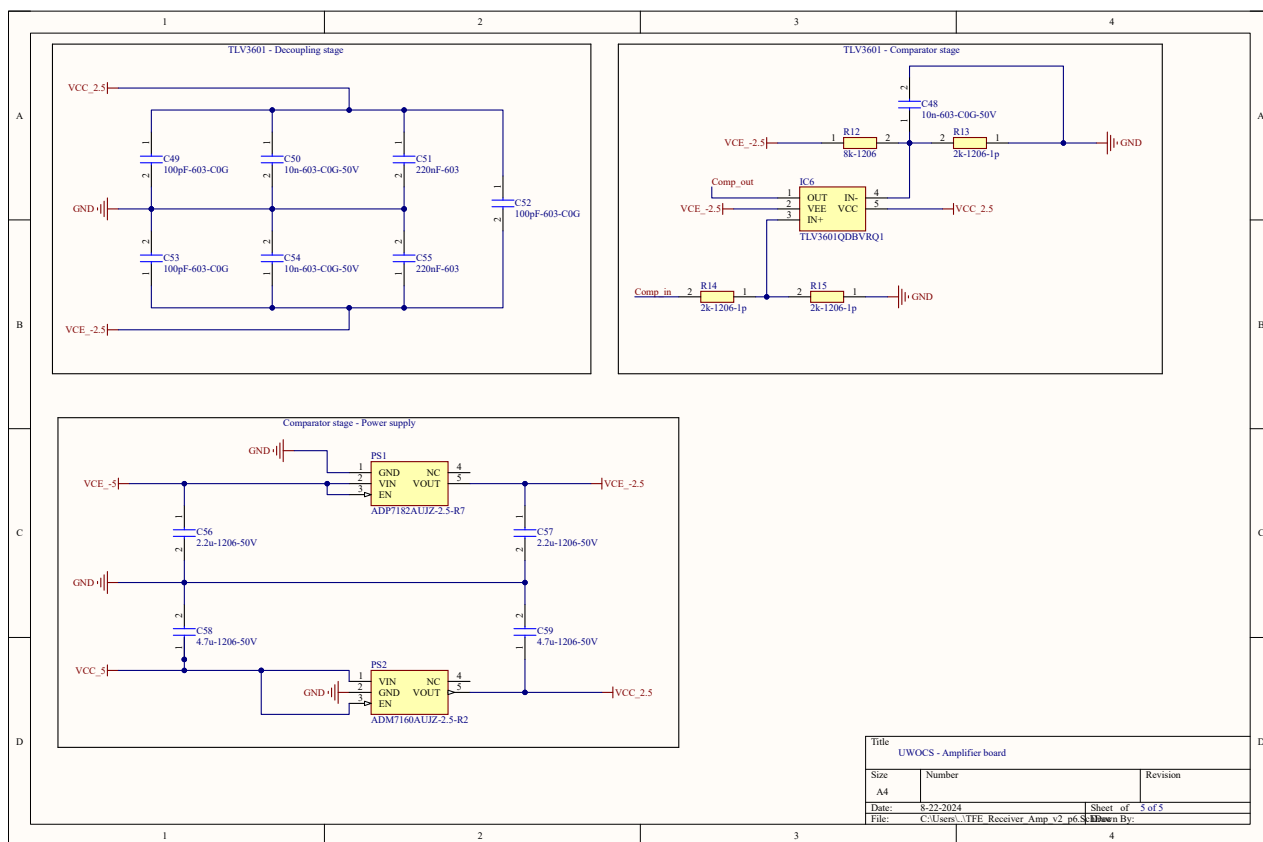


Figure B.6: Schematics of the receiver board. Page 5 of 5.